FINAL REPORT

Examination of Wildland Fire Spread at Small Scales Using Direct Numerical Simulations and Frequency Comb Laser Diagnostics

SERDP Project RC-2642

JUNE 2021

Peter E. Hamlington
John W. Daily
Gregory B. Rieker
John Farnsworth
Michael Hannigan
Hope Michelsen
Sean Coburn
Caelan Lapointe
Charlie Callahan
Jeff Glusman
Eric Kolb
Amanda Makowiecki
Prakriti Sardana
Samantha Sheppard
Sam Simons-Wellin
Nicholas Wimer
Tim Breda
Abdul Dawlatzai
Chris Kling
University of Colorado, Boulder

Alexei Y. Poludnenko
Texas A&M University, College Station

Chad M. Hoffman
Colorado State University, Fort Collins

Distribution Statement A
This document has been cleared for public release

SERDP
DOD ▪ EPA ▪ DOE

This report was prepared under contract to the Department of Defense Strategic Environmental Research and Development Program (SERDP). The publication of this report does not indicate endorsement by the Department of Defense, nor should the contents be construed as reflecting the official policy or position of the Department of Defense. Reference herein to any specific commercial product, process, or service by trade name, trademark, manufacturer, or otherwise, does not necessarily constitute or imply its endorsement, recommendation, or favoring by the Department of Defense.

REPORT DOCUMENTATION PAGE

Form Approved
OMB No. 0704-0188

The public reporting burden for this collection of information is estimated to average 1 hour per response, including the time for reviewing instructions, searching existing data sources, gathering and maintaining the data needed, and completing and reviewing the collection of information. Send comments regarding this burden estimate or any other aspect of this collection of information, including suggestions for reducing the burden, to Department of Defense, Washington Headquarters Services, Directorate for Information Operations and Reports (0704-0188), 1215 Jefferson Davis Highway, Suite 1204, Arlington, VA 22202-4302. Respondents should be aware that notwithstanding any other provision of law, no person shall be subject to any penalty for failing to comply with a collection of information if it does not display a currently valid OMB control number.
PLEASE DO NOT RETURN YOUR FORM TO THE ABOVE ADDRESS.

1. REPORT DATE *(DD-MM-YYYY)*	**2. REPORT TYPE**	**3. DATES COVERED** *(From - To)*
11/06/2021	SERDP Final Report	7/28/2016 - 7/27/2021

4. TITLE AND SUBTITLE

Examination of Wildland Fire Spread at Small Scales Using Direct Numerical Simulations and Frequency Comb Laser Diagnostics

5a. CONTRACT NUMBER
16-C-0026

5b. GRANT NUMBER

5c. PROGRAM ELEMENT NUMBER

6. AUTHOR(S)

Peter E. Hamlington, John W. Daily, Gregory B. Rieker, John Farnsworth, Michael Hannigan, Hope Michelsen, Sean Coburn, Caelan Lapointe, Charlie Callahan, Jeff Glusman, Eric Kolb, Amanda Makowiecki, Prakriti Sardana, Samantha Sheppard, Sam Simons-Wellin, Nicholas Wimer, Tim Breda, Abdul Dawlatzai, Chris Kling: **University of Colorado, Boulder**

Alexei Y. Poludnenko: **Texas A&M University, College Station**

Chad M. Hoffman: **Colorado State University, Fort Collins**

5d. PROJECT NUMBER
RC-2642

5e. TASK NUMBER

5f. WORK UNIT NUMBER

7. PERFORMING ORGANIZATION NAME(S) AND ADDRESS(ES)
University of Colorado, Boulder
427 UCB
Boulder, CO 80309-0427

8. PERFORMING ORGANIZATION REPORT NUMBER
RC-2642

9. SPONSORING/MONITORING AGENCY NAME(S) AND ADDRESS(ES)
Strategic Environmental Research and Development Program (SERDP)
4800 Mark Center Drive, Suite 16F16
Alexandria, VA 22350-3605

10. SPONSOR/MONITOR'S ACRONYM(S)
SERDP

11. SPONSOR/MONITOR'S REPORT NUMBER(S)
RC-2642

12. DISTRIBUTION/AVAILABILITY STATEMENT

DISTRIBUTION STATEMENT A. Approved for public release: distribution unlimited.

13. SUPPLEMENTARY NOTES

14. ABSTRACT

The primary objective of this project was to understand and characterize wildland fire spread at small scales (roughly 1m—1mm) using high fidelity direct and large eddy simulations (DNS and LES, respectively) with reduced chemical kinetic mechanisms calibrated using data from frequency comb laser diagnostics (FCLD). Specific objectives of this project were to (i) Understand and characterize wildland fire spread at scales from roughly 1m to below 1mm using DNS and LES to directly resolve relevant fluid and chemical processes. (ii) Develop and calibrate reduced chemical kinetics mechanisms for the pyrolysis, ignition, and combustion of wildland fuels. (iii) Use frequency comb laser diagnostics to study wildland fire spread at small scales by providing data for the calibration of reduced chemical mechanisms and for simulation validation. (iv) Use insights from the computations and experiments to perform improved simulations of wildland fire spread at landscape scales.

15. SUBJECT TERMS

Wildland Fire Spread, Direct Numerical Simulations, Frequency Comb Laser Diagnostics

16. SECURITY CLASSIFICATION OF:			**17. LIMITATION OF ABSTRACT**	**18. NUMBER OF PAGES**	**19a. NAME OF RESPONSIBLE PERSON**
a. REPORT	**b. ABSTRACT**	**c. THIS PAGE**			Peter Hamlington
UNCLASS	UNCLASS	UNCLASS	UNCLASS	96	**19b. TELEPHONE NUMBER** *(Include area code)* 303-492-0555

Abstract

Introduction and Objectives: The primary objective of this project was to understand and characterize wildland fire spread at small scales (roughly 1m—1mm) using high fidelity direct and large eddy simulations (DNS and LES, respectively) with reduced chemical kinetic mechanisms calibrated using data from frequency comb laser diagnostics (FCLD). Specific objectives of this project were to (i) Understand and characterize wildland fire spread at scales from roughly 1m to below 1mm using DNS and LES to directly resolve relevant fluid and chemical processes. (ii) Develop and calibrate reduced chemical kinetics mechanisms for the pyrolysis, ignition, and combustion of wildland fuels. (iii) Use frequency comb laser diagnostics to study wildland fire spread at small scales by providing data for the calibration of reduced chemical mechanisms and for simulation validation. (iv) Use insights from the computations and experiments to perform improved simulations of wildland fire spread at landscape scales.

Technical Approach: This project consisted of a joint computational and experimental effort focused on two configurations. In the first, pyrolysis, ignition, and burning of solid wood samples were measured and simulated in a mass-loss calorimeter. Different wood types, moisture contents, and radiative fluxes were examined. The resulting experimental data were used to develop and calibrate reduced chemical kinetic models for pyrolysis and gas phase combustion, as well as for validation of the computational simulations. In the second configuration, fire spread was examined in a novel tilting wind tunnel, called the WindCline, for different fuel types, crossflow wind speeds, and slope angles. Experimental measurements of temperature, water mole fraction, flame height, and spread rate for different conditions were used to validate the simulations.

Results: This project was the first to demonstrate the use of adaptive mesh refinement (AMR) for physically accurate and computationally efficient simulations of buoyancy driven flows, pool fires, laboratory-scale biomass combustion, and wildland fire spread. Complex reaction mechanisms for pyrolysis and gas phase combustion were successfully reduced using automated mechanism reduction software, resulting in chemical models that were sufficiently compact for implementation in the AMR simulations. This project was also the first to use FCLD to study evaporation, pyrolysis, ignition, and combustion of solid wildland fuels. Both near-infrared and mid-infrared FCLD were used to calculate time series of temperature and species concentrations during biomass evaporation, pyrolysis, ignition, and combustion for different fuel types and fuel moisture contents. Finally, simulations of fire spread at larger scales were performed using simulations with AMR in both solid and gas phases. Again, this was the first demonstration of AMR for simulations of large-scale fire spread, showing that grid adaptation can be used to significantly reduce computational cost while maintaining physical accuracy.

Benefits: The combined computational and experimental approach of this project provided unprecedented access to information about chemical species, temperature, and turbulence during the entire pyrolysis, evaporation, ignition, and combustion process, thereby permitting more complete understanding of the physics that must be represented by coarse-scale numerical models of wildland fire spread. The proposed project was also specifically focused on the small-scale behavior of wildland fires and has provided a simulation capability that fills a gap in the current hierarchy of wildland fire computational models. An important outcome of this project was the development of an AMR-based computational capability, which will be of direct benefit for the planning and prediction of prescribed burns. Ultimately, the proposed research has brough together two cutting-edge technologies (AMR and FCLD) for the first time in wildland fire research.

Table of Contents

1. Executive Summary 4

1.1. Introduction 4

1.2. Objectives 4

1.3. Technical Approach 4

1.4. Results and Discussion 5

1.5. Implications for Future Research and Benefits 13

2. Introduction and Objectives 14

3. Background 15

3.1 Computational Approaches in Combustion and Wildland Fire Modeling 15

3.2 Chemical Kinetics Mechanisms for Wildland Fire Spread 17

3.3 Advanced Combustion Diagnostics Based on Frequency Comb Lasers 19

4. Results Overview 20

5. Results: Numerical Simulations of Wildland Fire Spread at Small Scales 20

5.1 Direct Numerical Simulations of Fire Dynamics at Small Scales 20

5.2 Adaptive Mesh Simulations of Buoyancy Driven Flows (Wimer et al. 2020, 2021) 24

5.3 Adaptive Mesh Simulations of Turbulent Diffusion Flames (Lapointe et al. 2020) 29

5.4 Adaptive Mesh Simulations of Propagating Flames 34

6. Results: Chemical Kinetic Model Reduction and Implementation 43

6.1 Chemical kinetic model reduction (Glusman et al. 2019) 44

6.2 Chemical Kinetic Model Implementation 48

7. Results: Measurements of Biomass Combustion Using FCLD 53

7.1 Near Infrared DCS of Solid Fuel Pyrolysis and Combustion (Makowiecki et al., 2020) 54

7.2 Mid Infrared DCS of Solid Fuel Pyrolysis (Makowiecki et al., 2021) 59

7.3 WindCline Measurements 63

8. Results: Numerical Simulations of Landscape Scale Fires 69

8.1 AMR Based Computational Solver for Landscape-Scale Simulations 69

8.2 AMR Based Landscape-Scale Simulations 72

9. Conclusions and Implications for Future Research/Implementation 73

10. References 75

11. Appendices 84

11.1 Appendix A: Supporting Data 84

11.2 Appendix B: List of Scientific/Technical Publications 84

List of acronyms

AMI: Arbitrary mesh interface
AMR: Adaptive mesh refinement
CFL: Courant, Friedrichs, Levy
CRECK: Chemical Reaction Engineering and Chemical Kinetics
CTU: Corner transport upwind
DCS: Dual comb spectroscopy
DFG: Difference-frequency generation
DNS: Direct numerical simulation
DRGEP: Directed relation graph with error propagation
DRGEPSA: Directed relation graph with error propagation and sensitivity analysis
DSLR: Digital single-lens reflex
EDM: Eddy dissipation model
FCLD: Frequency comb laser diagnostics
FDS: Fire dynamics simulator
FTIR: Fourier transform infrared spectroscopy
fvDOM: Finite volume discrete ordinate model
HCE: Hemicellulose
HITRAN: High-resolution transmission molecular absorption database
HRR: Heat release rate
ICL: Inter-band cascade lasers
IR: Infrared
LAS: Laser absorption spectroscopy
LDV: Laser doppler velocimetry
LES: Large eddy simulation
LIG: Lignin
MARS: Model automatic reduction software
MC: Moisture content
MLC: Mass loss calorimeter
NIST: National Institute for Standards and Technology
NSCBC: Navier-Stokes characteristic boundary condition
OPO: Optical parametric oscillators
PIMPLE: PISO-SIMPLE algorithm
PISO: Pressure implicit with splitting of operator
PIV: Particle image velocimetry
PM: Particulate matter
PNNL: Pacific Northwest National Laboratory
PPLN: Periodically poled lithium niobate
PPML: Pseudo perfectly matched layer
PSR: Perfectly stirred reactor
QCL: Quantum cascade lasers
RT: Rayleigh Taylor
SA: Senstivity analysis
SGS: Subgrid scale
SIMPLE: Semi-implicit method for pressure-linked equations

SLPM: Standard liters per minute
SNR: Signal-to-noise ratio
TANN: Tannin
TGL: Triglyceride
TVD: Total variation diminishing
URANS: Unsteady Reynolds averaged Navier Stokes
WUI: Wildland-urban interface

List of Figures

Figure ES-1: Temperature (left), CH4 (middle), and H2O (right) fields near the methane inflow for a methane pool fire with air co-flow using infinitely fast chemistry up to 6 s. The methane inflow occurs between 0.2 and 0.3 m, and the computational domain size is 1024 × 4096, giving a grid resolution of less than 0.5 mm.

Figure ES-2: Instantaneous fields of density, ρ, in x − z (top row) and x − y (bottom row) planes at five different times in the R5 simulation. The x − z fields are taken along the y = 0 centerline, and the x − y fields are taken at z = 0.2 m. Regions of grid refinement in each panel are indicated by gray lines that become increasingly dark with increasing refinement level; it should be noted that these lines show the locations of different refinement levels, but do not show the grid itself, which is much denser.

Figure ES-3: Strouhal number as a function of Richardson number for the present simulations and prior experiments from Hamins et al. 1992, Cetegen & Kasper 1996, Cetegen et al. 1998, Bharadwaj & Das 2017 and Bharadwaj & Das 2019 (see legend in (a)). In (b), we also show the least squares fit to all data (cyan dash-dot line), the linear stability analysis result from Bharadwaj & Das 2017 (magenta dashed line), as well as the proposed relationship (solid black line).

Figure ES-4: Instantaneous temperature fields and meshes for (a) static and (b) AMR small-scale pool fire verification cases. Regions of low temperature are colored in black and regions of high temperature are colored in white. A linear black- orange-white colormap is used in between.

Figure ES-5: Path and time-averaged gas phase temperature statistics from simulation and LAS measurements using the baseline case with 240 rpm blower speed, 0∘ tunnel tilt, and 6 SLPM methane inflow rate.

Figure ES-6: Maximum temperature in an opposed-jet diffusion flame as a function of maximum strain rate for detailed (solid lines), Skeletal-A (dashed lines), Skeletal-B (dotted lines), and Skeletal-C (dash-dot lines) models.

Figure ES-7: Gas-phase temperature (a) and cumulative mass loss (b) during pyrolysis and combustion compared to experimental measurements nominally taken at 4 mm. Clouds surrounding data provide measurements at ±2 mm from nominal measurement height. The simulation contains only CH4 and utilizes infinitely fast chemistry for combustion.

Figure ES-8: Representative plots of surface temperature, mass loss, mass flux, gaseous temperature and water mole fraction for three samples with varying moisture content: (a) 0.7% (b) 11.9% (c) 43.4%.

Figure ES-9: 20-s time-resolved species concentrations and gas temperature derived from the DCS measurements. Species concentrations are normalized by the natural abundance used in the HITRAN database. The species are grouped by the process which governs their production (and hence trend), with species predominantly produced from smoldering combustion on the left and species produced from pyrolysis on the right. Uncertainty bars are calculated from uncertainty in

pressure measurement, statistical fit uncertainty, and saturation threshold (varied from 0.15 to 0.25).

Figure ES-10: Images of the WindCline in both tilt-up (left) and tilt-down (right) configurations.

Figure ES-11: (a) visual representation of the computational domain for the tree fire spread case, showing the initial fire line (red) and tree grouping (grey) with respect to the fuel bed (green) and gaseous domain; (b) visualization of fire spread, where fire is represented by a volume render of temperature from low (black) to hot (orange).

Figure 1: Physical and chemical processes occurring at sub-meter scales during wildland fire combustion. A wildland fire will spread if the radiated and convected heat from the burning fuel is sufficient to evaporate the moisture in nearby live fuels, to pyrolyze the resulting dry fuel, and finally to ignite the combustible pyrolysis gas products. If heat release from the combustion is sufficiently high, then new surrounding live fuels will repeat the same process and the fire will spread.

Figure 2: Hierarchical structure between oxidation mechanisms for hydrocarbons.

Figure 3: Progression of the temperature field for a methane pool fire with air co-flow using infinitely fast chemistry up to 6 s. The methane inflow occurs between 0.2 and 0.3 m, and the computational domain size is 1024 × 4096, giving a grid resolution of less than 0.5 mm. White dashed lines show the start of the PPML regions.

Figure 4: Temperature (left), CH_4 (middle), and H_2O (right) fields near the methane inflow for a methane pool fire with air co-flow using infinitely fast chemistry up to 6 s. The methane inflow occurs between 0.2 and 0.3 m, and the computational domain size is 1024 × 4096, giving a grid resolution of less than 0.5 mm.

Figure 5: Progression of the CH_4 field for a methane pool fire for one second. Pockets of CH_4 can travel up to 1 m from the infinite pool at the bottom of the domain. Although these are small amounts of methane, upon burning they create pockets of hot products that could, in a real wildfire scenario, ignite a previously unburned reservoir of fuel.

Figure 6: Instantaneous fields of density, ρ, in $x - z$ (top row) and $x - y$ (bottom row) planes at five different times in the *R*5 simulation. The $x - z$ fields are taken along the $y = 0$ centerline, and the $x - y$ fields are taken at $z = 0.2$ m. Regions of grid refinement in each panel are indicated by gray lines that become increasingly dark with increasing refinement level; it should be noted that these lines show the *locations* of different refinement levels, but do not show the grid itself, which is much denser.

Figure 7: Time and azimuthal averages of (a–c) axial velocity, (d–f) axial velocity variance, (g–i**)** helium mass fraction, and (j–l**)** helium mass fraction variance as functions of radial position (*r*) at three different heights above the base of the plume: 0.2 m (left column), 0.4 m (middle column), and 0.6 m (right column). Experimental results from O'Hern et al. 2005 are indicated by open circles. Computational results are shown for *R*1 (low resolution; thin solid black lines) and *R*5 (high resolution; heavy solid black lines) from the AMR simulations, as well as from NIST 2018 (thin dashed red lines), Desjardin et al. 2004 (DOT; thin dotted green lines), Maragkos et al. 2012 & 2013 (MRM; thin dash dot blue lines), Blanquart and Pitsch 2008 (BP; heavy red dashed lines),

Burton 2008 (B; heavy green dotted lines), and Chung and Devaud 2008 (CD; heavy blue dash dot lines).

Figure 8: Isosurfaces of the temperature field as a function of time (snapshots are separated by 0.05 s) for (*a*) a circular buoyant jet; (*b–d*) rectangular buoyant jets with different aspect ratios; (*e*) an equilateral triangle buoyant jet; and (*f*) an annular buoyant jet.

Figure 9: Strouhal number as a function of Richardson number for the present simulations and prior experiments from Hamins *et al.* 1992, Cetegen & Kasper 1996, Cetegen *et al.* 1998, Bharadwaj & Das 2017 and Bharadwaj & Das 2019 (see legend in (*a*)). In (*b*), we also show the least squares fit to all data (cyan dash-dot line), the linear stability analysis result from Bharadwaj & Das 2017 (magenta dashed line), as well as the proposed relationship (solid black line).

Figure 10: Instantaneous temperature fields and meshes for (a) static and (b) AMR small-scale pool fire verification cases. Regions of low temperature are colored in black and regions of high temperature are colored in white. A linear black- orange-white colormap is used in between.

Figure 11: Profiles of the time-averaged vertical velocity along the vertical centerline in the *y* direction for the large-scale pool fire case. Experimental results are shown for the methane pool fire studied by McCaffrey 1979, and prior computational results from Wang et al. 2011 and Maragkos et al. 2017 are indicated by solid black and blue dash-dot lines, respectively.

Figure 12: Profiles of the time-averaged temperature with respect to the ambient temperature along the vertical centerline in the *y* direction for the large-scale pool fire case. Experimental results are shown for the methane pool fire studied by McCaffrey 1979, and prior computational results from Wang et al. 2011 and Maragkos et al. 2017 are indicated by solid black and blue dash-dot lines, respectively.

Figure 13: Instantaneous snapshots from simulations using $-10°$ (first row), $0°$ (second row), $+10°$ inclines, and 3 SLPM (first column), 6 SLPM (second column), and 9 SLPM (third column) methane inflow rates.

Figure 14: Path and time-averaged gas phase temperature statistics from simulation and LAS measurements using the baseline case with 240 rpm blower speed, $0°$ tunnel tilt, and 6 SLPM methane inflow rate.

Figure 15: Schematic of the vertical fire spread case, showing the propane burner in orange, as well as both the panel and gas regions. The orange arrow indicates the direction of gravity.

Figure 16: Visualization of static, AMR, and balanced AMR verification cases. Gas-phase combustion is visualized using volume renders of regions with high HRR for static (left sub-panels), for AMR without balancing (center sub-panels), and AMR with balancing (right sub-panels) vertical panel spread cases at times (a) 1.0 s, (b) 8.0 s. Regions are colored by temperature from low (black) to high (yellow). The computational meshes are visualized in a plane through the center of the domain in each panel.

Figure 17: Comparison of chemical HRR time histories for static, dynamic, and dynamic with balancing cases. HRR is computed from instantaneous mass loss rates from the solid.

Figure 18: Instantaneous gas-phase temperature near the time of peak HRR near the gas-solid interface at 8 s. Panels from top to bottom show profiles at panel heights of $z/H = 0.1$, 0.5, and 0.9, where $H = 2.4$ m is the total height. The transverse location x is normalized by half panel width $L = 0.3$ m.

Figure 19: Time history of chemical heat release rate (HRR) for the two-panel fire spread verification case. Experimental results [43] are shown as black circles and AMR simulation results from fireDyMFoam are shown as red squares.

Figure 20: Number of species as a function of error limit during the reduction of the detailed model using the directed relation graph with error propagation (DRGEP) and sensitivity analysis (SA) method. Dash-dot lines indicate the number of species for the given error limit in skeletal models A (blue lines) and B (red lines) prior to the reaction elimination step (which produces Skeletal-C).

Figure 21: Laminar flame speed for a one-dimensional premixed flame as a function of equivalence ratio φ for detailed (solid lines), Skeletal-A (dashed lines), Skeletal-B (dotted lines), and Skeletal-C (dash-dot lines) models. The reactants were at 300 K and P = 1 atm.

Figure 22: Maximum temperature in an opposed-jet diffusion flame as a function of maximum strain rate for detailed (solid lines), Skeletal-A (dashed lines), Skeletal-B (dotted lines), and Skeletal-C (dash-dot lines) models. The conditions of the opposed-jet configuration were T_{fuel} = 500 K, T_{air} = 300K, and P=1atm.

Figure 23: Gas- and solid-phase meshes, showing the temperature field from low (red, 750 K) to high (white, 1650 K) and the char in the solid (inset) from low (tan, 0) to high (brown, 0.03). Ambient temperature of 300 K is removed to show details of the plume.

Figure 24: Surface temperature (a) and cumulative mass loss (b) during pyrolysis compared to experimental measurements nominally taken at 4 mm. The simulation contains only CH_4 and utilizes infinitely fast chemistry for combustion.

Figure 25: Gas-phase temperature (a) and cumulative mass loss (b) during pyrolysis and combustion compared to experimental measurements nominally taken at 4 mm. Clouds surrounding data provide measurements at ±2 mm from nominal measurement height. The simulation contains only CH_4 and utilizes infinitely fast chemistry for combustion.

Figure 26: Experimental setup showing the configuration of the IR camera (surface temperature), laser beam path (gas-phase temperature and water vapor con- centration), load cell (mass loss), and visual camera (optical images). Not shown is the heat flux gauge. The cone heater uniformly irradiates the sample, while the purge box surrounding the sample holder provides a uniform flow of dry air to purge portions of the laser beam path that are not over the sample.

Figure 27: Representative plots of surface temperature, mass loss, mass flux, gaseous temperature and water mole fraction for three samples with varying moisture content: (a) 0.7% (b) 11.9% (c) 43.4%.

Figure 28: Mass flux before and after ignition as a function of sample moisture content. Mass fluxes represent the average of the time-resolved data encompassed by boxes in Figure 27.

Figure 29: The effect of fuel moisture content on the peak gas temperature measured 3 mm above the sample surface. The inset shows the peak gas temperature data plotted as a function of the measured water vapor concentration in the gases above the sample just prior to ignition.

Figure 30: Top-down view of experimental setup. Components in green dashed boxes are only present for tests in the C–H stretch region.

Figure 31: Recorded absorbance spectra and model fits to obtain species concentrations and temperature. The left panels show the measurement and fit in the 4-5 μm spectral region targeting CO and CO_2 transitions. The right panels show the measurement in the C–H stretch region. The top panels show measured DCS data (red) and the spectral fits (blue). The second row shows the fit residuals. The absorbance model of each constituent in the fit is shown separately below. For the C–H stretch region (right panels), the blue curve in the top panel is the addition of the spectral fit together with the residual absorbance from the m-FID approach.

Figure 32: 20-s time-resolved species concentrations and gas temperature derived from the DCS measurements. Species concentrations are normalized by the natural abundance used in the HITRAN database. The species are grouped by the process which governs their production (and hence trend), with species predominantly produced from smoldering combustion on the left and species produced from pyrolysis on the right. Uncertainty bars are calculated from uncertainty in pressure measurement, statistical fit uncertainty, and saturation threshold (varied from 0.15 to 0.25).

Figure 33: Schematic of the WindCline tilting blow-down wind tunnel.

Figure 34: Images of the WindCline in both tilt-up (left) and tilt-down (right) configurations.

Figure 35: Streamwise velocity profiles measured using PIV at the beginning of the WindCline test section for different blower speeds. Panel (a) shows a wide field of view and panel (b) shows the boundary layer structure.

Figure 36: Optical images of the time averaged flame in the WindCline for three different tilt angles: -10°, 0°, and 10° (left to right). Top panels show the side view and bottom panels show the top-down view. The wind tunnel inflow and burner flow rates were 1.2 m/s and 6 SLPM, respectively.

Figure 37: Gas phase temperature profiles measured using near-IR FCLD in the WindCline for a slope of 0° and inflow and burner flow rates of 1.2 m/s and 6 SLPM, respectively.

Figure 38: Optical images (top row) and blue light filtered images (bottom row) of the instantaneous flame structure and charring pattern in the WindCline for 0° tilt angle. The wind tunnel inflow and burner flow rates were 1.2 m/s and 6 SLPM, respectively.

Figure 39: Time series of CO_2, CO and PM2.5 at the exit of the WindCline during the solid phase flame spread experiment shown in Figure 38.

Figure 40: Visualization of simulation at 1 and 30 s highlighting mesh changes in gaseous and solid regions. The fuel bed and building obstacle are colored by char mass fraction from green (low) to black (high) and brown (low) to black (high), respectively. In the gaseous domain a volume render of high temperature is included to visualize fire propagation. Mesh outlines are provided in each region to illustrate where cells have been added.

Figure 41: (a) Visual representation of the computational domain for the tree fire spread case, showing the initial fire line (red) and tree grouping (grey) with respect to the fuel bed (green) and gaseous domain; (b) Visualization of resulting fire spread, where fire is represented by a volume render of temperature from low (black) to hot (orange).

1. Executive Summary

1.1. Introduction

It has long been a goal of wildland fire research to develop more accurate computational models for predicting the behavior of both catastrophic large fires and prescribed burns. An important challenge in the development of such models, however, has been the daunting task of incorporating the small-scale physics of fuel evaporation, pyrolysis, ignition, and combustion, as well as turbulent convection, into landscape-scale simulations (Mell, McDermott and Forney 2010). Computational models of wildland fire spread can generally be divided into two categories: semi-empirical operational models used for nearly real-time incident response and physics-based models used to understand the dynamics of fire spread (Coen, *et al.* 2006). Although there is a growing trend in wildland fire research towards physics-based models (Sullivan 2009; Mell, McDermott and Forney 2010; Morvan 2011), such models remain limited by the challenge of incorporating the physics of wildland fuel combustion in landscape-scale numerical simulations that are coupled to atmospheric dynamics and weather (Coen, *et al.* 2006). This project has addressed this challenge by using simulations with adaptive mesh refinement (AMR), experimentally calibrated reduced chemical kinetics mechanisms, and frequency comb laser diagnostics (FCLD) to study the physics of wildland fire spread at scales from 1m to below 1mm. The resulting physical insights were then used to improve the accuracy of landscape-scale wildland fire spread simulations using AMR.

1.2. Objectives

The primary objective of this project was to understand and characterize small-scale processes involved in the combustion of solid wildland fuels using the most advanced computational and experimental tools available in modern combustion research. We performed the first simulations of wildland fire spread using AMR enabling us to capture a wide range of spatial scales at a relatively modest computational cost. The simulations incorporated reduced chemical kinetic mechanisms for pyrolysis, ignition, and combustion that were calibrated using laboratory measurements from near-infrared (near-IR) FCLD. The near-IR FCLD system was also used to validate AMR simulations for laboratory scale fires in a novel tiltable wind tunnel—called the "WindCline"— developed during this project. In addition to the near-IR FCLD measurements, which were the first of their kind, we also performed the first mid-IR FCLD measurements of wood fuel evaporation and pyrolysis. The resulting validated AMR-based simulation tools were then used to model fire spread at landscape scales. More specific objectives addressed in this project were the following:

1. Understand and characterize wildland fire spread at scales from roughly 1m to below 1mm using AMR-based simulations to directly resolve relevant fluid and chemical processes.
2. Develop and calibrate reduced chemical kinetics mechanisms for the pyrolysis, ignition, and combustion of wildland fuels.
3. Use FCLD to study wildland fire spread at small scales by providing data for the calibration of reduced chemical mechanisms and for simulation validation.
4. Use insights from the computations and experiments to perform improved simulations of wildland fire spread at landscape scales.

1.3. Technical Approach

This project consisted of a joint computational and experimental effort focused on two configurations. In the first, pyrolysis, ignition, and burning of solid wood samples were measured

and simulated in a mass-loss calorimeter. Different wood types, moisture contents, and radiative fluxes were examined. The resulting experimental data were used to develop and calibrate reduced chemical kinetic models for pyrolysis and gas phase combustion, as well as for validation of the computational simulations. In the second configuration, fire spread was examined in novel tilting WindCline for different fuel types, crossflow wind speeds, and slope angles. Experimental measurements of temperature, water mole fraction, flame height, and spread rate for different conditions were used to validate the simulations. These two configurations were the focus of four inter-connected tasks:

Task 1: Computational investigation of wildland fire spread at small scales – Both static mesh and AMR simulations of wildland fire spread were performed using DNS and LES at scales from 1m down to below 1mm. New reduced chemical kinetics models for evaporation, pyrolysis, ignition, and combustion were implemented in the simulations, and simulations were performed of laboratory-scale fuel beds with a line ignition source for different fuel types, fuel-bed slopes, and ambient conditions.

Task 2: Development of reduced chemical kinetic models for wildland fire combustion – Chemical kinetics codes and automated reduction software were used to study and reduce complex reaction mechanisms for water removal, pyrolysis, and gas phase combustion during solid biomass burning. Parameters in the reduced mechanisms were be calibrated using experimental data from FCLD, and the resulting models were implemented and validated in AMR based simulations.

Task 3: Investigation of wildland fire spread at small scales using FCLD – The processes of evaporation, pyrolysis, ignition, and combustion were examined using FCLD, which have the capability to simultaneously measure temperature, chemical species concentrations, and turbulence intensity. The diagnostics were used for two sets of experiments that: (*i*) Characterized evaporation and pyrolysis processes in fuels subjected to an external radiation source, and (*ii*) Studied the spread of wildland fires at laboratory scales.

Task 4: Physically-accurate simulations of wildland fire spread – Based on the fire-spread insights obtained from the simulations and experiments, a new simulation capability for wildland fire heat transfer was developed, where AMR is used in both solid and gas phases. This capability was demonstrated for larger-scale fire spread approaching landscape scales.

1.4. Results and Discussion

In the following sections we present significant research findings and conclusions for each of the tasks noted in Section 1.3.

1.4.1 Task 1: Computational investigation of wildland fire spread at small scales

1.4.1a Direct numerical simulation of fire dynamics at small scales

Using DNS to directly resolve, with high physical accuracy, small-scale fluid dynamic and chemical processes, we performed simulations of gaseous pool fires coupled with an infinitely fast chemical reaction mechanism. Pool fires are connected to the fundamental structure and dynamics of wildland fires, and, in the DNS, the gaseous pool fire was created with a very low inlet velocity of gaseous methane which simulates an infinite reservoir of fuel with a low velocity air co-flow that helps to encourage the mixing of the fuel and air for the reaction to take place. Further simplifying the problem was the use of an infinitely fast chemical reaction mechanism instead of

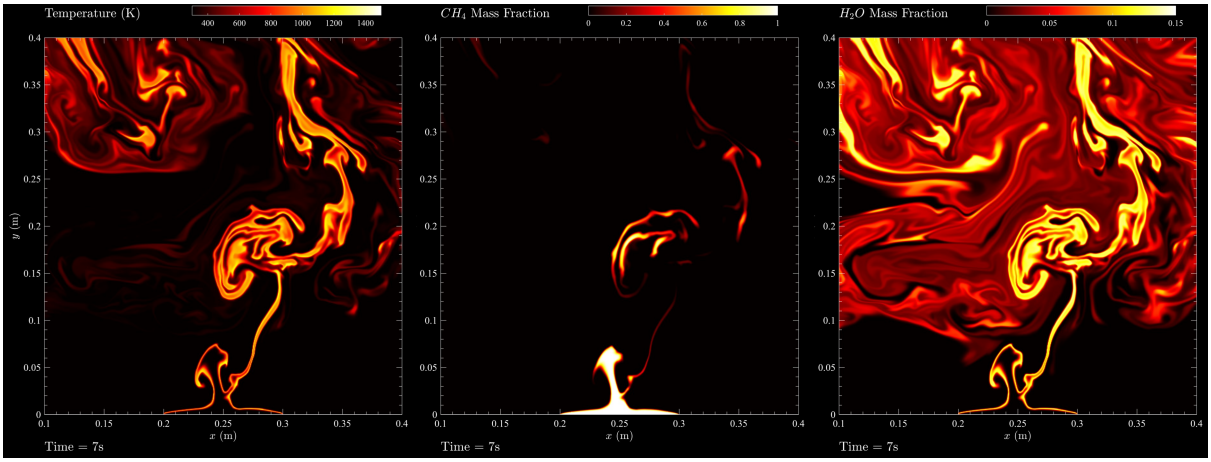

Figure ES-1: Temperature (left), CH_4 (middle), and H_2O (right) fields near the methane inflow for a methane pool fire with air co-flow using infinitely fast chemistry up to 6 s. The methane inflow occurs between 0.2 and 0.3 m, and the computational domain size is 1024 × 4096, giving a grid resolution of less than 0.5 mm.

a more realistic and complex multi-step chemical reaction mechanism. Although detailed chemistry is ultimately desired, it should be noted that an infinitely fast assumption is commonly made. Results such as those shown in Figure 1 indicated that DNS of pool fires was possible, but the computational cost of using a fully compressible code to perform the simulations made it infeasible to perform longer duration simulations of real-world configurations. This motivated subsequent research in this project using low Mach codes and AMR.

1.4.1b Numerical simulations of buoyancy-driven flows using adaptive mesh refinement: structure and dynamics of a large-scale helium plume

The physical characteristics and evolution of a large-scale helium plume were examined through a series of numerical simulations with increasing physical resolution using AMR; Figure 2 shows the progression of the AMR grid at five successive times in the highest resolution simulation. The five simulations each model a 1-m-diameter circular helium plume exiting into a $(4\ \mathrm{m})^3$ domain and differ solely with respect to the smallest scales resolved using the AMR, spanning resolutions

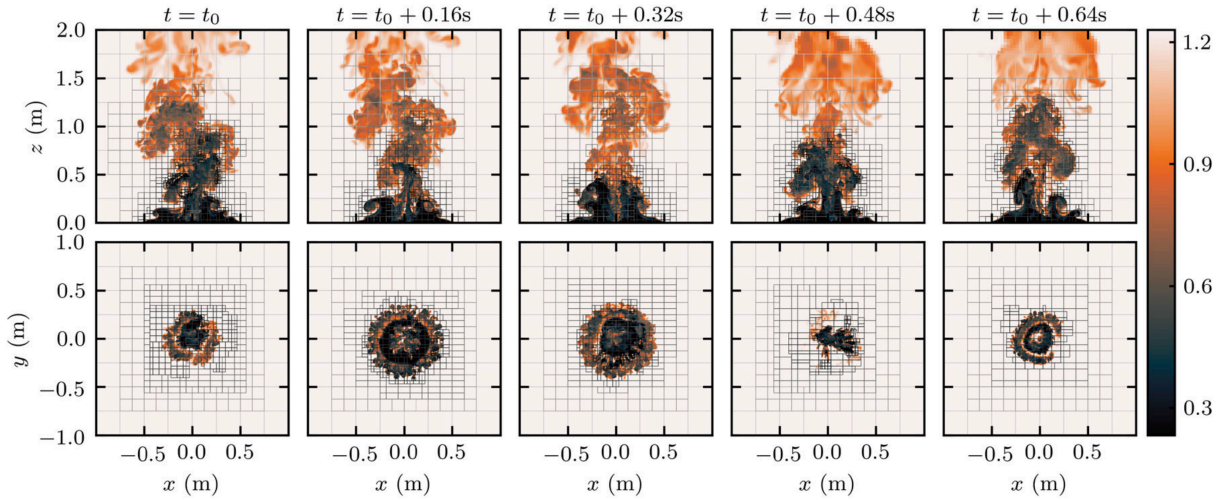

Figure ES-2: Instantaneous fields of density, ρ, in $x - z$ (top row) and $x - y$ (bottom row) planes at five different times in the *R*5 simulation. The $x - z$ fields are taken along the $y = 0$ centerline, and the $x - y$ fields are taken at $z = 0.2$ m. Regions of grid refinement in each panel are indicated by gray lines that become increasingly dark with increasing refinement level; it should be noted that these lines show the *locations* of different refinement levels, but do not show the grid itself, which is much denser.

from 15.6 mm down to 0.976 mm. As the physical resolution becomes finer, the helium–air shear layer and subsequent Kelvin– Helmholtz instability are better resolved, leading to a shift in the observed plume structure and dynamics. A critical resolution is found between 3.91 and 1.95 mm, below which the mean statistics and frequency content of the plume are altered by the development of a Rayleigh–Taylor (RT) instability near the centerline near the plume base. Comparisons were made with prior experimental and computational results, revealing that the presence of the RT instability leads to reduced centerline axial velocities and higher puffing frequencies than when the instability is absent. An analysis of velocity and scalar gradient quantities, and the dynamics of the vorticity, show that gravitational torque associated with the RT instability is responsible for substantial vorticity production in the flow. The grid-converged simulations performed here indicate that very high spatial resolutions are required to accurately capture the near-field structure and dynamics of large-scale plumes relevant to wildland fire dynamics, particularly with respect to the development of fundamental flow instabilities.

1.4.1c Scaling of the puffing Strouhal number for buoyant jets and plumes

Prior research has shown that buoyant jets, plumes, and pool fires 'puff' at a frequency that depends on the balance of momentum and buoyancy fluxes at the inlet, as parametrized by the Richardson number. Experiments have revealed the existence of scaling relations between the Strouhal number of the puffing and the inlet Richardson number, but geometry-specific relations are required when the characteristic length is taken to be the diameter (for round inlets) or width (for planar inlets). Similar to earlier studies of rectangular buoyant jets and plumes, in this study we used the hydraulic radius of the inlet as the characteristic length to obtain a single Strouhal–Richardson scaling relation for a variety of inlet geometries over Richardson numbers that span three orders of magnitude. We used AMR simulations to compute puffing Strouhal numbers for circular, rectangular (with three different aspect ratios), triangular and annular high-temperature buoyant jets and plumes over a range of Richardson numbers. We then combined these results with prior experimental data for round, planar and rectangular buoyant jets and plumes to propose a new scaling relation, shown in Figure 3, that describes puffing Strouhal numbers for various inlet shapes and for hydraulic Richardson numbers spanning over four orders of magnitude. This

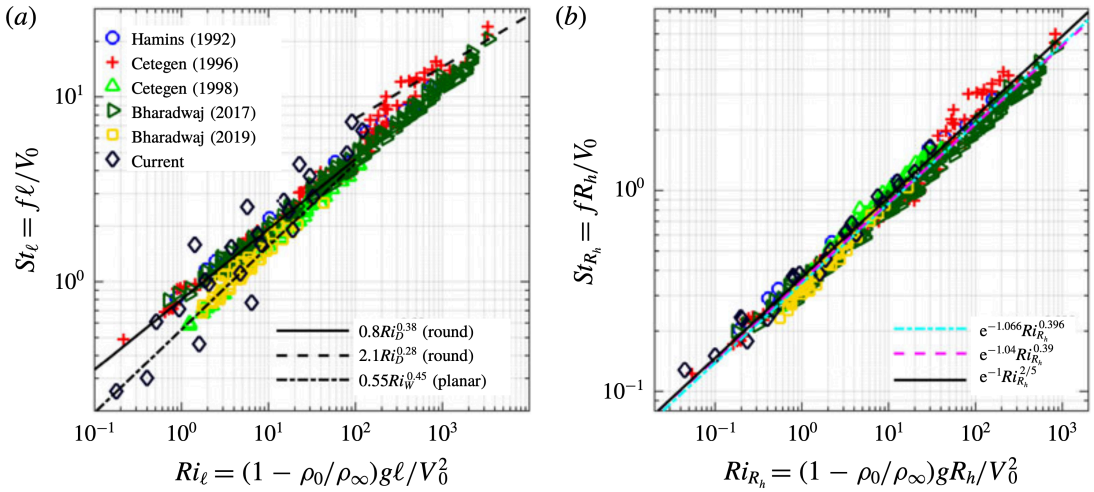

Figure ES-3: Strouhal number as a function of Richardson number for the present simulations and prior experiments from Hamins *et al.* 1992, Cetegen & Kasper 1996, Cetegen *et al.* 1998, Bharadwaj & Das 2017 and Bharadwaj & Das 2019 (see legend in (*a*)). In (*b*), we also show the least squares fit to all data (cyan dash-dot line), the linear stability analysis result from Bharadwaj & Das 2017 (magenta dashed line), as well as the proposed relationship (solid black line).

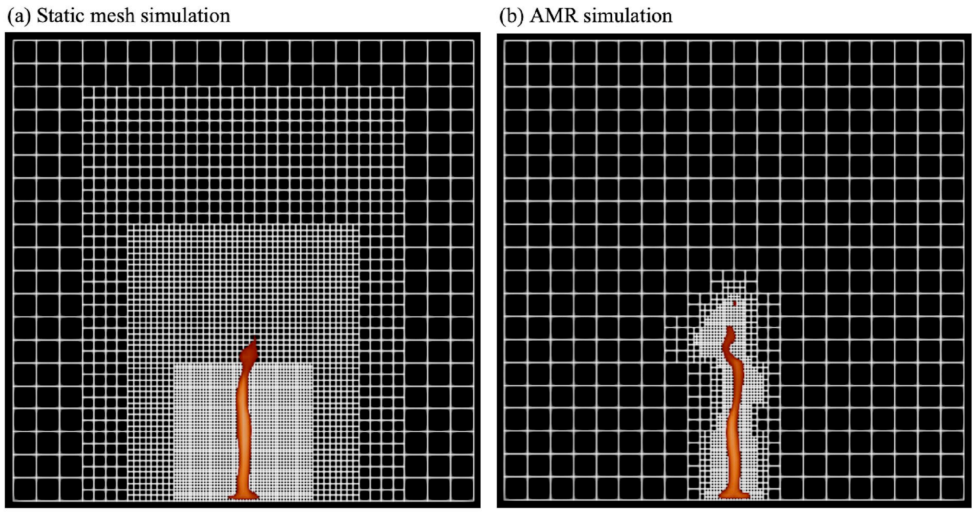

Figure ES-4: Instantaneous temperature fields and meshes for (a) static and (b) AMR small-scale pool fire verification cases. Regions of low temperature are colored in black and regions of high temperature are colored in white. A linear black- orange-white colormap is used in between.

empirically motivated scaling relation is also shown to be in good agreement with prior results from global linear stability analyses.

1.4.1d Efficient simulation of turbulent diffusion flames using adaptive mesh refinement

We addressed the challenge of resolving wide spatial scale ranges in fire simulations through the development of a new OpenFOAM-based AMR computational capability for LES of turbulent diffusion flames. The AMR approach provides increased resolution in localized regions based on user-defined criteria, resulting in a simulation that dynamically tracks fire spread and reduces computational cost compared to uniform and static mesh approaches. The new AMR-enabled solver, called diffusionFireFoam, is an extension of the fireFoam solver and incorporates dynamic meshing capabilities already available in OpenFOAM. We have shown that both first- and second-order statistics from the AMR simulation are in good agreement with results from a statically refined simulation that has the same fine-scale resolution, but a larger overall mesh (see Figure 4). We also showed for a larger-scale methane pool fire that an AMR simulation in diffusionFireFoam agrees with results from static mesh simulations, experiments, and prior computational studies. Once again, substantial computational savings are achieved, with roughly 5 times fewer grid cells in the AMR simulations than in prior static mesh simulations.

1.4.1e Efficient simulations of propagating flames using adaptive mesh refinement

Fires are complex multi-physics problems that span wide spatial scale ranges. Capturing this complexity in computationally affordable numerical simulations for process studies and "outer-loop" techniques (e.g., optimization and uncertainty quantification) is a fundamental challenge in reacting flow research. Further complications arise for propagating fires where a priori knowledge of the fire spread rate and direction is typically not available. In such cases, static mesh refinement at all possible fire locations is a computationally inefficient approach to bridging the wide range of spatial scales relevant to fire behavior. Here we addressed this challenge by incorporating AMR in fireFoam, an OpenFOAM solver for simulations of complex fire phenomena involving pyrolyzing solid surfaces. The AMR functionality in the extended solver, called fireDyMFoam, is load balanced, models gas, solid, and liquid phases, and allows us to dynamically track regions of

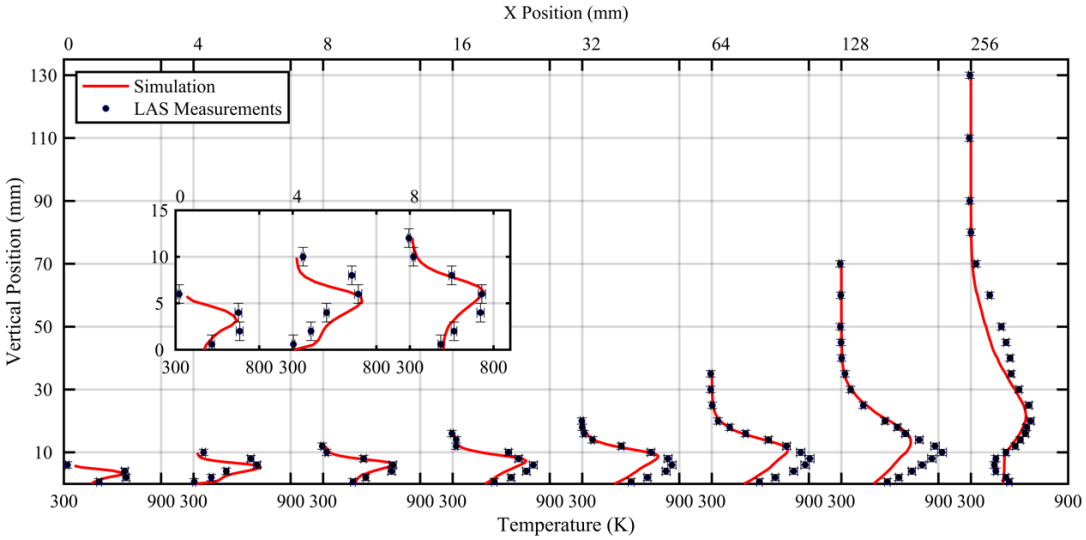

Figure ES-5: Path and time-averaged gas phase temperature statistics from simulation and LAS measurements using the baseline case with 240 rpm blower speed, 0° tunnel tilt, and 6 SLPM methane inflow rate.

interest, thus avoiding inefficient over-resolution of areas far from a propagating flame. We demonstrated the AMR capability and computational efficiency for fire spread on vertical panels, showing that the AMR solver reproduces results obtained using much larger statically refined meshes, but at a substantially reduced computational cost. We then used the solver to perform simulations of diffusion flames in the WindCline, giving good agreement with experimental measurements, as shown in Figure 5.

1.4.2 Task 2: Development of reduced chemical kinetic models for wildland fire combustion

1.4.2a Reduced gas-phase kinetic models for burning of Douglas fir

New skeletal chemical kinetic models were obtained by reducing a detailed model for the gas-phase combustion of Douglas Fir pyrolysis products. The skeletal models are intended to reduce the cost of high-resolution wildland fire simulations, without substantially affecting accuracy. The reduction begins from a 137 species, 4,533 reaction detailed model for combustion of gas-phase biomass pyrolysis products and is performed using the directed relation graph with error propagation and sensitivity analysis method, followed by further reaction elimination. The reduction process tracks errors in the ignition delay time and peak temperature for combustion of gas-phase products resulting from the pyrolysis of Douglas Fir. Three skeletal models are produced by this process, corresponding to a larger 71 species, 1,179 reaction model with 1% error in ignition delay time compared to the detailed model, an intermediate 54 species, 637 reaction model with 24% error, and a smaller 54 species, 204 reaction model with 80% error. Using the skeletal models, peak temperature, volumetric heat release rate, premixed laminar flame speed, and diffusion flame extinction temperatures (see Figure 6) are compared with the detailed model, revealing an average maximum error in these metrics across all conditions considered of less than 1% for the larger skeletal model, 10% for the intermediate model, and 24% for the smaller model. All three skeletal models are thus sufficiently accurate and computationally efficient for implementation in high-resolution wildland fire simulations, where other model errors and parametric uncertainties are likely to be greater than the errors introduced by the reduced kinetic models presented here.

1.4.2b Computationally efficient simulations of Douglas fir pyrolysis and combustion

Numerical simulations have the potential to provide low-cost, low-risk insights into wildland fire structure and dynamics, but simulation accuracy is limited by the difficulty of modeling physical processes that span a wide range of spatial scales. These processes include heat transfer via radiation and turbulent advection, as well as both solid- and gas-phase chemistry. Here we addressed this complexity by using a multi-species chemical kinetic mechanism in simulations with AMR to model the multi-phase pyrolysis of dry Douglas fir. The LES was performed in fireDyMFoam, which is an AMR extension of the OpenFOAM solver fireFoam. Gas-phase and surface temperatures, and mass loss from the simulations were shown to compare favorably with experimental measurements of a small Douglas fir fuel sample undergoing pyrolysis and combustion beneath a cone calorimeter (see Figure 7). Using FCLD, optical and infrared cameras, and a load cell, the experiments provide simultaneous in situ, time-resolved measurements of chemical composition, temperature, and mass loss. This study thus combined cutting edge computational and experimental techniques with multi-step chemical kinetic modeling to provide a validated computational tool for the prediction of solid fuel pyrolysis relevant to wildland fuel combustion.

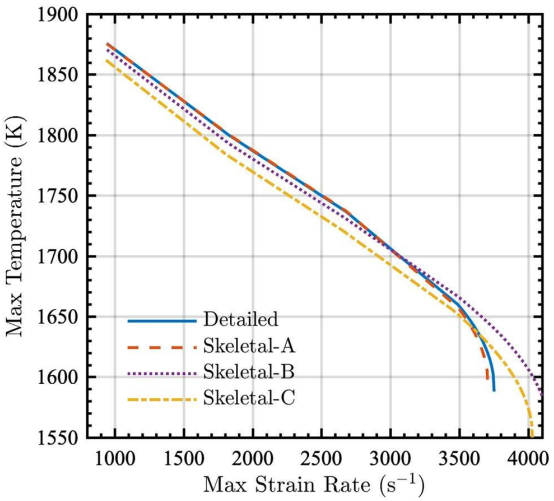

FigureES-6: Maximum temperature in an opposed-jet diffusion flame as a function of maximum strain rate for detailed (solid lines), Skeletal-A (dashed lines), Skeletal-B (dotted lines), and Skeletal-C (dash-dot lines) models.

1.4.3 Task 3: Investigation of wildland fire spread at small scales using FCLD

1.4.3a Dual frequency comb spectroscopy of solid fuel pyrolysis and combustion: Quantifying the influence of moisture content in Douglas fir

As the fire research community develops multi-scale models to predict the spread of wildland fires, there is a need for well-controlled, small-scale experiments which provide benchmark data and fundamental understanding of the effects of key parameters on the combustion of wildland fuels. Here, we implemented a unique suite of non-intrusive, quantitative diagnostics that simultaneously measured mass loss, surface temperature, *in situ* gas temperature and water vapor concentration,

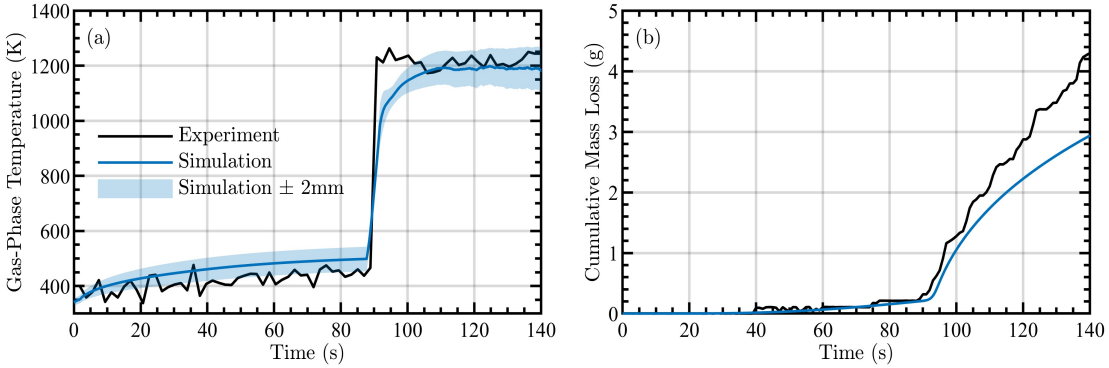

Figure ES-7: Gas-phase temperature (a) and cumulative mass loss (b) during pyrolysis and combustion compared to experimental measurements nominally taken at 4 mm. Clouds surrounding data provide measurements at ±2 mm from nominal measurement height. The simulation contains only CH_4 and utilizes infinitely fast chemistry for combustion.

including the first implementation of dual frequency comb spectroscopy for the study of solid fuels. As a demonstration, we examined the effect of fuel moisture content on the burning of Douglas fir wood samples that were ignited under constant radiative heat flux from a cone calorimeter to provide benchmark data for multi-scale models; results are shown in Figure 8. Peak flame temperatures 3 mm above the sample surface measured with the dual frequency comb laser spectrometer were more than 1200 K. The flame temperature decreases by over 150 K as fuel moisture content increases from 0.7% to 40%. This work demonstrated a platform for simultaneous, quantitative measurements of well-controlled small-scale experiments which provide bench- mark data for the development of simulations capable of capturing the complex physics present in wildland fire systems.

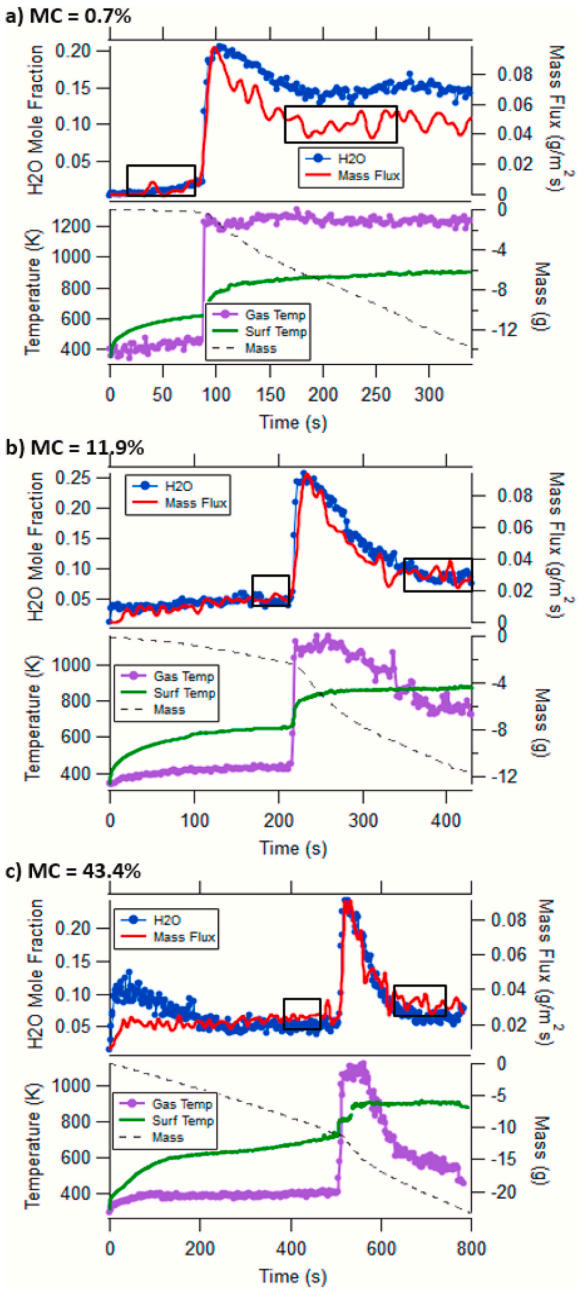

Figure ES-8: Representative plots of surface temperature, mass loss, mass flux, gaseous temperature and water mole fraction for three samples with varying moisture content: (a) 0.7% (b) 11.9% (c) 43.4%.

1.4.3b Mid-infrared dual frequency comb spectroscopy for combustion analysis

We demonstrated the application of mode-locked mid-infrared dual frequency comb spectroscopy for combustion analysis. With two settings of the same dual-comb system, the measurement spans 1500 cm^{-1} from 2.8 to 5 µm with 0.0067 cm^{-1} (200 MHz) point spacing, or almost a quarter-million discrete comb modes. Using this broadband spectrometer, we quantified the pyrolysis and smoldering combustion of wood samples. Specifically, we measured 20-second time-resolved mole fractions of CH_4, H_2O, two isotopologues of CO_2, two isotopologues of CO, ethane, formaldehyde, methanol, formic acid, as well as gas temperature directly above radiatively heated wood samples (see Figure 9). The combination of the fine spectral resolution and the broad bandwidth of the dual-comb spectrometer allows for precise separation of absorption signatures of individual molecules.

1.4.3c Near-infrared dual frequency comb spectroscopy in the WindCline

To mitigate these effects and overcome these challenges, we have designed and built a wind tunnel facility called the WindCline where the wind tunnel structure is mounted on a tilting platform. The tilting platform allows for the investigation of incline effects on flame structure, without compromising flow quality. Two sets of experiments have been performed in the WindCline. In the first

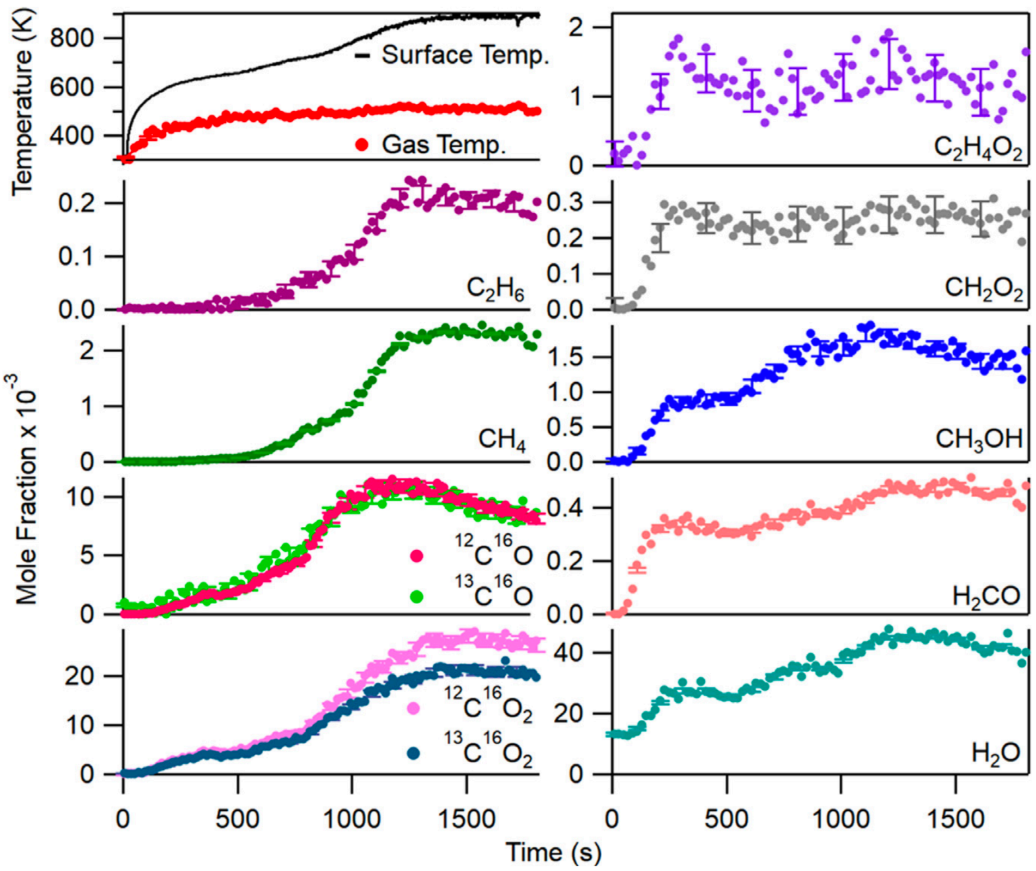

Figure ES-9: 20-s time-resolved species concentrations and gas temperature derived from the DCS measurements. Species concentrations are normalized by the natural abundance used in the HITRAN database. The species are grouped by the process which governs their production (and hence trend), with species predominantly produced from smoldering combustion on the left and species produced from pyrolysis on the right. Uncertainty bars are calculated from uncertainty in pressure measurement, statistical fit uncertainty, and saturation threshold (varied from 0.15 to 0.25).

experiments, a diffusion flame in cross-flow was created by flowing methane through the burner at the bottom of the test section and igniting immediately above the burner. Flame structure was examined for different wind tunnel speeds, burner flow rates, and wind tunnel inclines. The experimental data in Figure

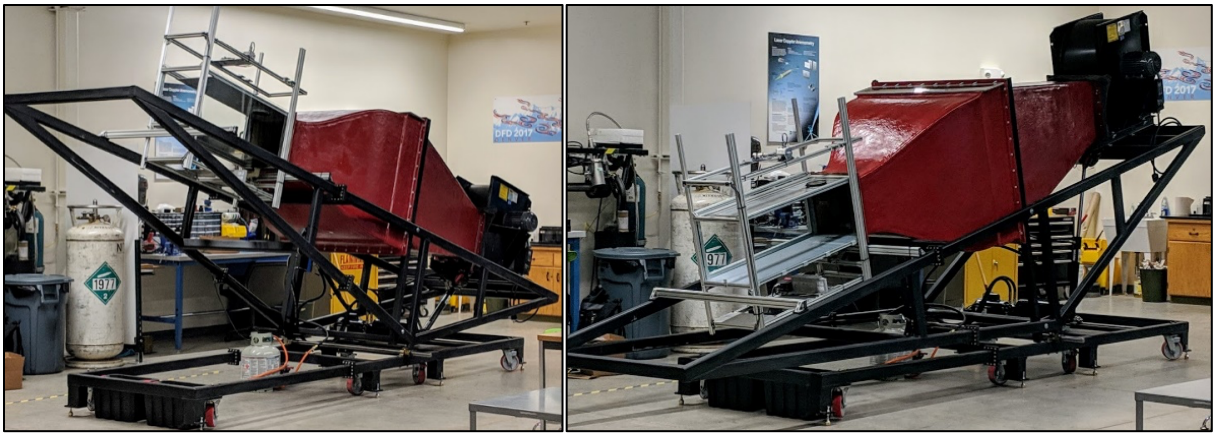

Figure ES-10: Images of the WindCline in both tilt-up (left) and tilt-down (right) configurations.

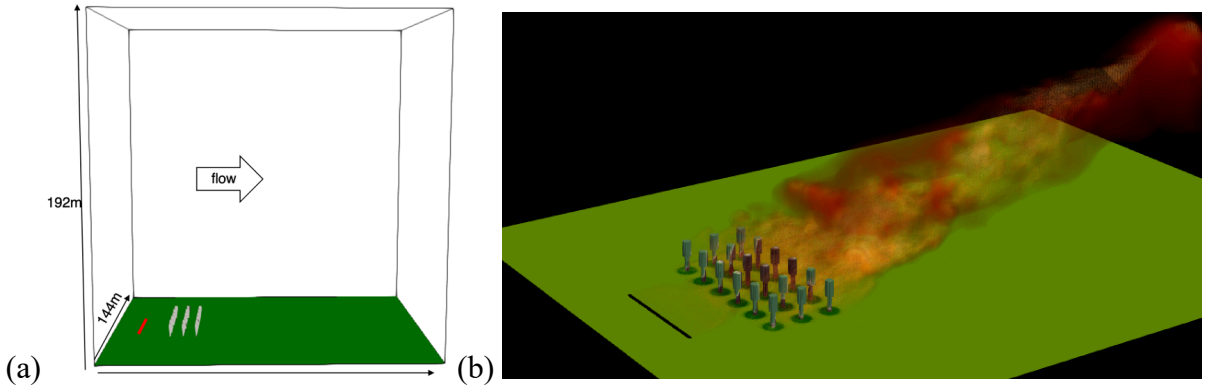

Figure ES-11: (a) visual representation of the computational domain for the tree fire spread case, showing the initial fire line (red) and tree grouping (grey) with respect to the fuel bed (green) and gaseous domain; (b) visualization of fire spread, where fire is represented by a volume render of temperature from low (black) to hot (orange).

5 were obtained using dual comb spectroscopy for one of these conditions. In the second experiment, the metal bottom plate of the test section was replaced with a planed sheet of Douglas fir to measure charring, pyrolysis, and both flame and smoldering combustion in a solid fuel sample.

1.4.4 Task 4: Physically accurate simulations of wildland fire spread

The fireDyMFoam solver has been extended to incorporate AMR in the solid phase to further decrease computational cost. Previously, the solid regions needed to be pre-refined to high resolution to enable use of AMR; this constraint has been relaxed. Additionally, solid modeling has been generalized to enable fully 3D modeling. Arbitrary mesh interface (AMI) coupling is employed to couple gaseous and solid regions. This solver has been demonstrated for two large-scale, wind-driven fire spread cases, both incorporating gas- and solid-phase AMR to decrease computational cost. The first case is representative of the wildland urban interface (WUI) where a propagating fire interacts (and eventually burns) a building-like structure and AMR is used to achieve meter-scale resolution from a nominal resolution of 16-m. In the second case, the solver is used to model a slightly more complex problem, where a propagating flame interacts with an array of tree-like obstacles. Here we further leverage the utility of AMR to obtain ~0.25-m. resolution from an initial resolution of 16m. Simulation layout highlighting the fireline location with respect to the group of trees is shown in Figure 11(a); spread is again successfully captured and visualized in Figure 11(b).

1.5. Implications for Future Research and Benefits

The combined computational and experimental approach of this project provided unprecedented access to information about chemical species, temperature, and turbulence during the entire pyrolysis, evaporation, ignition, and combustion process, thereby permitting more complete understanding of the physics that must be represented by coarse-scale numerical models of wildland fire spread. The proposed project was also specifically focused on the small-scale behavior of wildland fires and has provided a simulation capability that fills a gap in the current hierarchy of wildland fire computational models. An important outcome of this project was the development of an AMR-based computational capability, which will be of direct benefit for the planning and prediction of prescribed burns. Ultimately, the proposed research has brough together two cutting-edge technologies (AMR and FCLD) for the first time in wildland fire research and the development of new physically accurate but computationally efficient simulation tools will have a substantial impact on capabilities for understanding and predicting the behaviors of both catastrophic and prescribed burns.

2. Introduction and Objectives

It has long been a goal in wildland fire research to develop more accurate computational models for predicting the behavior of both catastrophic large fires and prescribed burns. An important challenge in the development of such models, however, has been the daunting task of incorporating the small-scale physics of fuel evaporation, pyrolysis, ignition, and combustion, as well as turbulent convection, into landscape-scale simulations (Mell, McDermott and Forney 2010).

The primary objective of this project was to understand and characterize these small-scale processes using the most advanced computational and experimental tools available in modern combustion research. We performed the first simulations of wildland fire spread using adaptive mesh refinement (AMR), enabling us to capture up to four orders of magnitude in spatial scale separation, at a relatively modest computational cost. The simulations incorporated reduced chemical kinetic mechanisms for pyrolysis, ignition, and combustion that were calibrated using laboratory measurements from near-infrared (near-IR) frequency comb laser diagnostics (FCLD). The near-IR FCLD system was also used to validate AMR simulations for laboratory scale fires in a novel tiltable wind tunnel—called the "WindCline"— developed during this project. In addition to the near-IR FCLD measurements, which were the first of their kind, we also performed the first mid-IR FCLD measurements of wood fuel evaporation, pyrolysis, ignition, and combustion. The resulting validated AMR-based simulation tools were then used to model fire spread at landscape scales. More specific objectives addressed in this project were the following:

1. Understand and characterize wildland fire spread at scales from roughly 1m to below 1mm using AMR-based simulations to directly resolve relevant fluid and chemical processes.
2. Develop and calibrate reduced chemical kinetics mechanisms for the pyrolysis, ignition, and combustion of wildland fuels.
3. Use FCLD to study wildland fire spread at small scales by providing data for the calibration of reduced chemical mechanisms and for simulation validation.
4. Use insights from the computations and experiments to perform improved simulations of wildland fire spread at landscape scales.

Through this combined computational and experimental effort, this project addressed the research needs of SERDP and Department of Defense (DoD) fire managers in the following ways:

A. SERDP Research Need: *Improved understanding of open combustion processes at fine to landscape scales with a focus on the flaming and short-term (hours) smoldering phases.*
   - AMR simulations and FCLD were used to examine evaporation, pyrolysis, ignition, and combustion processes involved in wildland fire spread at sub-meter spatial scales and short (roughly 1-10min) time scales.

B. SERDP Research Need: *Improved understanding of fire spread across heterogeneous fuels through either particle-scale or fuel-bed scale type combustion processes.*
   - AMR simulations and FCLD were used to measure the flame dynamics and spread at fuel-bed scales for different fuel types, fuel geometries, and ambient conditions.

C. SERDP Research Need: *Improved understanding of the role of fuel characteristics in the combustion process, including the burning of live fuels (as distinct from dead fuels), and how this affects fuel consumption.*
   - Various fuel types were examined, and these fuels and the processes by which they burn were characterized using measurements from FCLD. These measurements were then used to calibrate reduced chemical reaction mechanisms implemented in the AMR simulations.

Ultimately, the simulations and experiments performed in this project have enabled the development of improved AMR-based computational tools for landscape-scale simulations which will, in turn, benefit predictions of wildland fire spread in both catastrophic and prescribed burn situations.

3. Background

Since 2010, wildland fires have consumed over 29 million acres of timber, grass, and brush in the U.S., equivalent to nearly half the surface area of Colorado (all statistics in this paragraph are from the National Interagency Fire Center 2021). Over the same period, $8 billion was spent on fire suppression by federal agencies and almost 11 million additional acres of wildland fuel were removed through preventative prescribed burns. Nearly two thousand structures were lost as the result of wildland fires in 2014 alone. Moreover, over the coming decades, climate change will contribute to increased wildland fire activity, particularly in the Western U.S. (Westerling, *et al.* 2006).

Despite the enormous prevalence and cost of wildland fires, prediction and understanding of such fires using computational models remains an inexact science. Computational models of wildland fire spread can generally be divided into two categories: semi-empirical operational models used for nearly real-time incident response and physics-based models used to understand the dynamics of fire spread (Coen, *et al.* 2006). Although there is a growing trend in wildland fire research towards physics-based models (Sullivan 2009; Mell, McDermott and Forney 2010; Morvan 2011), such models remain limited by the daunting challenge of incorporating the physics of wildland fuel combustion in landscape-scale numerical simulations that are coupled to atmospheric dynamics and weather (Coen, *et al.* 2006). This project has addressed this challenge by using AMR-based simulations, experimentally calibrated reduced chemical kinetics mechanisms, and FCLD to study the physics of wildland fire spread at scales from 1m to below 1mm. The resulting physical insights were then used to improve the accuracy of landscape-scale wildland fire spread simulations using AMR.

Additional background details are provided in the following sections on computational approaches in combustion and wildland fire modeling, reduced chemical kinetics mechanisms for burning of wildland fuels, and the use of frequency comb laser diagnostics in combustion research.

3.1 Computational Approaches in Combustion and Wildland Fire Modeling

Wildland fires are characterized by enormous spatial and temporal scale ranges, spanning chemical heat release at sub-millimeter and sub-millisecond scales to landscape-scale dynamics occurring over kilometers and minutes to hours. Resolving this full range of scales in a single simulation with a static and uniform computational mesh is currently infeasible using modern computational resources and is likely to remain so for decades to come. As a result, nearly all current landscape-scale simulation efforts seek to reduce computational cost using simplified physics models and limiting the temporal and spatial scales that are explicitly resolved.

Commonly used models employ a variety of different computational approaches. Coupled atmosphere-flame models such as WRF-FIRE (Coen, *et al.* 2006) and FIRETEC (Linn 1997, Linn, *et al.* 2002, Linn, Winterkamp, *et al.* 2011) use relatively coarse computational grids (down to roughly 1m resolution) to model wildland fire spread at landscape scales in what are typically called large eddy simulation (LES) or unsteady Reynolds averaged Navier-Stokes (URANS) approaches. In both LES and URANS, only the largest scales of the flow are directly resolved, and

subgrid-scale models must be used for unresolved scales. Such approaches are unavoidable given the wide range of scales present in wildland fire problems, yet the accuracy of these simulations critically depends on the accuracy of the subgrid-scale models used for unresolved physics. A wide range of fluid dynamic and chemical models have been used at subgrid-scales (e.g., the Smagorinsky (Smagorinsky 1963) or Deardorff (Deardorff 1980) models for turbulent fluctuations and the Rothermal model for flame spread (Rothermal 1972)) but accurately representing all necessary small-scale physics in these models remains a subject of much research in the broader combustion community (Pitsch 2006 has provided a review of subgrid-scale modeling for combustion LES). Computational models at smaller scales such as WFDS (Mell, McDermott and Forney 2010; McGrattan, *et al.* 2007; Mell, *et al.* 2007) and FIRELES (Zhou, Pakdee and Mahalingam 2004, Zhou Mahalingam and Weise 2005, Zhou, Mahalingam and Weise 2007) are also based on the LES approach, where the grid resolution is larger than a centimeter and unresolved subgrid-scale physics must be modeled.

In general, an understanding of relevant small-scale physics is required to develop physically accurate subgrid-scale models, and yet there is a notable omission in the hierarchy of existing simulation approaches; namely, a simulation capability that extends from scales of 1m to below 1mm. Chemical reactions and the actual burning of wildland fuels occur at these scales, and this range is thus fundamental to the very existence of wildland fires. Moreover, in essentially all existing computational frameworks, these scales are below the simulation grid scale.

Methods to decrease temporal-scale separation include infinitely fast chemistry, operator splitting, flamelet libraries, and chemical mechanism reduction to identify quasi-steady state species, either a priori (Kadem, *et al.* 2011) or at run-time (Evans and Milne 1987; Jarvis, *et al.* 2011; Smith, *et al.* 2015). Spatial-scale separation is more difficult to address. Since uniform meshes are not computationally affordable, statically refining regions of interest can alleviate some computational cost if a priori knowledge of such areas is available. However, static refinement will only provide useful results if the regions of interest do not change, which is rarely the case in most real-world fire spread problems. We have addressed these challenges in the proposed project through two approaches: (i) direct numerical simulations (DNS) where all relevant length scales are directly resolved and (ii) OpenFOAM-based AMR simulations where high spatial resolution is only used where it is needed.

With respect to DNS, two notable challenges arise, one practical and the other physical (Mell, McDermott and Forney 2010). The practical challenge arises from the requirement that all relevant physical scales must be directly resolved, which necessarily introduces enormous computational grid sizes. It has been noted (Mell, McDermott and Forney 2010), for example, that understanding wildland fire spread on scales from 1m to 1mm using DNS would require 1 billion grid cells and a large amount of computer memory. However, with the increasing availability of high-performance computational resources and the development of massively parallel computational codes, such large calculations have become a reality in recent years. Consequently, despite the need for large-scale computational resources, DNS is now a feasible option for the study of wildland fire spread at small scales.

The primary physical challenge associated with DNS arises when formulating the governing equations that will be directly solved. These equations should accurately and (to the extent possible) exactly represent real-world fluid and chemical processes occurring at small scales. Although the compressible Navier-Stokes equations governing the fluid dynamics are well understood, appropriate models for chemical processes involved in wildland fire spread are significantly less certain. Models are required for evaporation, pyrolysis, ignition, and combustion

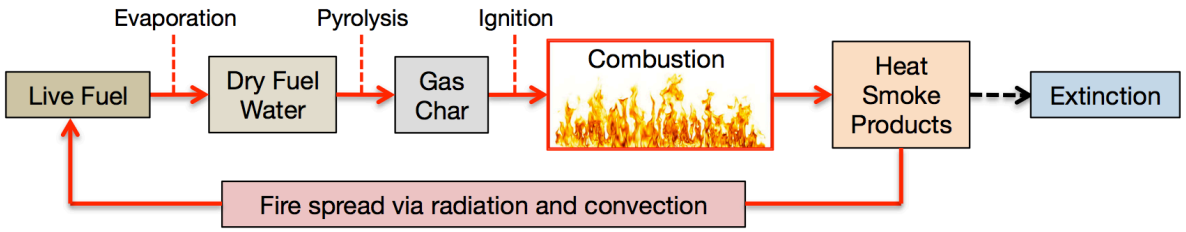

Figure 1: Physical and chemical processes occurring at sub-meter scales during wildland fire combustion. A wildland fire will spread if the radiated and convected heat from the burning fuel is sufficient to evaporate the moisture in nearby live fuels, to pyrolyze the resulting dry fuel, and finally to ignite the combustible pyrolysis gas products. If heat release from the combustion is sufficiently high, then new surrounding live fuels will repeat the same process and the fire will spread.

processes involved in the spread of a fire to unburned live fuels (Figure 1 shows a schematic of these processes). Complex models for these processes have been proposed, but it is important to maintain low computational cost in large-scale simulations such as those proposed here, thus requiring the use of reduced chemical kinetics mechanisms. The development of these mechanisms is discussed in the following section.

As an alternative to the computational cost of DNS using fixed computational grids, we have also taken advantage of AMR in this project to add grid cells in regions of high interest and remove cells in regions of low interest. Computational power is thus concentrated where it is needed most, and prior studies (Baker 2018 provides a review) have shown AMR to significantly reduce computational cost. The two primary benefits of AMR in the present context are that: (i) the cost savings enabled by AMR can be used to span a much wider spatial scale range than is typically possible, and (ii) since a priori knowledge of where a fire is going and how it will spread is often unavailable, dynamically tracking the flame will benefit predictive capabilities while further avoiding the cost of over-resolving regions of lesser interest.

3.2 Chemical Kinetics Mechanisms for Wildland Fire Spread

As shown in Figure 1, combustion of wildland fuels involves initial evaporation of water, pyrolysis of the solid material, ignition, and then gas phase combustion of the resulting products. Evaporation involves bringing water in the fuel to its boiling point, and its subsequent transport from the solid through pores in the fuel. It may also involve morphological changes due to steam production contained within cellular structures. Once any water is evaporated, local temperatures can increase enough to result in evaporation of remaining extractive compounds, followed by de-polymerization of the biopolymers lignin, cellulose, and hemicellulose. Depending on combustion severity, the fuel is either entirely consumed or a mostly carbon-based char remains. The rate at which these processes occur depends on fuel structure and composition, size, and local convective and radiative heating rates.

In practice, the overall physics are highly coupled. While water removal is the first step for combustion of live or wet fuels, heat transfer will result in a temperature distribution within the solid so that material near the surface may be pyrolyzing while the interior is still relatively cool. Once gaseous species begin to be produced, they will mix with surrounding air and combustion can occur, increasing the local heat transfer to the solid. As discussed above, the physics of fuel heating and pyrolysis must be coupled with the fluid mechanics of the gas phase. Due to the overall complexity of each step, however, most workers have focused on developing kinetics mechanisms for only one or two aspects of the full wildland fuel burning process. Here we divide the discussion into mechanisms for water removal, pyrolysis, and gas phase chemistry.

• Water Removal: Numerous workers studying wildfire, thermochemical processing of biomass, and wood treatment have investigated the problem of wood drying, primarily using thermo-gravimetric analysis. Theoretically, the removal of water can be treated as coupled heat and mass transfer through porous media, and recent examples of how to model this problem have been outlined by Younsi *et al.* [20] and Kadem *et al*. [21]. Younsi *et al.* [20] solved the coupled energy and mass conservation equations for the wood but treated the effects of the surroundings using Sherwood and Nusselt numbers. Kadem *et al.* [21] performed a comprehensive analysis solving the three-dimensional Navier-Stokes equations along with energy and concentration equations for the surroundings coupled with the energy and mass conservation equations for the solid wood. In both cases, these analyses result in the temperature and moisture distribution in the wood as a function of time.

• Pyrolysis: The production of gas phase products from biomass solids has been studied by exposing fuel samples to heat sources that simulate fire conditions, mainly direct conductive, convective and/or thermal radiation. Thermo-gravimetric analysis has been used extensively, as have drop-type flow reactors and simple furnace arrangements. In seminal work, Evans and Milne 1987 described the molecular character of biomass pyrolysis based on extensive molecular beam/mass spectrometric analysis of pyrolysis products. In their paper, they make the following general observations. At relatively low pyrolysis severity, the primary products are H_2O, CO_2, and CO, along with a large variety of volatile compounds that are mainly oxygenates. As pyrolysis severity is increased leading to secondary chemical processes, the primary volatiles tend to crack, forming lighter C_1-C_5 aliphatics, C_6-C_9 aromatics, aldehydes, ketones, alcohols, and furans. These then tend to break down further into olefins, smaller aromatics and CO, CO_2, H_2, H_2O, and CH_4. Finally, at the highest temperatures (tertiary processes), the products CO, CO_2, H_2, and H_2O appear, with relative concentrations depending on the amount of oxygen available and the C/H/O composition of the biomass. A considerable amount of work has been carried out since Evans and Milne's study. A recent example is that of Jarvis *et al.* (2011) who studied the evolution of gas phase products from white oak using a laminar entrained flow reactor with molecular beam/mass spectrometry diagnostics. Using factor analysis, they were able to divide product species into six classes based on molecular weight and structure.

• Gas Phase Combustion: To model gas phase combustion requires knowledge of the composition of gases exiting the solid fuel following pyrolysis along with the thermodynamic properties of each species and a kinetic reaction mechanism. As discussed above, the set of compounds found is quite large, and most researchers have chosen to take a 'lumped' approach to characterizing the gaseous fuel and describing the chemical kinetics. The dilemma that faces the researcher is that far more is known about pyrolyzate composition than thermodynamic properties and reaction mechanisms and their rates for the larger species. For the lighter fractions such as CH_4 and CO, thermodynamic properties are well known and there exist kinetic mechanisms that have been directly validated based on experimental flame data. For the larger hydrocarbons and oxygenated species, however, thermal decomposition pathways, thermochemical data and reaction rates are not universally available.

Even if a complete kinetic reaction mechanism were known for the gas phase combustion of a given fuel type, inclusion of the mechanism in high-resolution DNS would would be computationally infeasible. Therefore, a reduced reaction mechanism of some kind must be used.

There are two general approaches to developing such reduced mechanisms. One approach is to take the results of a pyrolysis model that predicts the light products of pyrolysis and then reduce an existing mechanism for the gas phase chemistry. In this case, one could start with a well-known mechanism like GRI-Mech (Smith, *et al.* 2015) and reduce to a smaller mechanism as in Zhou *et al.* (2001). The other approach is to identify thermodynamic properties and reaction pathways and rates from more detailed species data such as that generated by Jarvis *et al.* (2011). Then using a hierarchical approach like that outlined by Westbrook and Dryer (1984) and shown in Figure 2 (but with biomolecules added), build on existing mechanisms. An intermediate approach is to characterize classes of molecules (Jarvis' factors, for example) with lumped representative species. This is the approach taken, for example, by Ranzi *et al.* (2018) in developing their gas phase mechanism. A similar approach was employed in the present project.

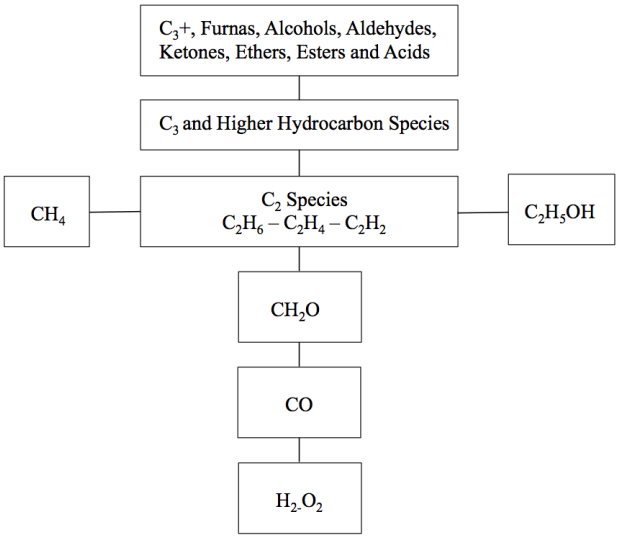

Figure 2: Hierarchical structure between oxidation mechanisms for hydrocarbons.

3.3 Advanced Combustion Diagnostics Based on Frequency Comb Lasers

The development of reduced chemical kinetics mechanisms can be guided, as it was in the present project, by measurements from high-fidelity diagnostics. Species and temperature data are among the most important for developing models of evaporation, pyrolysis, ignition, and combustion, and velocity field data is helpful for understanding turbulent flow properties in fluid dynamics models. Systems based on these diagnostics typically target one or a few species or temperature, where the absorption of laser light by species of interest is quantified to determine species concentrations and temperature. Although additional particle image or laser Doppler velocimetry (PIV or LDV, respectively) using a separate system is necessary to determine velocity fields and turbulence characteristics, laser absorption diagnostics are ideal options for *in-situ* sensing of temperature and species concentrations.

Rather than more traditional single species/parameter laser diagnostic techniques, in this project we instead used frequency comb spectroscopic techniques to simultaneously achieve multi-species, temperature, and turbulence measurements with a single instrument. The instrument was used for controlled measurements of biomass combustion to aid in the development of pyrolysis, ignition, and gas-phase combustion models. Most importantly, unlike traditional PIV or LDV systems, the instrument is ultimately capable of field-deployment, and the same techniques developed here could be used to characterize complex real-world wildland fire combustion environments.

The frequency comb laser is a recent Nobel prize-winning technology pioneered in part at the University of Colorado (Hall 2006). The femtosecond pulsed output of the laser is composed of 100,000+ perfectly spaced, discrete wavelength elements or “comb teeth,” that effectively act as a massively parallel set of continuous wave lasers with well-known frequencies. The frequency

comb can span hundreds of nanometers in various spectral regions (Newbury 2011; Diddams 2010). This broad wavelength span enables simultaneous measurements of multiple species and temperature because the unique temperature-dependent absorption 'fingerprint' for each species can be captured at different wavelengths. Compared with traditional broadband absorption spectrometers like Fourier Transform Spectrometers, comb-based techniques are much faster and have extremely high resolution, which is critical for resolving the characteristic absorption of small molecules in turbulent environments. In this project, we used an approach called dual-comb spectroscopy, which was recently adapted and demonstrated for the first time in a turbulent environment (Rieker, *et al.* 2014). By sending one comb through a turbulent medium and measuring the phase change with the other comb, we can also resolve the turbulence intensity spectrum, which is related to turbulence length scales, to inform model development.

4. Results Overview

In the following sections, we provide an overview of results obtained during this project. The results are divided into topical areas focused on (i) numerical simulations of wildland fire spread at small scales, (ii) development and implementation of reduced chemical kinetic models, (iii) measurements of biomass evaporation, pyrolysis, ignition, and combustion using FCLD, and (iv) AMR-based simulations of landscape-scale wildland fire spread. Where possible, we refer to the reader to the literature for more detail, with a citation to relevant papers provided in the section heading, and several peer-reviewed publications have resulted from this project (Glusman, *et al.* 2019; Lapointe, *et al.* 2020; Makowiecki, *et al.* 2020; Wimer, *et al.* 2020; Wimer, *et al.* 2021; Makowiecki, *et al.* 2021); in such instances, we only present an overview of the methods and key results. In cases where results have not yet appeared in the open literature (e.g., for papers in preparation), we provide as much detail as possible in the present report.

5. Results: Numerical Simulations of Wildland Fire Spread at Small Scales

There was a progression of simulation codes and fidelities throughout this project, beginning with an attempt to perform DNS of fire dynamics at small scales. In this first study, we adapted the fully compressible reacting flow code Athena-RFX to perform simulations of a pool fire with infinitely fast chemistry. However, the fully compressible nature of the code required excessively small computational time-steps, limiting the overall time simulated, and there was little pre-existing functionality for complex geometries and boundary conditions. As a result, we performed subsequent simulations using low-Mach number solvers such as those available in OpenFOAM and PeleLM, to enable the use of larger time steps and simulation of more complex problem configurations. Notably, both codes also allow the use of AMR, which was used to further accelerate the computational simulations.

In the following, we first describe our work with Athena-RFX and then describe two studies of buoyancy driven non-reacting flows using PeleLM. We then outline the development of novel AMR-enabled solvers in OpenFOAM. Ultimately, the AMR solver fireDyMFoam developed in this project was used to perform the simulations of landscape scale fire spread described in Section 7 of this report.

5.1 Direct Numerical Simulations of Fire Dynamics at Small Scales

In a real-world wildland fire, many different factors contribute to the spread and structure of the fire, including wind, weather, terrain, and variable fuel types. This is an incredibly complex

problem that is very difficult to model accurately given the large range of scales. Therefore, for this initial study, a much simpler system – a gaseous pool fire – is analyzed to understand some of the underlying dynamics and structure of wildland fires at small scales. The gaseous pool fire is created with a very low inlet velocity of gaseous methane which simulates an infinite reservoir of fuel with a low velocity air co-flow that helps to encourage the mixing of the fuel and air for the reaction to take place. Further simplifying the problem is the use of an infinitely fast chemical reaction mechanism instead of a more realistic and complex multi-step chemical reaction mechanism. Although detailed chemistry is ultimately desired, it should be noted that an infinitely fast assumption is commonly made.

5.1.1 *Infinitely fast chemistry*

The use of infinitely fast chemistry assumes the chemical reaction timescale is much smaller than that of the advective and diffusive timescales. In low turbulence diffusion flames, this assumption is much less egregious than in premixed combustion or in fluid flows with high levels of turbulent mixing and has been used by others in DNS of reacting flows (Pantano, *et al*. 2003, Doom, *et al*. 2007). This means that the reaction takes place essentially instantaneously as the reactant species (i.e., CH_4 and O_2) meet each other, immediately yielding products of combustion (i.e., CO_2, H_2O, and heat). This global single step reaction is represented for stoichiometric conditions as:

$$CH_4+2O_2+7.58N_2 \rightarrow CO_2+2H_2O+7.58N_2+\text{heat}.$$

In Athena-RFX, this reaction is implemented as:

1. At every time step, we check every grid cell in the domain to determine whether CH_4 and O_2 are both present.
2. If, in any given cell, there exists both CH_4 and O_2, the infinitely fast reaction is activated.
3. We determine which reactant (i.e., CH_4 or O_2) is the limiting reactant based on mole fraction and the stoichiometric reaction above.
4. The limiting reactant is eliminated along with the stoichiometric equivalent of the non-limiting reactant, and products are added in their place according to the above equation.
5. The amount of heat released is always determined by the amount of CH_4 and O_2 that is depleted, regardless of whether it is the limiting reactant.

It should be noted that, since the assumption of infinitely fast chemical reactions is not entirely physical, the heat released is often too large for it to be representative of a real-world reaction, so we have imposed a damping coefficient to prevent the temperatures in the simulation from exceeding that of the adiabatic flame temperature, which for a methane-air reaction is 2200 K.

The idea of a damping coefficient for an infinitely fast chemical reaction mechanism is not a new one, and the FDS from NIST also enforces a damping that is based on the grid resolution of the simulation (McGrattan, *et al.* 2013). Currently, the damping coefficient for Athena-RFX is a constant of 0.25, though a variable damping coefficient more akin to FDS is being considered and the effects of a variable coefficient will be studied in future work.

5.1.2 Governing equations

Numerical simulations are performed using Athena-RFX (Polundnenko and Oran 2010, 2011) a reacting flow version of the fully compressible, multi-physics Riemann solver Athena (Stone, *et al.* 2008, Athena MHD Code Project - https://trac.princeton.edu/Athena/wiki/AthenaEqns). We perform reacting, fully- compressible simulations of methane-air combustion, which requires the solution of the compressible Navier-Stokes equations. For the following simulations, the above equations are solved with an external gravitational field, viscous stresses, thermal conduction, and

diffusion consistent with that of dry air and methane at a pressure of one atmosphere. The viscous stress tensor is a temperature dependent quantity, where the coefficient of viscosity obeys a power-law dependence on temperature. Numerically, the Riemann fluxes were calculated using an HLLC scheme (Gardiner and Stone 2008) and the equations were integrated in time using the directionally unsplit CTU method of Colella (Colella 1990). Additionally, all time advancing was done dynamically with a maximum CFL number of 0.3 to ensure stability of the numerical method (Wimer, *et al.* 2017).

5.1.3 Boundary conditions

For the simulations, there are two different types of boundary conditions: inflow and outflow boundary conditions. The inflow boundary condition is a straightforward, standard boundary condition that requires no additional explanation. The treatment of the outflow boundary conditions, however, is not straightforward and since they are of utmost importance to the accuracy of the simulations, will be discussed in full.

For subsonic fluid flow, pressure waves can travel in both the direction of the bulk fluid flow as well as against this direction. This means that, at the location where the fluid should exit the computational domain, pressure waves should be allowed to travel both into and out of the domain. Therefore, the numerical boundary condition for outflow must mimic the effect that the atmospheric ambient conditions have on the fluid flow. To add to the problem, it has been shown by Poinsot and Lele (1992) that even physically well-posed boundary conditions do not always produce physical results in the subsonic outflow regime and that added numerical stability is often required.

In Athena-RFX, we use a version of the Navier-Stokes Characteristic Boundary Conditions (NSCBC) proposed in Poinsot and Lele (1992) with an added pseudo perfectly matched layer (PPML) (Appelö and Colonius 2009) to deal with the numerical stability problems. Although the NSCBCs work well on their own, there are some minor numerical artifacts capable of influencing the solution in an unphysical manner. The addition of the PPML (sometimes called a 'sponge' damping region) on top of the computational domain takes care of these issues by damping out spurious pressure waves generated by the computation and gently relaxing the flow to ambient conditions. These boundary conditions along with the pseudo-perfectly matched layer have been tested and validated using a two-dimensional turbulent buoyant jet and are reported in (Wimer, *et al.* 2017).

5.1.4 Physical setup

The physical problem under investigation is a two-dimensional methane pool fire with an air co-flow under the influence of gravity and exhausting into an ambient, hydrostatic atmosphere. The computational domain is 0.5 m × 2.0 m, and the width of the methane pool is 0.1 m and is in the center of the domain at the bottom boundary. The co-flow region is treated as an inflow boundary condition on the bottom boundary surrounding the methane pool. The methane has a small inlet velocity of 1 cm/s to simulate a seeping, infinite reservoir of fuel while the air co-flow region has a slightly larger 4 cm/s inlet velocity; both methane and air enter the domain at a temperature of 300 K. The sides and top of the domain are outflow boundary conditions that relax to a co-flow or a hydrostatic state respectively. A grid resolution for this simulation was chosen to be identical to the previous non-reacting study (Wimer, *et al.* 2017) of 1024 × 4096, which results in a resolution of slightly smaller than 0.5 mm. This very fine grid resolution leads to roughly 4 grid cells within the flame of our methane-air infinitely fast combustion mechanism.

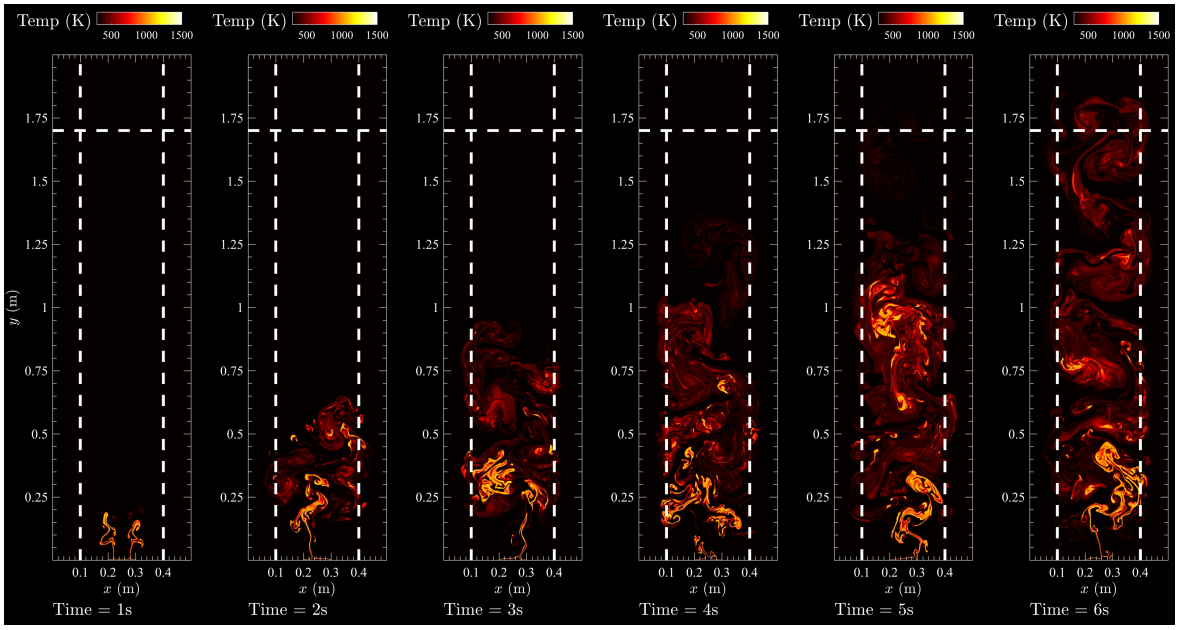

Figure 3: Progression of the temperature field for a methane pool fire with air co-flow using infinitely fast chemistry up to 6 s. The methane inflow occurs between 0.2 and 0.3 m, and the computational domain size is 1024 × 4096, giving a grid resolution of less than 0.5 mm. White dashed lines show the start of the PPML regions.

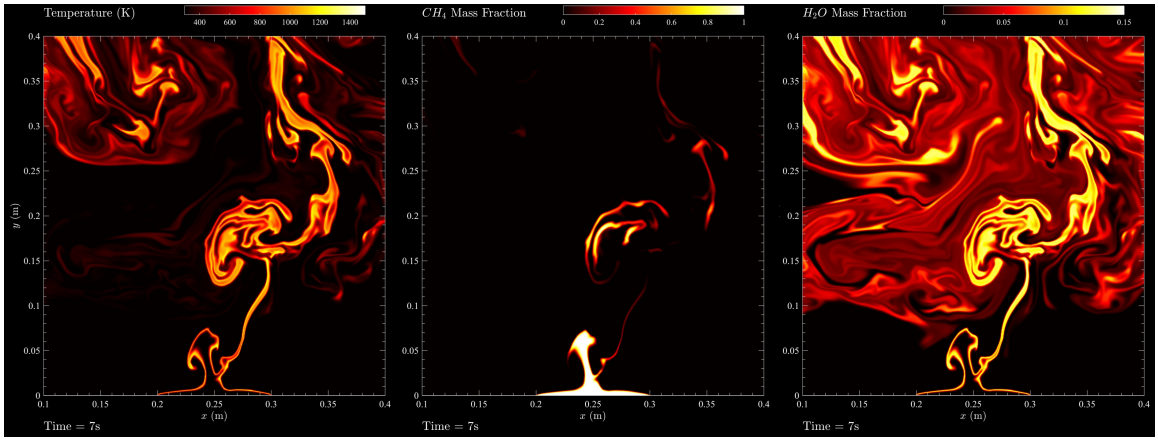

Figure 4: Temperature (left), CH_4 (middle), and H_2O (right) fields near the methane inflow for a methane pool fire with air co-flow using infinitely fast chemistry up to 6 s. The methane inflow occurs between 0.2 and 0.3 m, and the computational domain size is 1024 × 4096, giving a grid resolution of less than 0.5 mm.

5.1.5 Results

Figure 3 shows the time evolution of the temperature field from the methane-air pool fire up to a time of six seconds. The white dashed lines denote the start of the PPML as described in the previous section. As the CH_4 enters the domain, it immediately reacts with the air creating thin puffs of hot products that are visible in the first frame of Figure 3. As the fuel burns, the local temperature increases, leading to an increase in the buoyant force, thereby accelerating and thinning the flame into a meandering 'finger'. As the simulation progresses, the domain begins to be filled with thin structures that are a result of the vortex shedding from the thin flame front.

The thin, high temperature regions shown in Figure 3 are hot products advecting upwards rather than a thinned-out flame front. This can more clearly be seen in Figure 4, which shows a zoomed

view of the temperature field as well as the CH_4 and H_2O mass fractions. Here we can clearly see that most of the fuel is consumed in the first few centimeters of the domain, turning into H_2O and CO_2. Although the combustion looks to be complete low in the domain, there are clearly patches of methane that go unburned and are carried further up in the domain, leading to other patches of high temperature and H_2O mass fraction, as seen in Figure 4. These pockets seem to be formed from the long 'finger' of flame that is stretched until it pinches off the main reservoir. In the process of pinching into a round pocket, the unburnt fuel on the inside can persist for some time as only the edges of the pocket can meet O_2 and react. In a real wildland fire, the advection of pockets of fuel away from the ground can lead to flame 'jumping' as an area of previously un-ignited fuel can catch fire due to the sudden spark of high temperature caused by the burning of floating pockets of fuel.

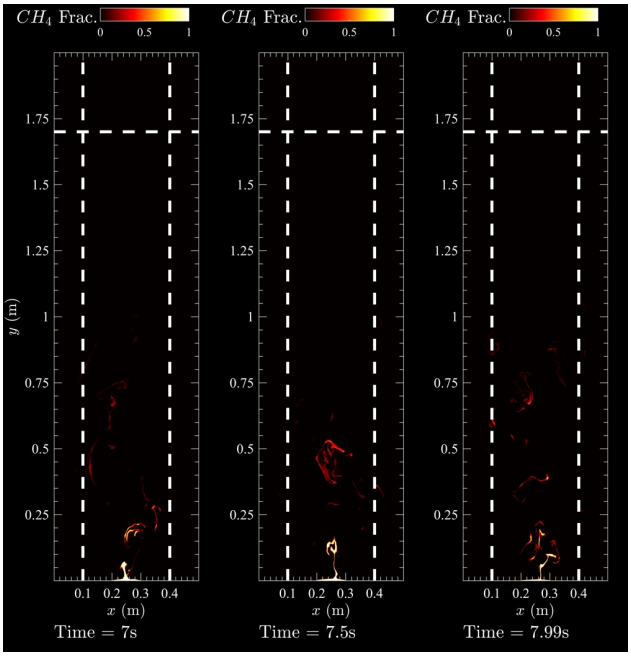

Figure 5: Progression of the CH_4 field for a methane pool fire for one second. Pockets of CH_4 can travel up to 1 m from the infinite pool at the bottom of the domain. Although these are small amounts of methane, upon burning they create pockets of hot products that could, in a real wildfire scenario, ignite a previously unburned reservoir of fuel.

The natural question to answer is then: How far away from the fuel source do these 'pockets' of CH_4 travel? Figure 5 shows small pockets of methane traveling up to 1 m from the infinite pool of methane at the bottom of the domain, which equates to roughly 0.5 s to 1.0 s of lifetime in the domain. When these small pockets of methane meet oxygen, they immediately produce high temperature products that are then accelerated upwards and eventually exit the top of the domain. However, if this were a real-world wildland fire, instead of a 2D simulation, those pockets of unburned fuel from the ground could be blown horizontally and easily ignite another reservoir of fuel some distance away.

Despite this simulation being a substantial simplification of the true wildland fire problem, the preliminary insights obtained here into the dynamics of flame thinning and pinching can be applied to more complex problems. Future work is needed to expand the complexity of the problem by adding a third dimension and more complex chemistry, as discussed in the next section.

5.2 Adaptive Mesh Simulations of Buoyancy Driven Flows (Wimer et al. 2020, 2021)

Buoyancy-driven flows are ubiquitous in nature and engineering, spanning natural phenomena as diverse as thermals in the ocean, volcanic plumes, and wildland fires, as well as engineering applications such as flue gas systems and burners for industrial processing. With the growing availability and decreasing cost of high-performance computing resources, numerical simulations are being increasingly used to study these flows, using LES (e.g., Bastiaans, *et al.* 2000, Zhou, *et al.* 2001a & 2001b, DesJardin, *et al.* 2004, Worthy and Rubini, 2005, Pham, *et al.* 2007, Chung and Devaud 2008, Burton 2008, Blanquart and Pitsch 2008, Maragkos, *et al.* 2012 & 2013, Jatale, *et al.* 2015) and DNS (e.g., Bastiaans, *et al.* 2000, Pham, *et al.* 2007). However, prior attempts to

reproduce experimental results for larger-scale buoyancy- driven flows, particularly in the context of LES for meter-scale plumes and pool fires (Brown, *et al.* 2018), have proved difficult, limiting the use of simulations for the understanding and design of many real-world systems. The reasons for this lack of success are still not fully understood but may be attributable to overly simplistic representations of experimental configurations, inadequate knowledge of experimental initial and boundary conditions, inadequate spatial resolution in simulations, or inaccurate computational models for fluid properties and subgrid-scale (SGS) quantities. Likely, discrepancies between experimental and computational results are a combination of several or all these causes.

In the present study, we partially address these discrepancies by performing a series of high-fidelity computational simulations of a large-scale forced helium plume at different grid resolutions. The simulations are used here to examine the structure and dynamics of buoyancy-driven flows but can also be used for the future development and validation of SGS models. Most notably, the present computations have clearly defined initial and boundary conditions, avoid the use of SGS models, and are grid-converged up to second-order velocity and helium mass fraction statistics. Particular attention is paid to the spatial resolution required to accurately capture the dominant plume dynamics in the absence of an SGS model, and we show that the necessary resolution is between 3.91 and 1.95 mm.

The numerical code used to perform the simulations is PeleLM, a low-Mach, adaptive, parallel, reacting flow code developed at Lawrence Berkeley National Laboratory (Almgren, *et al.* 1998, Day and Bell 2000, Bell, *et al.* 2005, Nonaka, *et al.* 2012, Pazner, *et al.* 2016, Nonaka, *et al.* 2018). This code has a long development history and its underlying algorithms have been repeatedly validated over the past two decades and are based on a density-weighted approximate projection algorithm that is second order in space and time. The low-Mach number model incorporates a mixture-averaged diffusion model (Ern and Giovangigli 2004) and the CHEMKIN (Reaction Design 2011) specification for detailed kinetics and thermodynamic relationships of ideal gas mixtures. Advection is treated numerically with an unsplit, multi-dimensional, second-order time explicit Godunov method, using upwinding that is constrained by the equation of state (Colella 1990; Saltzman 1994; Almgren, *et al.* 1998). Diffusion is solved time implicitly with a Crank–Nicolson discretization, and the chemical kinetics are advanced using the backward difference method in DVODE (Brown, *et al.* 1989). These processes are iteratively coupled together using a spectral deferred corrections strategy that incorporates a time-dependent, spatially uniform pressure field. PeleLM is freely distributed via GitHub (https://github. com/AMReX-Combustion/PeleLM), and this distribution includes several convergence cases that demonstrate second-order convergence (in the L2 norm) in standardized nightly regression tests, including inert and reacting flow cases. PeleLM also exhibits exceptional parallel scaling up to 250k cores using a hierarchical parallelism (MPI+OpenMP) strategy.

PeleLM is built on the AMReX (Zhang, *et al.* 2019) library for block-structured AMR. The solution is managed as a nested hierarchy of refined grid levels. Each level consists of a union of rectangular patches with constant mesh spacing and is properly nested within the next coarser level. The coarsest level tiles the entire computational domain, whereas the finest level typically covers only a small fraction of the domain that contains critical fine-scale features. Periodically during the advance, user-supplied error functions identify regions in the evolving solution that require increased resolution, and new refinement levels are generated. After the solution is transferred to these new patches, the old levels are destroyed. On distributed memory hardware, data are distributed at the granularity of the grid patches using a variety of dynamic load balancing strategies. Local work can be further parallelized by exploiting shared memory threaded hardware.

The convergence properties of PeleLM have been thoroughly characterized for low-Mach, high-Karlovitz combustion scenarios in a series of studies by Aspden *et al.* (2011, 2015a, 2015b, 2016, 2017a & 2018b).

Details of the equations solved in the present PeleLM simulations, the adaptive numerical method, and the physical and computational configurations of the simulations are outlined in Wimer *et al.* (2020,2021).

5.2.1 Large-scale helium plume dynamics (Wimer et al. 2021)

The physical characteristics and evolution of a large-scale helium plume have been examined through a series of numerical simulations with increasing physical resolution using AMR. The five simulations each model a 1-m-diameter circular helium plume exiting into a $(4\ \mathrm{m})^3$ domain and differ solely with respect to the smallest scales resolved using the AMR, spanning resolutions from 15.6 mm down to 0.976 mm (Figure 6 shows the progression of the plume and AMR grid for the finest resolution case). As the physical resolution becomes finer, the helium–air shear layer and subsequent Kelvin-Helmholtz instability are better resolved, leading to a shift in the observed plume structure and dynamics. A critical resolution is found between 3.91 and 1.95 mm, below which the mean statistics and frequency content of the plume are altered by the development of a Rayleigh–Taylor (RT) instability near the centerline near the plume base. Comparisons were made with prior experimental and computational results (see Figure 7), revealing that the presence of the RT instability leads to reduced centerline axial velocities and higher puffing frequencies than when the instability is absent. An analysis of velocity and scalar gradient quantities, and the dynamics of the vorticity, show that gravitational torque associated with the RT instability is responsible for substantial vorticity production in the flow. The grid-converged simulations performed here indicate that very high spatial resolutions are required to accurately capture the near-field structure and dynamics of large-scale plumes, particularly with respect to the development of fundamental flow instabilities.

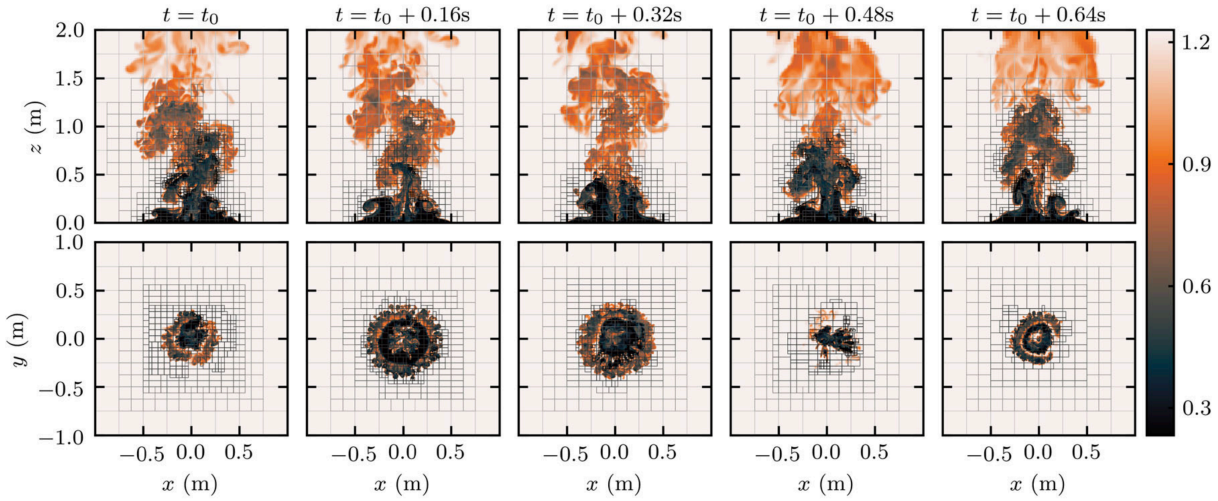

Figure 6: Instantaneous fields of density, ρ, in $x - z$ (top row) and $x - y$ (bottom row) planes at five different times in the *R5* simulation. The $x - z$ fields are taken along the $y = 0$ centerline, and the $x - y$ fields are taken at $z = 0.2$ m. Regions of grid refinement in each panel are indicated by gray lines that become increasingly dark with increasing refinement level; it should be noted that these lines show the *locations* of different refinement levels, but do not show the grid itself, which is much denser.

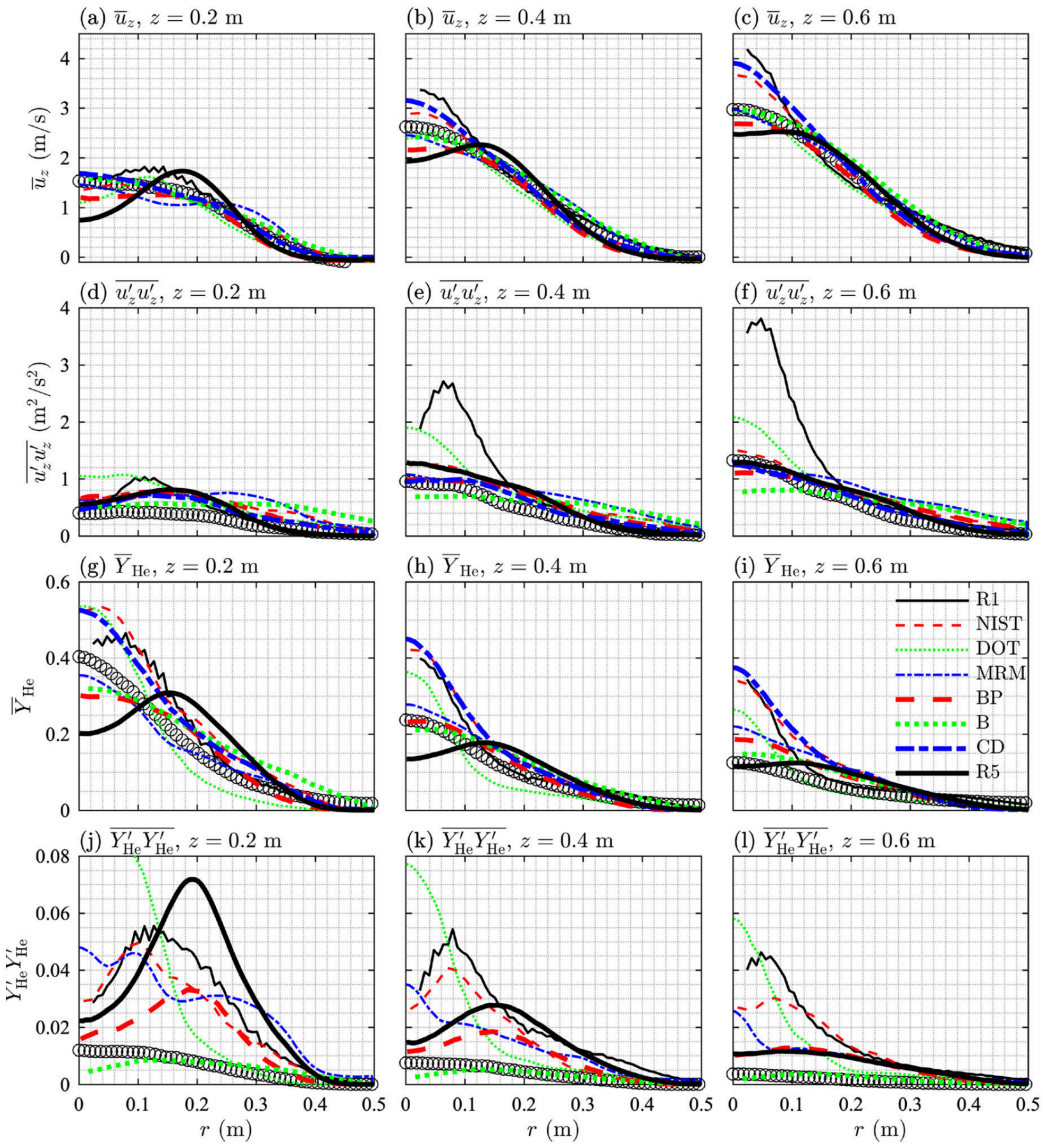

Figure 7: Time and azimuthal averages of (a–c) axial velocity, (d–f) axial velocity variance, (g–i) helium mass fraction, and (j–l) helium mass fraction variance as functions of radial position (r) at three different heights above the base of the plume: 0.2 m (left column), 0.4 m (middle column), and 0.6 m (right column). Experimental results from O'Hern et al. 2005 are indicated by open circles. Computational results are shown for *R*1 (low resolution; thin solid black lines) and *R*5 (high resolution; heavy solid black lines) from the AMR simulations, as well as from NIST 2018 (thin dashed red lines), Desjardin et al. 2004 (DOT; thin dotted green lines), Maragkos et al. 2012 & 2013 (MRM; thin dash dot blue lines), Blanquart and Pitsch 2008 (BP; heavy red dashed lines), Burton 2008 (B; heavy green dotted lines), and Chung and Devaud 2008 (CD; heavy blue dash dot lines).

5.2.2 Scaling of the puffing Strouhal number for buoyant jets and plumes (Wimer et al. 2020)

Prior research has shown that buoyant jets and plumes "puff" at a frequency that depends on the balance of momentum and buoyancy fluxes at the inlet, as parameterized by the Richardson number. Experiments have revealed the existence of scaling relations between the Strouhal number of the puffing and the inlet Richardson number, but geometry-specific relations are required when the characteristic length is taken to be the diameter (for round inlets) or width (for planar inlets).

Here we instead use the hydraulic radius of the inlet as the characteristic length, resulting in a single Strouhal-Richardson scaling relation for a variety of inlet geometries.

We use adaptive mesh numerical simulations to measure puffing Strouhal numbers for circular, rectangular (with three different aspect ratios), triangular, and annular high-temperature buoyant jets over a range of Richardson numbers (see Figure 8). The computational domain for each simulation consisted of a 128 × 128 × 128 base grid with two levels of AMR. The grid was re-meshed every time step to maintain sufficiently fine resolution in regions with large vorticity and density gradient magnitudes, and to reduce resolution in regions where magnitudes were small. With two levels of AMR, the smallest physical scale resolved in the simulations was 1.95 mm, which was recently shown to be sufficiently fine for accurate resolution of the puffing frequency of a large-scale helium plume using an identical numerical approach and similar physical set-up (Wimer*, et al.* 2021).

The bottom boundary in each of the simulations consisted of a high temperature inlet and a mild air coflow. Open boundary conditions were used on the four sides and at the top of the domain. The inlet and coflow were specified using Dirichlet boundary conditions, and the open boundaries were specified using a divergence-constrained velocity projection that allowed for both fluid inflow and outflow. In each of the simulations, hot air with temperature 1000 K flowed from the inlet, and the inlet velocity was varied to span a range of Richardson numbers. The coflow was uniform and the same in all simulations, with velocity 0.05 m/s and temperature 300 K. The gravitational acceleration was directed downwards with magnitude g = 9.81 m/s^2 towards the

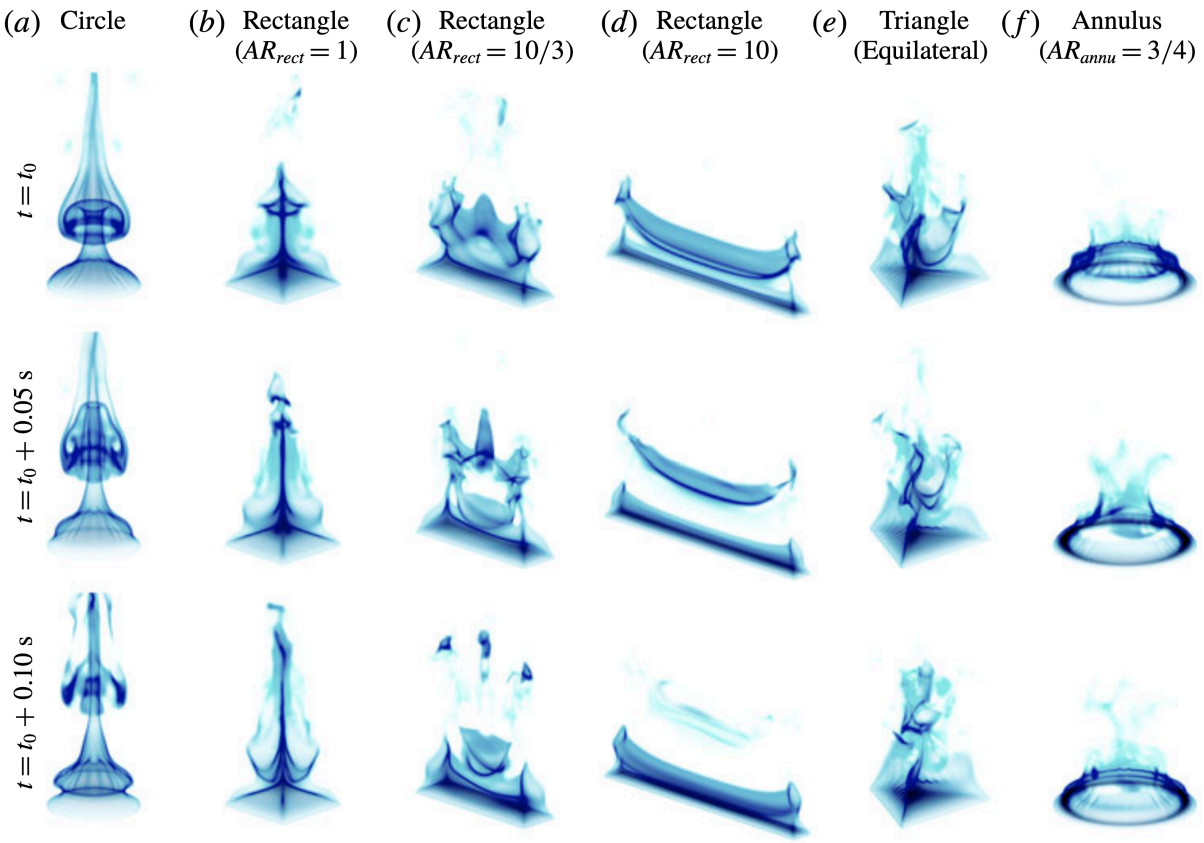

Figure 8: Isosurfaces of the temperature field as a function of time (snapshots are separated by 0.05 s) for (*a*) a circular buoyant jet; (*b–d*) rectangular buoyant jets with different aspect ratios; (*e*) an equilateral triangle buoyant jet; and (*f*) an annular buoyant jet.

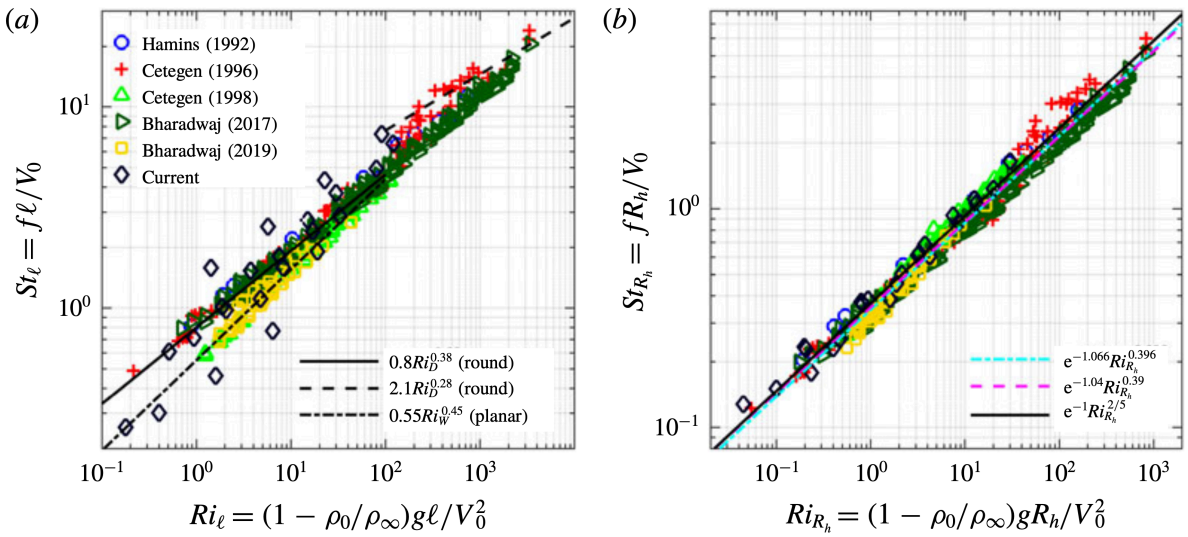

Figure 9: Strouhal number as a function of Richardson number for the present simulations and prior experiments from Hamins *et al.* 1992, Cetegen & Kasper 1996, Cetegen *et al.* 1998, Bharadwaj & Das 2017 and Bharadwaj & Das 2019 (see legend in (*a*)). In (*b*), we also show the least squares fit to all data (cyan dash-dot line), the linear stability analysis result from Bharadwaj & Das 2017 (magenta dashed line), as well as the proposed relationship (solid black line).

bottom boundary along the vertical axis. Each of the simulations were performed for 20 s and statistics were computed over the last 10 s to allow for the decay of initial transients.

Puffing Strouhal numbers for each of the simulations are shown in Figure 9. We then combined these results with prior experimental data for round, planar, and rectangular buoyant jets, and plumes to propose a new scaling relation that describes puffing Strouhal numbers for various inlet shapes and for Richardson numbers spanning over four orders of magnitude (Figure 9). This empirically motivated scaling relation is also shown to be in good agreement with prior results from global linear stability analyses.

5.3 Adaptive Mesh Simulations of Turbulent Diffusion Flames (Lapointe et al. 2020)

Fires in both built and natural environments are multi-scale, multi- physics problems that are enormously difficult to model accurately using numerical simulations. Such simulations are important for process studies and operational predictions required to mitigate fire risk and manage ongoing fires. Although simulations can be financially cheap, low risk, high speed, and multi-dimensional (in both space and time), they are plagued by accuracy concerns and can become prohibitively computationally expensive for large-scale fires involving physical processes spanning several orders of magnitude in spatial and temporal scale ranges. These processes range from chemical heat release at sub- millimeter and sub-millisecond scales to fire spread over tens of meters and minutes (in the case of building fires), or kilometers and hours (in the case of wildland fires).

Because of these challenges, accurately and reliably predicting the structure and dynamics of large-scale fires remains a major research objective for the computational reacting flow community (NIST, 2018). In the present study, we take an important step towards this objective through the development of a new AMR computational capability in OpenFOAM (The OpenFOAM Foundation – openfoam.org, Weller, *et al.* 1998) for LES of turbulent diffusion

flames. The new solver is based on the native OpenFOAM reacting flow solver fireFoam (Gulla 2014, FM Global, FireFoam development repository – github.com/fireFoam-dev/fireFoam-dev 2017) and takes advantage of pre-existing dynamic meshing capabilities in OpenFOAM (Jasak and Gosman 2000a, 2000b & 2000c) for its AMR implementation.

The AMR approach provides increased resolution in localized regions based on user-defined criteria, resulting in a simulation that dynamically tracks fire spread and reduces computational cost compared to uniform and static mesh approaches. The new AMR-enabled solver, called diffusionFireFoam, is an extension of the fireFoam solver and incorporates dynamic meshing capabilities already available in OpenFOAM. We outline details of the new solver and demonstrate its basic functionality, accuracy, and computational efficiency for a small-scale methane pool fire verification case. We show that both first- and second-order statistics from the AMR simulation are in good agreement with results from a statically refined simulation that has the same fine-scale resolution, but a larger overall mesh. We then show for a larger-scale methane pool fire that an AMR simulation in diffusionFireFoam agrees with results from static mesh simulations, experiments, and prior computational studies. Once again, substantial computational savings are achieved, with roughly 5 times fewer grid cells in the AMR simulations than in prior static mesh simulations.

5.3.1 Description of numerical solver

We have developed the new AMR-enabled reacting flow solver in OpenFOAM, which is an open-source computational fluid dynamics software package that encompasses a multitude of solvers for a wide variety of problems, including turbulent reacting and multi-phase flows (The OpenFOAM Foundation – openfoam.org, Weller, *et al.* 1998). The new solver, called diffusionFireFoam, is a combination of the reacting flow solver fireFoam and existing dynamic meshing libraries in OpenFOAM. In the following, we provide background descriptions of fireFoam and dynamic meshing in OpenFOAM, before providing details on how we merged these capabilities in the present study to develop diffusionFireFoam.

The fireFoam solver, originally intended for modeling fire spread and suppression in industrial settings, solves the compressible Navier-Stokes equations in either exact, filtered, or averaged forms, depending on the desired level of fidelity, along with conservation equations for mass, energy, and reacting (or non-reacting) species.

We have developed an extended version of fireFoam, called diffusionFireFoam, that incorporates AMR for LES of fire problems. The new AMR functionality in fireFoam is based on similar functionality in rhoPimpleFoam and interFoam. Although the general framework for the AMR and flux correction already exists in various OpenFOAM solvers, however, significant effort was necessary to ensure that the flux correction used during the AMR was properly performed within the fireFoam LES framework to produce qualitative and quantitative results comparable to those obtained with a static mesh. This effort was concentrated on ensuring mass conservation for newly introduced faces, because mass fluxes are key for computing divergence quantities in the conservation equations. Although enthalpy conservation is also a potential concern, Wang et al. (2011) have previously demonstrated enthalpy conservation using the static mesh version of fireFoam. Because enthalpy is a volumetric quantity and stored at cell centers, it is mapped directly from the old to new mesh (Jasak and Gosman, 2000b), thus ensuring enthalpy conservation during the mesh update, and preserving the conservation properties of fireFoam verified by Wang et al. (2011). As with enthalpy, momentum is also a volumetric quantity and is similarly conserved during the mesh update.

The primary concern during mesh refinement and coarsening is thus to ensure mass conservation, which we achieve in diffusionFireFoam using a flux correction process (based on the original OpenFOAM implementation, used in, e.g., rhoPimpleFoam). The key steps in this process can be summarized as:

1. Store the specific momentum as well as the scalar-valued divergence.
2. Update the computational mesh.
3. Interpolate the stored momentum to the new mesh, yielding an initial mass flux on the new mesh.
4. Solve a Poisson equation to ensure that the flux on the new mesh is identical to the flux from the previous mesh, yielding the final mass flux on the new mesh.

Depending on the time-integration scheme of choice, the steps outlined above may also be necessary to update mass fluxes of prior time steps for the new mesh. A comparison of mass conservation during static mesh and AMR simulations has shown that continuity errors are comparably small in both cases, indicating that the flux- corrected AMR approach does not alter the mass conservation properties of the underlying numerical scheme applied to a static mesh.

We have also extended the AMR functionality in OpenFOAM to refine and coarsen on an arbitrary number of fields (instead of a single field), each with their own bounds (i.e., their own values of *lowerRefineLevel* and *upperRefineLevel*). A set of user-defined fields is scanned individually to identify cells eligible for refinement or coarsening. Then a "master" list of cells for refinement and coarsening is generated by superimposing the individual lists. This new library is used with diffusionFireFoam for the test cases presented in this work. Using AMR, we can significantly reduce computational cost while achieving results comparable to static (i.e., non-AMR) simulations.

The new AMR-enabled diffusionFireFoam solver can be configured in several ways depending on the specific details of a problem and the computational resources available to a user. Although the new solver is designed for maximum flexibility in its setup, in the following sections we provide descriptions of the configurations used in verification and validation tests. It is likely that there are many other configurations that would yield comparable, or even better (in terms of accuracy and efficiency) results, and the present tests are intended primarily to illustrate the potential benefits of the solver, as well as to provide direction for the selection of appropriate AMR configurations in other problems.

As released, the fireFoam solver is typically used to perform LES, and this is also the approach that we take with the AMR-enabled solver diffusionFireFoam. In the gas phase, 3D Favre-filtered compressible Navier-Stokes equations and conservation equations for mass, total enthalpy, and species are solved on a single unstructured computational mesh, where unity Lewis and turbulent Prandtl numbers are assumed.

Depending on the choice of turbulence closure, sub-grid scale (SGS) transport equations may also be necessary to close the governing equations. As in the standard version of fireFoam, we use mixture-averaged density and transport properties; the former is computed using the ideal gas law and the latter are temperature-dependent and computed using empirical correlations. Combustion modeling is assumed to be infinitely fast (for non-premixed flames) and governed by an eddy dissipation model. Radiation modeling is accomplished using a finite volume implementation of the discrete ordinate method, with a prescribed radiative fraction. For a detailed description of the gas phase physical treatment in fireFoam, we refer the interested reader to Wang et al. (2011).

The conservation equations are solved in a segregated manner and coupled using a procedure (i.e., PIMPLE) involving outer SIMPLE iterations and inner PISO correctors (Wang et al., 2011)

Spatial discretization is nominally second-order accurate; total variation diminishing (TVD) schemes are employed for the divergence of conserved scalar quantities, and a stabilized central difference scheme is used for the velocity convective term to aid stability. Additionally, in the interest of stability, enthalpy gradients are limited. Diffusive terms are unbounded and second order with limited non-orthogonal correction. First order Euler integration is used to march forward in time.

5.3.2 Verification and validation results

In Lapointe *et al.* (2020), we show that both first- and second-order statistics from the AMR simulation are in good agreement with results from a statically refined simulation of a pool fire that has the same fine-scale resolution, but a larger overall mesh (Figure 10 shows both static and AMR meshes for this case). We then examined a larger-scale methane pool fire, showing that an AMR simulation in diffusionFireFoam agrees with results from static mesh simulations, experiments, and prior computational studies. Once again, substantial computational savings are achieved, with roughly 5 times fewer grid cells in the AMR simulations than in prior static mesh simulations.

For the larger-scale pool fire, time-averaged centerline vertical profiles of temperature and vertical velocity are compared to similar computational studies and experimental data in Figures 11 and 12, respectively. It should be noted that the temperature plots include both the original thermocouple data and a 20% correction to account for radiation. These results are presented using the empirical scaling relationships determined by McCaffrey (1979). These figures also show results from other fireFoam-based studies by Wang et al. (2011) and Maragkos et al. (2017).

In general, Figures 11 and 12 show that the AMR-based diffusionFireFoam results agree as closely with the experimental data as the two prior simulation studies. Most notably, the AMR results are nearly identical to results from the study by Wang et al. (2011), which used fireFoam with static mesh refinement and similar choices for the numerical algorithms to those used here.

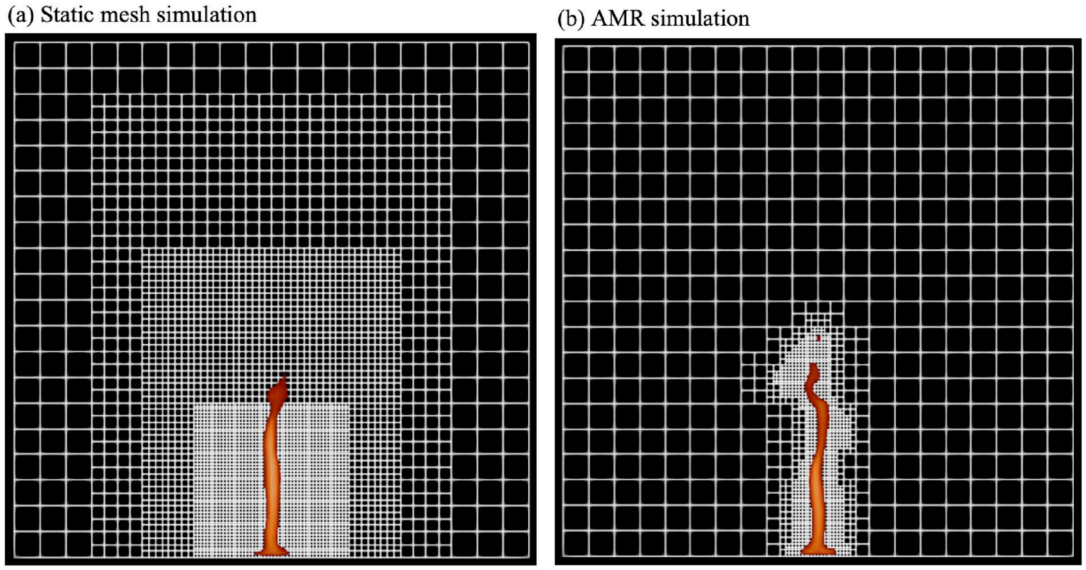

Figure 10: Instantaneous temperature fields and meshes for (a) static and (b) AMR small-scale pool fire verification cases. Regions of low temperature are colored in black and regions of high temperature are colored in white. A linear black- orange-white colormap is used in between.

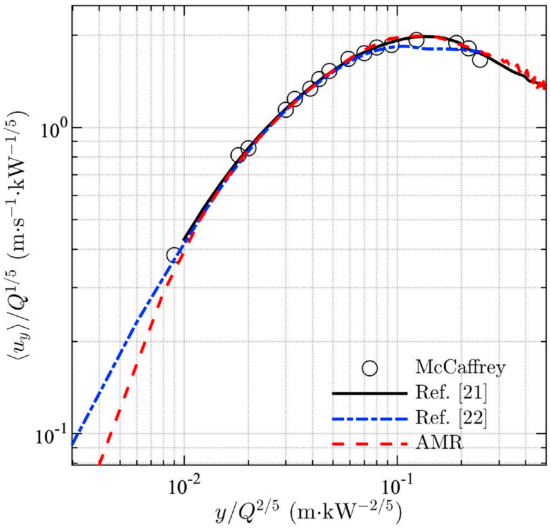

Figure 11: Profiles of the time-averaged vertical velocity along the vertical centerline in the *y* direction for the large-scale pool fire case. Experimental results are shown for the methane pool fire studied by McCaffrey 1979, and prior computational results from Wang et al. 2011 and Maragkos et al. 2017 are indicated by solid black and blue dash-dot lines, respectively.

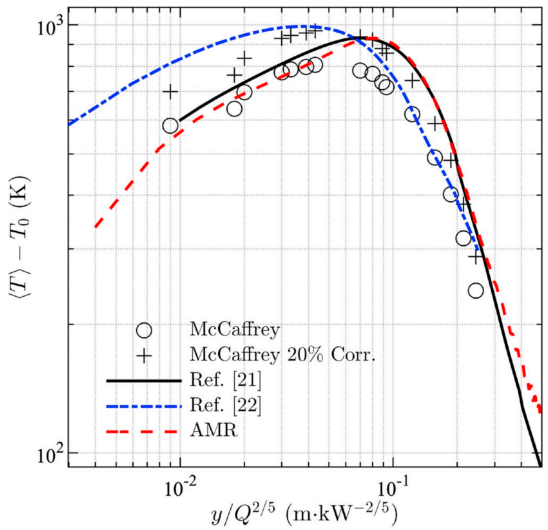

Figure 12: Profiles of the time-averaged temperature with respect to the ambient temperature along the vertical centerline in the *y* direction for the large-scale pool fire case. Experimental results are shown for the methane pool fire studied by McCaffrey 1979, and prior computational results from Wang et al. 2011 and Maragkos et al. 2017 are indicated by solid black and blue dash-dot lines, respectively.

Once again, these results thus indicate that there is no loss of accuracy incurred using AMR in diffusionFireFoam for simulations of pool fires.

With respect to computational cost, the AMR simulation, once spun- up, fluctuated between 85,000 and 100,000 cells. This is substantially lower than prior studies using statically refined meshes (Wang, *et al*. 2011; Maragkos, *et al.* 2017), which had roughly 400,000–500,000 cells (NIST 2018). We are thus once again able to obtain comparable results to statically refined mesh simulations, using AMR to decrease the overall computational cost.

5.3.3 WindCline results

The WindCline experimental apparatus incorporates a variable blower speed wind tunnel (see the description in Section 7.3 of this report) attached to a test section with a methane slot burner at its base. The entire WindCline can be tilted from -18° to 13° to mimic steep terrains and study the effects of such inclines on the spread and propagation of diffusion flames and wildfires in a controlled environment.

Previous modeling efforts made mostly qualitative and visual comparisons to flames observed experimentally. LES using AMR and the eddy dissipation combustion model (EDM) were performed for a range of tilt angles and flow conditions. The results were volume rendered on isosurfaces of temperature and compared to greyscale experimental results using a flame presence probability method to compare simulation and experimental flame structures at various tilt and flow conditions.

This study showed good large scale flame structure (flame angle, length, and contour) agreement between simulation and experiment at the flow and incline conditions shown in Figure 13. A more detailed gas phase temperature analysis was performed to quantitatively describe the flame temperature field. Comparisons were made to path and time-averaged laser absorption

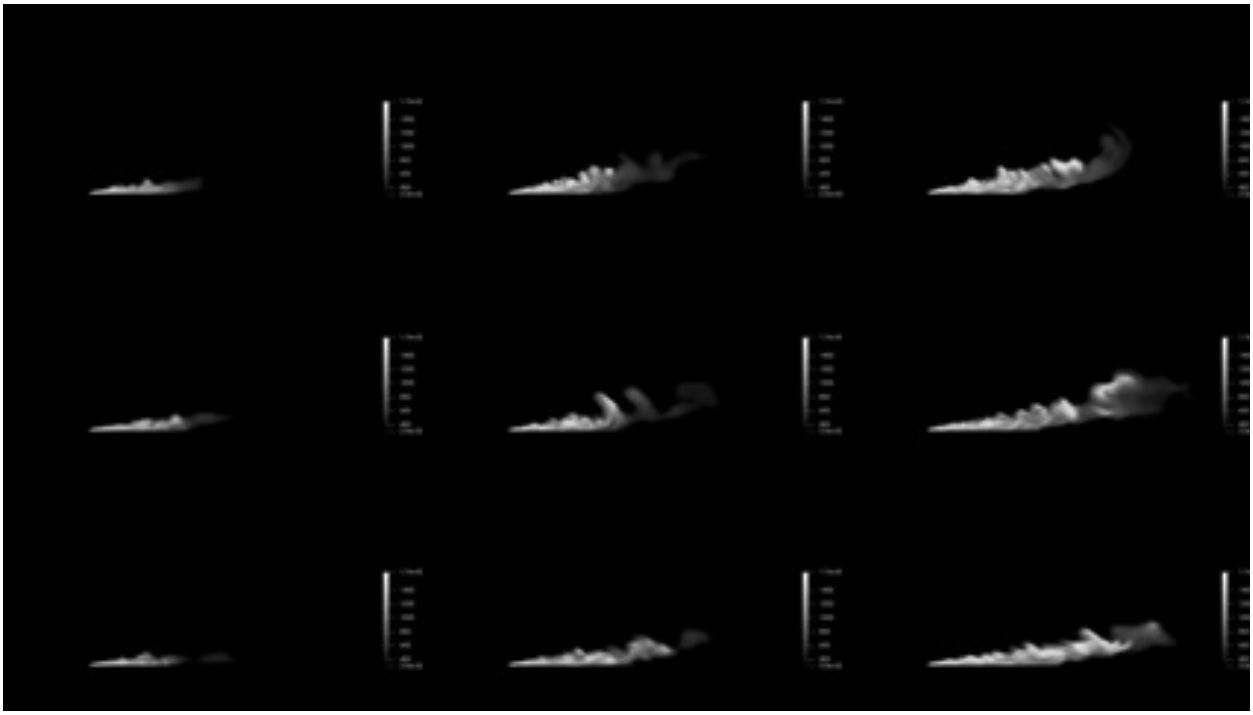

Figure 13: Instantaneous snapshots from simulations using $-10°$ (first row), $0°$ (second row), $+10°$ inclines, and 3 SLPM (first column), 6 SLPM (second column), and 9 SLPM (third column) methane inflow rates.

spectroscopy (LAS) measurements at 93 downstream and vertical locations. The simulations used measured inflow velocity profiles from the experiments (see Section 7.3) and used a 500 K isothermal temperature boundary condition on the bottom plate based on the measurements. As can be seen in Figure 14, we observe good agreement between simulation and experimental temperature field statistics in the baseline case using 240 rpm inlet blower speed, $0°$ tunnel tilt, and 6 SLPM methane inflow rate.

Various efforts are currently underway to gain even closer temperature field agreement. These include a more realistic description of both the tunnel inlet and burner velocity profiles that includes the effects of turbulence on larger scale mixing phenomena. A parameter study of EDM model coefficients will further lead to a more accurate description of ignition delay and reaction rates. We are also examining the effects of different wall models on the results; because the flame is within the boundary layer in these simulations, the choice of wall model is likely to be particularly significant.

Ultimately, closer model agreement in the baseline case will facilitate a wide-ranging exploration of temperature field and velocity statistics for many different flow and incline configurations. This will provide a rich and invaluable data set to the wildfire community. Current efforts to model pyrolysis and char in the WindCline are also currently underway. Similar comparisons will be made in these cases and will be extended to include char development and emission characterization.

5.4 Adaptive Mesh Simulations of Propagating Flames

Given the potential hazard and cost of experimental studies, particularly at large spatial scales, computational simulations are an attractive approach to studying fire behavior. However, computationally efficient, full-physics simulations that avoid empirical *ad hoc* models (Hanson, *et*

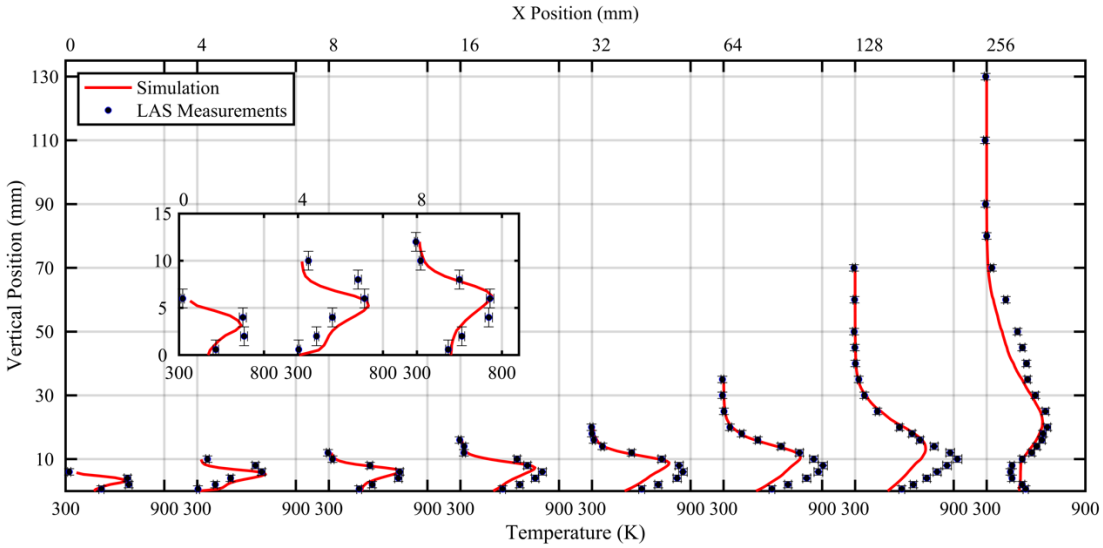

Figure 14: Path and time-averaged gas phase temperature statistics from simulation and LAS measurements using the baseline case with 240 rpm blower speed, 0° tunnel tilt, and 6 SLPM methane inflow rate.

al., 2000) are required to study fire dynamics over widely varying and realistic conditions, as well as to enable the reliable use of "outer-loop" techniques such as optimization (e.g., for mitigation and suppression efforts) and uncertainty quantification (e.g., for risk assessment).

Perhaps the greatest difficulty in performing such high-fidelity simulations is the wide spatiotemporal scale separation characteristic of fire spread problems. Disparate temporal scales, from relatively slow flow advection to fast chemical reactions, are often addressed by assuming infinitely fast chemistry. This mixed-is-burnt assumption can be made because chemical reactions occur on much shorter timescales than the turbulent mixing timescale for non-premixed flames. The eddy dissipation model (Chen, *et al.* 2014a, 2014b) can then be used to relate the combustion timescale to local turbulence timescales. Flamelet models or other mechanism reduction approaches (e.g., at run-time (Pope 1997, Singer, *et al.* 2006, Singer and Pope 2004) or *a priori* (Niemeyer, *et al*. 2010, Glusman, *et al.* 2019)) can also be used to balance fidelity with computational cost for problems where the mixed-is-burnt assumption is no longer valid.

Relevant spatial scales range from the small-scale structures of solid fuels to the larger scale features characteristic of buildings and warehouses. Methods to address temporal scale separation generally increase the minimum computational timestep, either by not resolving the reaction timescale or by making finite-rate chemistry more affordable. However, the minimum spatial length scale is often dictated by geometric constraints, such as the fuel size or local geometry. Although static mesh refinement can be used to address some of this scale separation, such approaches are inadequate in fire spread problems where the region of interest may be rapidly varying and is not known *a priori*.

In the present study, we use adaptive mesh refinement (AMR) to address the challenge of bridging wide spatial scale separations in simulations of fire spread. Using AMR, grid cells and physical resolution – and, by extension, computational resources – can be concentrated where they are most needed, for example to track a propagating flame. Previously, Lapointe *et al.* (2020) demonstrated the use of AMR with the OpenFOAM solver fireFoam for simulations of turbulent diffusion flames, and here we introduce a new extension of this solver, called fireDyMFoam, that uses AMR to model fire spread over solid pyrolyzing surfaces. The new solver retains the pre-

existing fireFoam capability for modeling multiphase flows, enabling the analysis and optimization of liquid-based fire suppression strategies (e.g., involving liquid films and particles) using computationally efficient AMR-based simulations of fire spread.

In the following, we outline the details of fireDyMFoam, including the treatment of gas, solid, and liquid phases, and a description of the AMR approach. We then demonstrate the solver for meter-scale vertical fire spread on combustible panels. We show that the solver reproduces results from static mesh simulations with the same fine-scale resolution, but at a substantially reduced computational cost. We then leverage these computational savings and use fireDyMFoam inside an optimization loop, driven by the Dakota toolkit for optimization and uncertainty quantification (Adams, *et al.* 2009), to minimize fire spread on a combustible panel, like previous test cases examined using the Fire Dynamics Simulator (McGratten et al., 2013; Lee 2019; Wang, *et al.* 2016). The new solver also includes dynamic load balancing for efficient AMR of fire spread problems. We have made the solver freely available to the fire modeling community at the public GitHub repository https://github.com/clapointe2011/public for simulations and optimization of a broad range of fire spread problems.

5.4.1 Computational framework: fireDyMFoam

Here we extend the AMR solver for diffusion flames outlined previously (Lapointe *et al.* 2020) to address multiphase flows and solid fuel pyrolysis. The new solver also includes dynamic load balancing to further increase computational efficiency. Each of these developments, which are described in more detail in the following sections, enable the simulations of landscape-scale fire spread described in Section 8.

5.4.1a Physical treatment of the gas phase

The fireFoam solver is typically used to perform LES, and this is also the approach that we take with the AMR-enabled solver fireDyMfoam. In the gas phase, 3D Favre-filtered compressible Navier-Stokes equations and conservation equations for mass, total enthalpy, and species are solved on a single unstructured computational mesh, where unity Lewis and turbulent Prandtl numbers are assumed.

Depending on the choice of turbulence closure, sub-grid scale (SGS) transport equations may also be necessary to close the governing equations. As in the standard version of fireFoam, we use mixture-averaged density and transport properties; the former is computed using the ideal gas law and the latter are temperature-dependent and computed using empirical correlations. Combustion modeling is assumed to be infinitely fast (for non-premixed flames) and governed by an eddy dissipation model. Radiation modeling is accomplished using a finite volume implementation of the discrete ordinate method, with a prescribed radiative fraction. For a detailed description of the gas phase physical treatment in fireFoam, we refer the interested reader to Wang, *et al. (*2011).

4.4.1b Physical treatment of the solid phase

We adopt the modeling procedure outlined previously for gas-phase modeling. In the solid phase, one-dimensional (1D) conservation equations are solved for mass, enthalpy, and species (Fukumoto, *et al.* 2018; Chaos, *et al.* 2011; Vinayak 2017). Solid-phase energy source terms include an optional in-depth radiative source, a reaction source term, a source term to account for mass loss (or, equivalently, gas production) from the solid phase, and an optional enthalpy flux-based source term for gas motion within the solid. These equations are solved on a series of independent, 1D solid meshes using mixture-averaged properties. That is, gas flux from the solid

is computed from the solid mass loss rate and is assumed to immediately enter the gaseous region (or equivalently from pyrolysate production rate) (Fukumoto, *et al.* 2018; Chaos, *et al.* 2011; Vinayak 2017). Additional details of the solid phase modeling are available in Fukumoto, *et al.* (2018), Chaos, *et al.* (2011), and Vinayak (2017).

5.4.1c Physical treatment of liquid films and particles

Liquid regions may be introduced at gas-solid interfaces and are commonly used to "collect" water droplets for suppression modeling. If used, quasi-3D equations for mass, momentum, and energy conservation are solved in the liquid phase (Meredith, *et al.* 2013; Ren, *et al.* 2017; Meredith, *et al.* 2011a; Meredith, *et al.* 2011b). For the film, a detailed description of all potential source terms is available in Meredith *et al.* (2013), and a summary of film modeling as it is commonly used is available in Ren *et al.* (2017). The equations are solved on a two-dimensional (2D) mesh and the third direction is captured implicitly by the film thickness.

If sprinklers are used (e.g., for flame suppression), a modeling methodology like other fireFoam sprinkler-suppression studies (e.g., FMGlobal 2017 and Ren*, et al*. (2017)) is adopted such that particles are only included as a mode of water delivery; heat transfer and phase change are not considered until the particles have been transferred to the solid panel surface (and incorporated into the film region). The particles are therefore governed only by a momentum conservation equation (because particle mass, composition, and temperature remain constant). Fluid-particle coupling is two-way, and particle source terms are treated semi-implicitly.

5.4.1d Phase coupling

Gas-solid-liquid coupling is treated in a segregated manner; particles are solved first, followed by solution of the liquid, solid, and gas phases (if a phase is not required, its solution is simply skipped). Interaction between each phase takes the form of the source terms described previously. At phase boundaries, the phases are coupled via mapped boundary conditions for the velocity, temperature, and fuel. For velocity, the mass flux of pyrolyzate in the solid region is matched to a corresponding mass flux of fuel in the gaseous region using either a one-to-one mapping or an energetically equivalent mapping (e.g., as implemented in the FMGlobal repository). For temperature, heat transfer is coupled between the solid, liquid, and gaseous regions, and for the fuel, pyrolyzate in the solid region is converted to a known fuel in the gaseous region.

5.4.1e Adaptive mesh refinement (AMR)

We refer to Section 4.3.1 for a description of the AMR process, including verification and validation of the approach in a range of both non-reacting and reacting flow problems.

Previously, we extended the AMR library in Jasak and Gosman (2000a-c) to enable refinement and coarsening on an arbitrary number of fields (Lapointe, *et al.* 2020). These fields are scaled at run-time to range between 0 and 1 (although un-scaled fields may also be used); refinement bounds are therefore fractions of the maximum value (e.g., the top 99.9% of values at a given time, or lower and upper bounds of 0.001 and 1, respectively). Prior work also involved extensive testing of the AMR procedure, focusing on flux corrections for new cell faces to ensure mass conservation. These improvements have also been implemented in fireDyMFoam.

Before continuing, it is prudent to discuss the application of AMR, specifically, within the context of fireFoam simulations. As described previously, fireFoam solves 3D conservation equations only in the gas phase; solid and liquid phases are 1D and 2D, respectively. This is important for two reasons: (*i*) native AMR functionality is inherently 3D and (*ii*) phases are

coupled with mapped boundary conditions (with an implied one-to-one mapping) at their respective interfaces.

Regarding the first point, we note that most of the computational expense can be attributed to the solution of the gas phase. Additionally, the solid and liquid phases use customized versions of "standard" OpenFOAM meshes, making integration of native AMR functionality non-trivial. Various researchers (e.g., Rettenmaier *et al.* (2019), and https://www.cfd-online.com/Forums/openfoam-meshing/118870-2d-adaptive-mesh-refinement.html) have addressed this integration (e.g., by extending the AMR for use with meshes that are not 3D), which is beyond the scope of the current study.

Regarding the second point, extensions to support changing meshes at the interface would ideally be accompanied using 3D meshes in the solid and liquid phases. This extension would also incorporate arbitrary mesh interface (AMI) functionality at interfaces; both extensions will be the focus of future work. For the current work, we focus on the use of AMR in the gas phase and make accommodations to facilitate its addition to fireFoam, such as pre-refining phase interfaces (to match the target maximum level of refinement) and protecting the interfaces from further refinement.

Recognizing that this pre-refinement (as well as the AMR itself) may introduce load imbalances for parallel simulations, we have also implemented run-time load balancing to maintain a balanced distribution of computational load for AMR cases run in parallel. This implementation follows that of the hyStrath repository (hyStrath 2021), where processor imbalances are assessed at write-time and system calls are used to redistribute the computational mesh. This method is noteworthy because it allows for use of native OpenFOAM utilities (e.g., reconstructParMesh, reconstructPar, and decomposePar), but requires minimal code modification (mostly at the solver level) and is easily extendable to other solvers.

5.4.1f Numerical treatment

The gas-phase is treated identically to the diffusionFireFoam simulations discussed previously. For the solid phase, we again use second-order methods for spatial discretization and first-order Euler integration for temporal integration. First-order methods integration time is also used in the liquid phase, if present; spatially, divergence terms are also first order and diffusive terms are second order. A global timestep is computed from a user-specified maximum advective Courant number in the gaseous and film regions and maximum diffusion number in the solid region. Temporal sub-cycling is used (often with a lower, particle-specific Courant number) to march Lagrangian particles forward in time.

5.4.2 Verification: single panel vertical fire spread

For the present implementation of AMR in fireDyMFoam to be deemed successful, it must result in a reduction of simulation cost with little or no impact on accuracy, as compared to equivalently refined static mesh simulations. To this end, we first compare the cost and accuracy of AMR in fireDyMFoam against statically refined simulations of a vertical fire spread problem (without particles or films, for simplicity).

The present case is based on a tutorial included with the standard distribution of OpenFOAM, where a [0.3 × 0.6] m, 60 kW propane burner is placed in the center of a narrow, initially quiescent domain. The burner is bounded on two sides by [0.6 × 2.4 × 0.01] m combustible wood panels, composed of homogeneous mixtures of unburnt solid fuel and burnt charred product. The propane

burns infinitely fast as it mixes with ambient air, heating the wood. The wood pyrolyzes and combustible products are transferred to the gaseous region, where they burn and the flame spreads.

For this first demonstration of fireDyMFoam, we focus on a single panel for simplicity, as shown in Figure 15. Static mesh and AMR simulations, described in the following, are performed for this simpler case, and the results are compared to verify that the AMR simulation produces comparable results to the static mesh simulation, but at a lower computational cost.

5.4.2a Statically refined simulation

In the static mesh simulation, a base mesh measuring [0.8 × 4.2 × 1.2] m, centered on the propane burner, was created for the solution of the gaseous region with 20 cm resolution. Four nested, static regions of refinement were then created, including a finest refinement region with 1.25-cm resolution occupying a [0.4×2.5×0.8] m volume centered longitudinally on the burner. Figure 16 shows slices through the center of the resulting static mesh at $z = 0$, indicating the successive regions of static refinement in the $x - y$ plane.

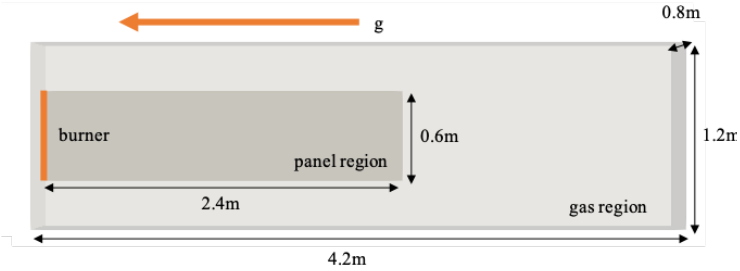

Figure 15: Schematic of the vertical fire spread case, showing the propane burner in orange, as well as both the panel and gas regions. The orange arrow indicates the direction of gravity.

The solid panel region was created by extruding a collection of faces on the boundary of the base mesh, within the 1.25 cm resolution region. An area of size [0.6 × 2.4] m was extruded by 1 cm, with 1 mm resolution in the third dimension. The propane burner was created in a [0.1 × 0.4] m area on the bottom boundary.

Gas and solid regions were coupled as described in the previous section. Within the gas phase, turbulence modeling was accomplished using a one equation eddy-viscosity model (Yoshizawa 1986) with C_k of 0.03. Combustion was modeled using the eddy dissipation method, as implemented in FMGlobal's fireFoam repository, with coefficients C_{EDC}, C_{Diff}, and C_{Stiff} of 4.0, 0.4, and 10^{-10}, respectively (Vilfayeau 2015 and Ren *et al.* 2016). Radiation modeling was performed using the finite volume discrete ordinate method with a prescribed radiative fraction of 0.2. In the solid phase, model coefficients for thermophysical properties match those from Chaos *et al.* (2011) for the single-layer configuration.

As mentioned previously, a custom variant of the PIMPLE algorithm is used; one outer PIMPLE iteration (where mass, momentum, and turbulence are solved) and three inner PISO iterations (where species and energy conservation and pressure correctors are solved) are used to solve the gas-phase conservation equations. A maximum convective Courant number of 0.5 is enforced in the gas phase, and a maximum diffusion number of 0.25 is used for the solid phase; the most limiting constraint is used to compute a single global timestep.

In total, the static mesh for the gaseous region was composed of 449,148 cells and the solid region was composed of 92,160 cells. We ran in parallel on 6 processors for 15 s of physical time.

5.4.2b AMR simulation

The physical setup of the AMR simulation is identical to that for the static case, described in the previous section. A base mesh of 20 cm is created, and the boundary faces along the gas-solid interface and burner are pre-refined by four levels to 1.25 cm resolution, for an initial cell count of

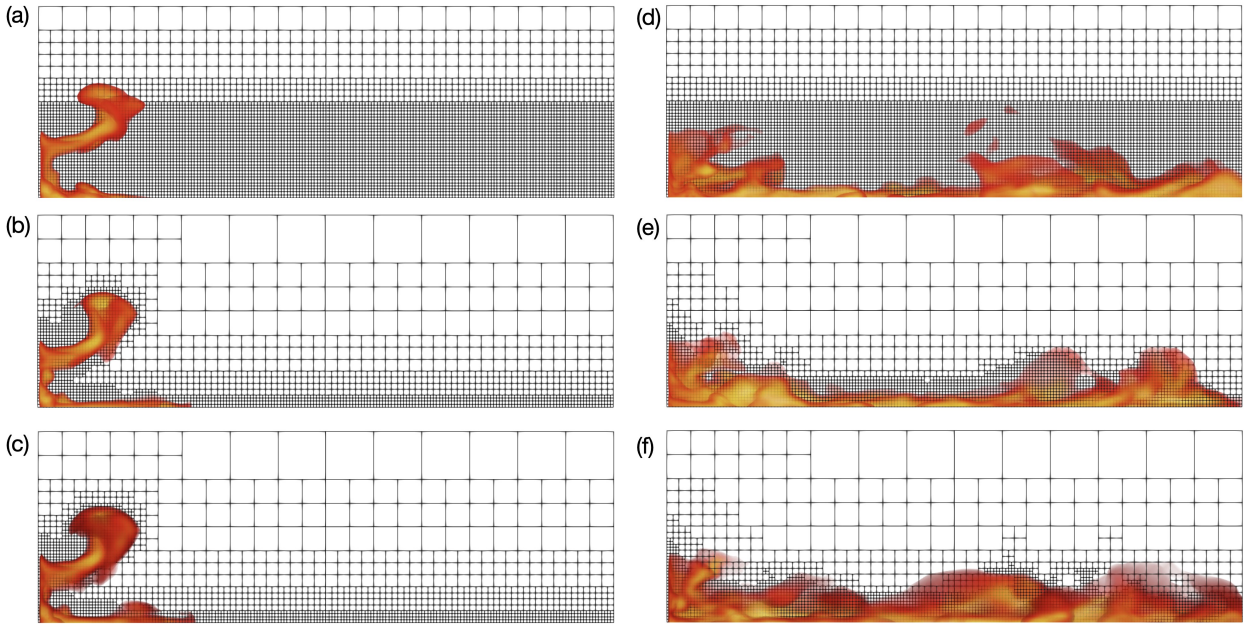

Figure 16: Visualization of static, AMR, and balanced AMR verification cases. Gas-phase combustion is visualized using volume renders of regions with high HRR for static (left sub-panels), for AMR without balancing (center sub-panels), and AMR with balancing (right sub-panels) vertical panel spread cases at times (a) 1.0 s, (b) 8.0 s. Regions are colored by temperature from low (black) to high (yellow). The computational meshes are visualized in a plane through the center of the domain in each panel.

69,048. The solid region is created as before and is therefore identical between the static mesh and AMR simulations.

Within the AMR simulation, four levels of refinement are used in the gaseous region to achieve 1.25 cm resolution, refining on gas-phase heat release rate (HRR) as a measure of combustion strength and location (top 99.9% of values) and gradients in HRR (top 99.9% of values) to fully encapsulate regions with combustion. The mesh is updated every four timesteps, and four buffer layers are used. Refinement fields are scaled at run-time to allow assignment of lower and upper refinement bounds more easily. It should be noted that other settings (e.g., fields and refinement criteria) may give even better results (i.e., further decrease computational cost without affecting simulation accuracy) and these values should be taken as illustrative rather than optimal.

Using the same physical setup and mesh update procedure, two AMR simulations were performed, corresponding to static and dynamic approaches to grid decomposition and allocation to computational cores. The first AMR case used a time-invariant, geometric decomposition of the gaseous domain, while the second case used run-time load redistribution with the "scotch" decomposition in OpenFOAM. In each case, the decomposition of the solid region did not change with time. For the case with load balancing, mesh redistribution was allowed every 0.1 s of simulation time.

5.4.2c Results and discussion

Instantaneous 3D renderings of the flame spread up the panel are shown in Figure 16 for the AMR and static simulations at 1.0, and 8.0 s. In general, the flame structure is qualitatively similar between the two simulations, with the propagation of the flame up the panel occurring at roughly the same rate in both cases.

The resulting AMR meshes at those times are also shown in Figure 16, illustrating the dynamically varying nature of the mesh and the gradually increasing number of grid cells in the AMR cases as the simulation proceeds. The AMR cases started with approximately 69,000 cells in the gaseous region and once spun up, fluctuated around 115,000 cells. The baseline and balanced variants required an average of 6.8 and 5.4 cpu-hours per physical second of simulation time (computed as the product of computation time and the number of cores divided by the physical duration of the simulation, 15 s), respectively. Consequently, we were able to decrease the computational cost relative to the static case which required an average of 13.6-cpu-hours per second of simulation time. Additionally, we have shown that, although the addition of load balancing makes the simulation even more computationally efficient, both AMR cases were significantly faster than their static counterpart.

From a quantitative perspective, the time history of volume integrated chemical HRR is compared for the static and AMR simulations in Figure 17. There is generally good agreement between the two simulations; it is emphasized, however, that the flame spread simulations are turbulent and some variability in the exact HRR time series is expected, independent of the mesh treatment. The overall shape of the time series is very similar between the three cases. We note that although the turbulent nature of these simulations is expected to create local and instantaneous differences in the simulation results, the general correspondence between the AMR and static simulations in Figure 17 suggests that the AMR simulation is adequately capturing the flame dynamics.

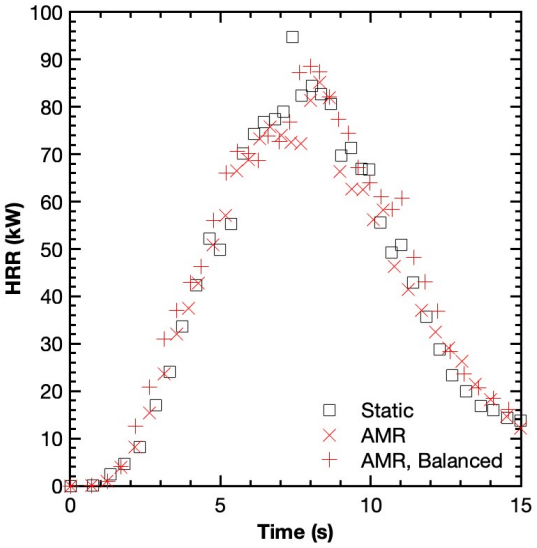

Figure 17: Comparison of chemical HRR time histories for static, dynamic, and dynamic with balancing cases. HRR is computed from instantaneous mass loss rates from the solid.

Finally, Figure 18 shows instantaneous temperature profiles from the AMR and static simulations at 8 s (when HRR is close to its maximum) near the gas-solid interface at various heights above the burner. Once again, the temperatures are similar between the two simulations, particularly near the centerline (i.e., x/L = 0), and deviations between the two sets of results are only observed near the edges of the flame. However, the turbulent nature of these simulations is again expected to create local and instantaneous differences in the simulation results, and the overall correspondence between the AMR and static simulations in Figure 18 suggests that the AMR simulations are capturing the flame dynamics reasonably well.

It is important to note that the computational savings of the AMR simulation are dependent on the choice of refinement fields and their bounds. We have shown here that the AMR simulation provides results that are comparable to the static mesh results, at a substantially lower computational cost. Additional improvements in efficiency may be achievable for other choices of refinement fields and AMR thresholds, although it should also be noted that further improvements in static mesh simulation cost may also be possible. As such, the present results should be taken as illustrative of the accuracy and efficiency of fireDyMFoam, and greater (or lesser) gains may be realized in other problems.

5.4.3 Validation: two-panel vertical fire spread

Building on the previous single panel vertical spread verification case, we now validate fireDyMFoam against experimental data for a panel spread case like the first verification case. A second panel with identical dimensions, opposite the first, was added to fully replicate the configuration in Chaos *et al.* (2011). For this configuration, two [0.6×2.4×0.0154] m corrugated cardboard panels are separated by a [0.3×0.6] m 60-kW propane burner. Experimental and computational data for chemical HRR and gas-solid interface temperature and heat flux were collected. Here we focus on HRR as a global metric of importance for combustion problems, and only perform an AMR simulation.

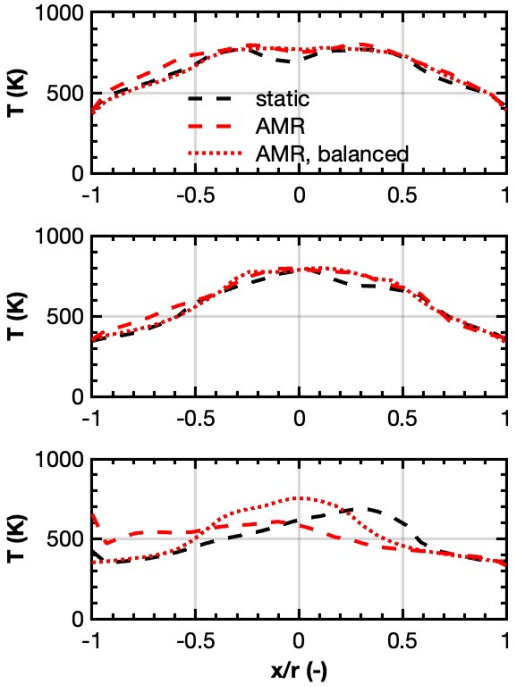

Figure 18: Instantaneous gas-phase temperature near the time of peak HRR near the gas-solid interface at 8 s. Panels from top to bottom show profiles at panel heights of z/H = 0.1, 0.5, and 0.9, where H = 2.4 m is the total height. The transverse location x is normalized by half panel width L = 0.3 m.

5.4.3a AMR simulation

The physical setup largely mimics the previous case shown in Figure 15 but now also includes a second solid region opposite the first. As with the single panel verification case, the mesh boundaries adjacent to the panels on the gas-solid interface are pre-refined, for an initial cell count of 14,712 cells, before meshing the solid region. The solid-phase computational domain is created as described previously, resulting in 4,608 independent, 1D regions, each 10 cells in depth, for a total of 46,080 cells. The case was run on a single processor for 150 s.

The physical models used in the gas phase are unchanged from the single panel spread verification case. Solid phase thermophysical properties are set following optimized values for the "triple-wall" corrugated cardboard reported in Chaos *et al.* (2011). The gas and solid phases are coupled as in the previous panel spread case with identical gas-solid interactions.

Following Chaos *et al.* (2011b), the gas-phase computational domain measures [0.3×8×3] m. Based on the recent success by Ren and Wang (2020) in simulating a similar case at coarse resolution, here we use a base resolution of 10 cm and two levels of refinement to achieve an effective resolution of 2.5 cm. The mesh was updated every other timestep; refinement fields and bounds were, however, not changed from those used in the single-panel verification case.

5.4.3b Results and discussion

Experimental (Chaos, *et al.* 2011b) and simulated chemical HRR (computed using the heat of combustion for pyrolysate from Ren *et al.* (2017) and Wang *et al.* (2014)) are compared in Figure 19. After spinup of the simulation, a maximum cell count of roughly 50,000 cells at peak HRR was required. Quantitatively, the AMR simulation provides a good prediction of the exponential increase in HRR (the primary goal of this simulation), matching computational results in Chaos *et al. (*2011) reasonably well. The value of peak HRR is also similar between the experiments and

simulations. We do note that the time of peak HRR in the simulation is slightly delayed relative to the experiment, and although a faster decay in HRR is also observed, a similar behavior has also been seen in other simulations, specifically those using statically refined meshes (Chaos *et al.* 2011). As such, the difference in the decay rates is likely due to the physical modeling used in the simulation (calibration is beyond the scope of this work), rather than due to the use of AMR itself.

In the future, this case could be improved, for example, by re-tuning solid phase thermophysical parameters for use with fireDyMFoam (and, by extension, a more recent version of OpenFOAM) to better match the experimental data after the time of peak heat release. In terms of modeling, possible improvements include the incorporation of a char oxidation model in the solid phase (e.g., as implemented in fireFoam) and recent developments in wall models for convective heat transfer (e.g., [44]) and updated solid phase thermophysical parameters (e.g., Ren and Wang 2020) and updated solid phase thermophysical parameters (e.g., Ren *et al.* 2017; Ren and Wang 2020). We anticipate that, given the results in Figure 19, each of these improvements will improve the agreement between the simulation and experimental results, and that AMR can still be used to decrease the computational cost of future simulations without negatively impacting accuracy.

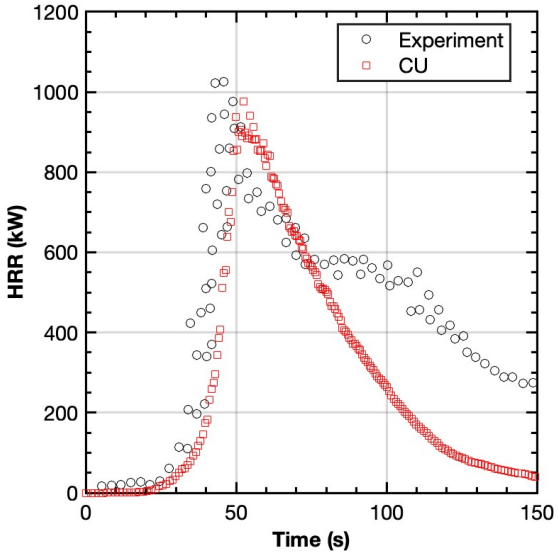

Figure 19: Time history of chemical heat release rate (HRR) for the two-panel fire spread verification case. Experimental results [43] are shown as black circles and AMR simulation results from fireDyMFoam are shown as red squares.

6. Results: Chemical Kinetic Model Reduction and Implementation

To reduce the computational cost of high-fidelity numerical simulations of wildland fire, computationally efficient—yet still physically accurate—reduced chemical kinetic models are required for the prediction of gas-phase combustion. Here we present three such skeletal models for the combustion of gas-phase products resulting from the pyrolysis of Douglas Fir. The computational savings enabled by these models are substantial when compared to detailed models, making the skeletal models suitable for wildland fire simulations spanning large ranges.

The need for such scale-resolving simulations arises from the considerable environmental and economic cost of wildland fires, as well as the difficulty in establishing future mitigation and avoidance strategies. It is anticipated that climate change will contribute to increased wildland fire activity, particularly in the Western U.S. (Barbero et al. 2015; Westerling 2016), further increasing the importance of simulations in fire management efforts. Predicting wildland fires using computational models remains, however, an inexact science.

As a possible solution to this challenge, high-resolution numerical simulations at much smaller scales (e.g., 10 m and below) can, in principle, be used to develop improved SGS models for landscape-scale wildland fire simulations. As the scale of the simulations decreases, however, there is a greater need to model all relevant small-scale chemical and fluid processes more accurately. To adequately model fire spread, simulations must be able to resolve small-scale turbulent mixing,

as well as capture the pyrolysis and subsequent gas-phase combustion of geometrically complex and spatially heterogeneous wildland fuels. The challenge of resolving turbulence can be addressed through advanced computational techniques such as AMR, but the chemical models must be sufficiently detailed without significantly increasing the computational cost.

Although typical biomass pyrolysis models are not excessively large, gas-phase combustion models routinely involve hundreds or even thousands of different species and reactions. For example, Ranzi et al. (2008) have provided a gas-phase biomass combustion model—which is the basis for the present skeletal models—that contains 4,533 reactions and 137 species. Skeletal and other reduced models are typically an order of magnitude smaller. The widely used multi-step DRM19 kinetic model, for instance, is a 19 species (plus N_2 and Ar), 84 reaction reduced model for methane combustion based on GRI-Mech 1.2 (Kazakov and Frenklach 1995).

6.1 Chemical kinetic model reduction (Glusman *et al.* 2019)

In the following, we outline the development of three new skeletal chemical kinetic models for gas-phase combustion of Douglas Fir pyrolysis products. The three models are targeted at large-scale simulations on high-performance computing resources but are intended to provide three different levels of accuracy and computational cost. Users may thus choose the model best suited to their needs and available computational resources. All skeletal mechanisms include a similar number of species (i.e., 71 and 54 species), but have vastly different numbers of reactions (i.e., 1, 179, 637, and 204 reactions).

The skeletal models are obtained by reducing the detailed chemical kinetic model for gas-phase biomass combustion from Ranzi et al. (2008). The reduction is performed using the directed relation graph with error propagation and sensitivity analysis method in a perfectly stirred reactor. We then show that all three skeletal models introduce relatively small errors, as compared to the detailed model, for various properties of premixed and diffusion flames.

6.1.1 Methodology

The overall reduction procedure tracks errors in ignition delay time and peak temperature in a constant-pressure, fixed volume perfectly stirred reactor (PSR) for the combustion of gases resulting from the pyrolysis of Douglas Fir. In the following, we describe the model and procedure used to obtain the Douglas Fir pyrolysis products, followed by descriptions of the detailed chemical kinetic model and the reduction process.

6.1.1a Pyrolysis model

The pyrolysis kinetic model is that of Debiagi et al. (2015), which includes extractives and is a refined version of the model published by Corbetta et al. (2014). The model involves 28 reactions and 47 species (including volatile, non-volatile, and condensed phase species) and provides pathways for the thermal decomposition of the three main polymer components of wood: cellulose, hemicellulose, and lignin, in addition to two extractives. It predicts light fractions directly, while heavy fractions are described by lumped species. The advantage of using this model is that the gaseous lumped product species correspond to those in an associated gas-phase detailed kinetic model (Ranzi et al., 2008), which is the starting point for the model reduction performed here. Of the 47 species in the pyrolysis mechanism, 18 are gaseous or volatile.

The major components of wood are polymers, and the pyrolysis model reflects this by starting with de-polymerization reactions, although in a highly simplified manner. Cellulose is assumed to transform into active cellulose, i.e., a reactive form that leads to the monomeric form and other

products like levoglucosan. Hemicellulose is assumed to decompose into intermediate species HCE1 and HCE2 that successively decompose with different activation energies, with different propensities to char. Lignin is assumed to be composed of LIG-C, LIG-O, and LIG-H (carbon, oxygen, and hydrogen rich derivatives of the β-O-4 molecule, respectively), that then decompose into intermediate components that lead to other products (Ranzi et al., 2008).

Extractives extend the applicable types of biomass that can be represented with this kinetic model. Previous versions of the pyrolysis mechanism (e.g., Corbetta et al., 2014) were only valid for specific types of biomass, depending on their carbon and hydrogen makeup. Extractives fall into two categories: hydrophilic and hydrophobic. Debiagi et al. (2015) chose to use a tannin (TANN) as the hydrophilic extractive and a triglyceride (TGL) as the hydrophobic extractive.

6.1.1b Douglas Fir Pyrolysis Products

To carry out reduction of the gas-phase kinetic model, a realistic set of gas-phase pyrolysis products is required as input to the gas-phase calculations. Therefore, we have run simulations using the pyrolysis model described in the previous section over a range of times and temperatures. This requires selecting a target wood species to work with, since the initial concentrations of cellulose, hemicellulose, and lignin vary by species. We have selected Douglas Fir because of its widespread availability and native presence in the Rocky Mountain region. We obtained the initial mole fractions of cellulose, hemicellulose, LIG-C, LIG-H, LIG-O, TANN, and TGL for Douglas Fir from Debiagi et al. (2015), Faravelli et al. (2010), and Schwetz and Lipp (1985).

The pyrolysis model is solved using an experimentally measured temperature time series as input. In the experiments, Douglas Fir samples were heated with a cone-calorimeter while simultaneously measuring surface temperature (via an infrared camera), gas temperature, and H_2O mole fraction. The latter two quantities were measured using dual-frequency comb laser diagnostics (Schroeder et al., 2017). Since the model describes pyrolysis (i.e., decomposition at high temperature in the absence of air), an approximately stoichiometric amount of air was assumed for comparison with the experimental dataset. The formation of pyrolysis gases is modeled using the surface temperature measured by the infrared camera, prior to combustion.

This process is carried out for each targeted condition (e.g., pressure, temperature, equivalence ratio, initial reactants), resulting in a single skeletal model that consists of the union of species remaining over all conditions. This guarantees that the reduced model maintains error below the specified limit for autoignition and PSR results.

6.1.1c Detailed Combustion Model

The detailed gas-phase kinetic model bio1412 from the CRECK modeling group is used as the starting point for the reduced skeletal models. This model is publicly available at the website http://creckmodeling.chem.polimi.it, with verification data given by Ranzi et al. (2008). The model contains 4,533 reactions and 137 species and is built upon earlier work from the CRECK group (Ranzi et al., 2001). Although this model has been shown to give good agreement for the gas-phase combustion of solid fuel pyrolysis gases (Ranzi et al., 2008), it is generally too large for inclusion in already demanding simulations of wildland fire. Consequently, in the following we reduce this model to a size that is appropriate for high-fidelity numerical simulations.

6.1.1.d Reduction Methodology

The CRECK detailed gas-phase combustion model is reduced using the Model Automatic Reduction Software (MARS) package (Niemeyer et al., 2010; Niemeyer and Sung, 2011, 2014,

2015). The reduction employs the directed relation graph with error propagation (DRGEP) and sensitivity analysis (SA) methods, followed by reaction elimination, which Niemeyer and colleagues have shown to be effective for reducing various surrogate fuel models.

Briefly, the process begins by applying DRGEP, which determines the importance of each species to the production or consumption of chosen target species (e.g., fuel, oxidizer, important pollutants). Next, a "greedy" SA removes individual species one-by-one and evaluates the error induced; it removes the species that least affect error and repeats the process on the remaining species until reaching the specified error limit. The error limit is determined by comparing predictions of the full, detailed kinetic model via autoignition and PSR simulations across expected conditions (e.g., pressure, temperature, equivalence ratio, and initial reactants) with those of the skeletal model. Ignition delay time and points along the upper PSR temperature response curve are chosen as metrics for the reduction, consistent with typical target parameters for premixed combustion mechanisms. Then, the contributions of each remaining reaction are examined, with the goal of eliminating reactions that are unimportant to the overall progression of the kinetic model, while remaining below the specified error tolerance. The final resulting model is considered the skeletal model.

This process is carried out for each targeted condition (e.g., pressure, temperature, equivalence ratio, initial reactants), resulting in a single skeletal model that consists of the union of species remaining over all conditions. This guarantees that the reduced model maintains error below the specified limit for autoignition and PSR results. Further, targeted species cannot be removed, regardless of their impact on the overall kinetics.

6.1.2 Results

Figure 20 shows the reduction process via DRGEPSA for the number of species remaining in the kinetic model as a function of error limit. Applying DRGEP with a maximum error of 30% (in ignition delay time and peak temperature in a PSR) to the detailed kinetic model removed 75 species and any reaction containing them, leaving 62 species. At this point in the reduction, the error in ignition delay time between the detailed model and the reduced model was approximately 21%.

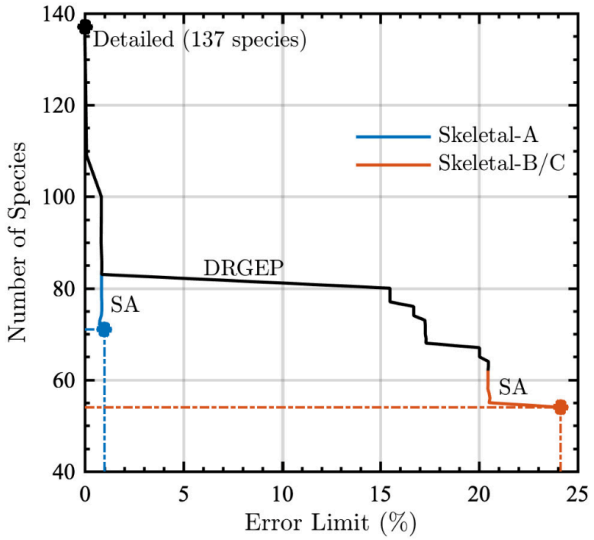

Figure 20: Number of species as a function of error limit during the reduction of the detailed model using the directed relation graph with error propagation (DRGEP) and sensitivity analysis (SA) method. Dash-dot lines indicate the number of species for the given error limit in skeletal models A (blue lines) and B (red lines) prior to the reaction elimination step (which produces Skeletal-C).

Applying sensitivity analysis removed 8 additional species and their associated reactions, resulting in a reduced model with 54 species and 637 reactions, giving approximately 24% error in ignition delay time, as compared to the detailed model. The reaction elimination step removed an additional 433 reactions, yielding a skeletal model with 204 reactions. For the ignition delay time in a PSR, this final skeletal model has 82.9% maximum error when compared to the detailed model. However, this most- reduced skeletal model

retains only 54 species and 204 reactions, corresponding to 39.4% of the total number of species and 4.5% of the total number of reactions in the detailed model.

During the DRGEP process, Figure 20 indicates a significant increase in error at 81 species, corresponding to a jump from 1% to greater than 15% error. Consequently, we created another reduced model with 1% error for gas-phase combustion, hereby noted Skeletal-A. Following the same naming convention, Skeletal-B is the reduced model produced by DRGEPSA with 30% error, and Skeletal-C is the model obtained from Skeletal- B after the reaction elimination step.

After the DRGEPSA process, the Skeletal-A model has only 1.00% error in ignition delay time compared to the detailed model, which increases to 24.1% error for Skeletal-B and 82.9% after the reaction elimination step in Skeletal-C. With the introduction of tabulated and dimensional reduction of chemistry, models on the order of one-thousand reactions and one-hundred species are suitable for computations (Hiremath et al., 2013), and thus all the skeletal models developed here are sufficiently compact for implementation in high-resolution simulations. The final skeletal models and associated information on thermodynamic and transport properties are provided as text-based files in the Supplemental Material.

To validate the model reduction in non-homogeneous flame configurations, laminar flame speeds were computed for a one-dimensional premixed flame in Cantera (Goodwin et al., 2018) using both detailed and skeletal chemical kinetic models with mixture-averaged diffusion coefficients. The physical domain length was 50 cm, the reactants were at a temperature of 300 K and pressure of 1 atm, and flame speeds were computed over a range of equivalence ratios. Figure 21 shows that there is essentially no discrepancy between the detailed and Skeletal-A models. Although errors are larger for the Skeletal-B and -C models, these errors will generally be tolerable in simulations of real-world fires given the typically larger errors introduced by other physical models in the simulations (e.g., for turbulence, heat transfer, and fuel properties), as well as uncertainties in boundary and initial conditions.

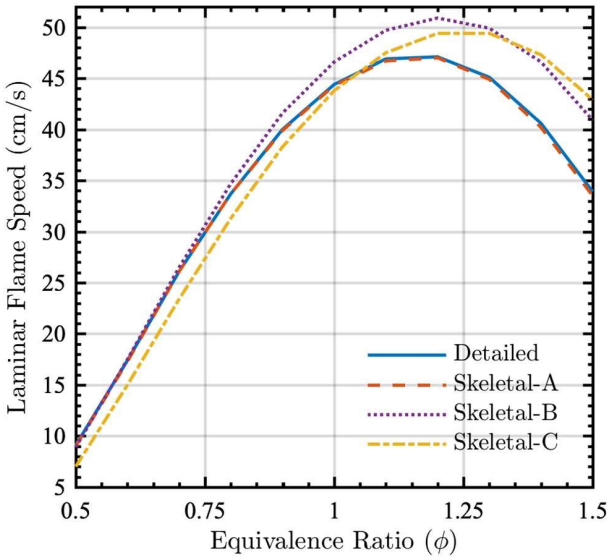

Figure 21: Laminar flame speed for a one-dimensional premixed flame as a function of equivalence ratio φ for detailed (solid lines), Skeletal-A (dashed lines), Skeletal-B (dotted lines), and Skeletal-C (dash-dot lines) models. The reactants were at 300 K and P = 1 atm.

Because wildland fires exhibit characteristics of both premixed and diffusion flames, the skeletal models were also used to compute the extinction temperature as a function of maximum strain rate for an opposed-jet diffusion flame. The simulations were performed using Cantera in an 18 mm domain with radiation. The fuel and air temperatures were 500 K and 300 K, respectively, and the pressure was 1 atm.

The results shown in Figure 22 indicate that the reduction process generally has minimal effect on the relation between the maximum temperature and strain rate at the extinction point. As with other metrics for the PSR and the premixed flame, the Skeletal-A model is in nearly perfect

agreement with the detailed model, and the Skeletal-B and -C models display relatively small discrepancies when compared to the detailed model.

Ultimately, three new skeletal chemical kinetic models have been developed and validated for the combustion of gas-phase products resulting from the pyrolysis of Douglas Fir. The skeletal models were obtained by using the directed relation graph with error propagation method, "greedy" sensitivity analysis, and unimportant reaction elimination to reduce a detailed gas-phase model with 137 species and 4,533 reactions.

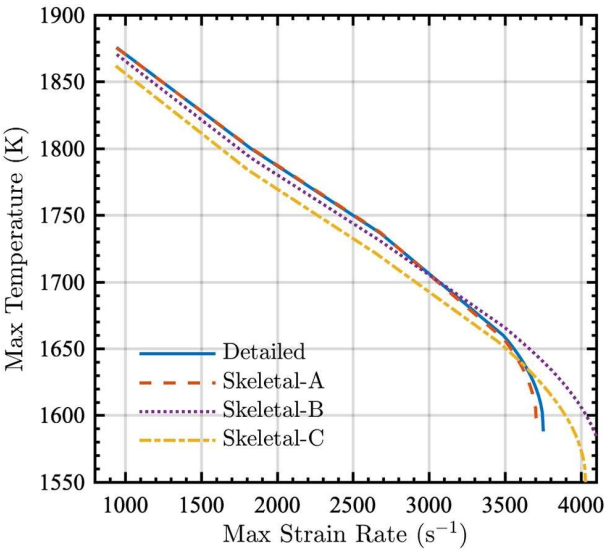

Figure 22: Maximum temperature in an opposed-jet diffusion flame as a function of maximum strain rate for detailed (solid lines), Skeletal-A (dashed lines), Skeletal-B (dotted lines), and Skeletal-C (dash-dot lines) models. The conditions of the opposed-jet configuration were T_{fuel} = 500 K, T_{air} = 300K, and P=1atm.

The three skeletal models had different sizes and resultant errors. The larger 71 species, 1,179 reaction skeletal model had a maximum error of 1% for combustion properties of interest over a wide range of conditions, while a more reduced model with 54 species and 637 reactions yielded maximum errors of roughly 21% and 24% in ignition delay time and laminar flame speed, respectively. The smallest 54 species, 204 reaction model had a maximum error of roughly 83% in ignition delay, with an average maximum error of 24%. These errors are reasonable given the complexity and uncertainty involved in modeling solid biomass combustion, although the larger skeletal model, with smaller error, is preferable if sufficient computational resources are available to allow its integration within high-fidelity simulations of wildland fire. It should also be noted that the largest errors were observed for all three skeletal models in the prediction of the ignition delay time, but these errors were small in absolute terms, particularly when compared to characteristic flow mixing times.

6.2 Chemical Kinetic Model Implementation

Wildland fires are multi-physics problems involving multi-phase flow, solid fuel pyrolysis, chemical heat release, and heat transfer via both radiation and turbulence-mediated convection. Further complicating the problem, these physical processes depend on fuel type, fuel geometry, and topography, among many other factors, and span an enormous range of spatial and temporal scales, from millimeter-scale chemical processes to fire spread at landscape scales. Although numerical simulations provide a low-cost, low-risk approach to studying wildland fire, simulation accuracy is constrained by the challenge of representing physical processes spanning such widely disparate scales (Hanson, *et al.* 2000, NIST 2018). In the present study, we address this challenge by combining computationally efficient simulations with multi-species chemical modeling to accurately reproduce time-resolved experimental measurements of chemical composition, temperature, and mass loss for a radiatively heated Douglas fir fuel sample.

In the target experiments, we perform simultaneous *in situ* mass loss, heat flux, optical imaging, surface temperature, laser-based gas temperature, and water vapor concentration measurements for a fuel sample under a cone calorimeter. We specifically focus on the pyrolysis of dry Douglas fir,

and then the gas-phase ignition of pyrolysis products. The experiments have carefully controlled boundary conditions, thus providing ideal validation data for the simulations, and the diagnostic suite is non-intrusive. The surface temperature of the fuel sample is measured with a calibrated infrared imaging camera. Simultaneous gas-phase temperature and water vapor concentration measurements are taken with near-infrared frequency comb laser absorption spectroscopy (Schroeder, *et al.* 2017, Coddington, *et al.* 2016). These experiments thus combine both traditional and state-of-the-art quantitative diagnostics to provide rich time-resolved data for simulation validation.

The numerical simulations are performed in OpenFOAM using a new adaptive mesh extension of the multi-phase reacting flow solver fireFoam, which models complex fire phenomena Wang, *et al.* 2011, FM Global's fireFoam). Initially developed for simulations of pool fires (Wang, *et al.* 2011), fireFoam has been used to model industrial fire problems in several different contexts and configurations (Meredith, *et al.* 2013, Ren, *et al.* 2016, Vilfayeau, *et al.* 2015, Ding, *et al.* 2015, Fukumoto, *et al.* 2018). The extension of fireFoam used in the present study is called fireDyMFoam (Lapointe, *et al.* 2019, 2020, 2021), which incorporates AMR to enable computationally efficient, yet high-resolution, simulations of wildland fire. This solver has been described in more detail for large eddy simulations by Lapointe et al. (2019,2020,2021) and is used here to perform LES of solid fuel pyrolysis in the solid-phase directly coupled with the gas-phase.

In the following, we first describe the *in situ* multi-diagnostic experimental measurements of Douglas fir pyrolysis. We then outline the AMR simulation framework, including the procedure by which the gas-phase composition of pyrolysis products is specified above the solid fuel sample. Finally, we present results showing that this framework provides good agreement with the available experimental measurements.

6.2.1 Methods

6.2.1a Experimental measurements

The experimental configuration is described in Section 6 of this report and consists of a [120×40×20] mm oven dried (85°C) Douglas fir fuel sample placed on a load cell (for mass measurements) and positioned beneath a cone calorimeter. The cone calorimeter generated a 21.5 kW/m^2 heat flux at the center of the sample, with uniformity over the full sample within 16% of the heat flux measured at the center. A calibrated infrared camera (FLIR A655SC) was used to measure the surface temperature of the sample, while gas-phase temperature and species mole fractions were measured with near-infrared frequency comb laser absorption spectroscopy [3, 4].

This diverse suite of diagnostics provides simultaneous time-resolved measurements of surface temperature, mass loss, as well as line-of-sight gas-phase temperature and water mole fraction, 4 mm above the surface. Full details of the experimental setup and results can be found in the study of fuel moisture effects by Makowiecki et al. (2020).

Although these small-scale experiments do not represent the full complexity found in real-world wildland fires, they do allow for careful control of boundary conditions, as well as the ability to isolate variables of interest (e.g., heat flux and fuel moisture content). Thus, these experiments are ideal for studying the detailed physical and chemical processes in support of model development for use in larger simulations of fire spread and suppression.

6.2.1c Physical setup

The numerical simulations are performed using the fireDyMFoam fire described previously. Within the gaseous domain, we solve the 3D low-pass filtered compressible Navier-Stokes

equations in addition to conservation equations for mass, total enthalpy, and species. A one equation eddy-viscosity turbulence model is used with default coefficients (Yoshizawa 1986). We employ a finite-volume implementation of the discrete ordinate method to model radiative heat transfer, with a prescribed radiative fraction of 0.2 and 100 discrete angles.

The solid phase is treated as described previously. Pyrolysis in the solid region is modeled as a single-step, irreversible Arrhenius reaction, where the reactions only proceed after the critical temperature $T_{crit} = 300$ K is reached. Once produced, the pyrolysis gases permeate the solid region via diffusion towards the surface. The gases enter the gas-phase region by mapping from pyrolysis products to a mixture of gaseous fuel species at the gas-solid interface.

The experiments are modeled using gas and solid regions of 1 m^3 and [0.12×0.04×0.02] m, respectively. Although the simulation configuration is an idealization of the experimental configuration, the available experimental measurements were all taken at or near the surface of the Douglas fir sample, away from the cone-calorimeter, structural supports, and other diagnostic equipment. Thus, it is not necessary to model the full experimental geometry to obtain good agreement with the measurements.

The gaseous domain is initially filled with a quiescent mixture of air and water vapor to match the ambient experimental humidity. All sides of the gaseous region are open and allow entrainment, except for the base, which is either modeled as a solid wall or as coupled to the solid region. This coupling takes the form of boundary conditions for velocity (to conserve the mass flux of gas from the solid region to pyrolysate species in the gaseous region), temperature (to conserve energy across the gas-solid interface), and species (converting generic “gas" product in the solid region to known species in the gaseous region). Custom boundary conditions made to address this conversion are discussed in the next section.

In the solid region, physical properties are set to match those of the Douglas fir sample used in the experiment. Properties of the wood are assumed to be homogeneous, with density 524 kg/m^3, thermal conductivity 0.1285 W/(m·K), emissivities of 0.759 and 0.957 for raw and charred wood, respectively, and a temperature-varying specific heat (Parker 1989). To model the radiative heat source used in the experiment, a heat flux of 21.5 kW/m^2 was applied to the interface following the implementation in FM Global’s fireFoam. The specific heat of formation of Douglas fir is -4×10^5 kJ/kg.

6.2.1d Numerical approach

The computational domain is discretized at the coarsest level into a 3.3-cm uniform mesh, with vertical stretching in the top 30% of the domain. We then refine the [0.12 × 0.04] m section of the bottom boundary by two levels (i.e., four times finer in each coordinate direction) corresponding to the solid-gas interface. The resulting mesh is composed of roughly 24,000 cells. We extrude this refined section downwards by 0.02 m to create the computational mesh for the solid. This gives 56 one-dimensional regions, each with 30 cells, for 1,680 total cells in the solid.

Within the gaseous region, two levels of AMR are used to provide higher mesh resolutions in areas of low density (i.e., hot regions) and high enstrophy to attain sub-centimeter resolution in areas of active combustion. An example AMR mesh, including the corresponding temperature field, is shown in Figure 23. Although the mesh does not change substantially during the later stages of the simulation, the AMR effectively provides the minimal mesh required to maintain the target resolution, resulting in an efficient numerical approach that does not require *a priori* knowledge of the flow. Most of the simulation was run with roughly 36,000 cells.

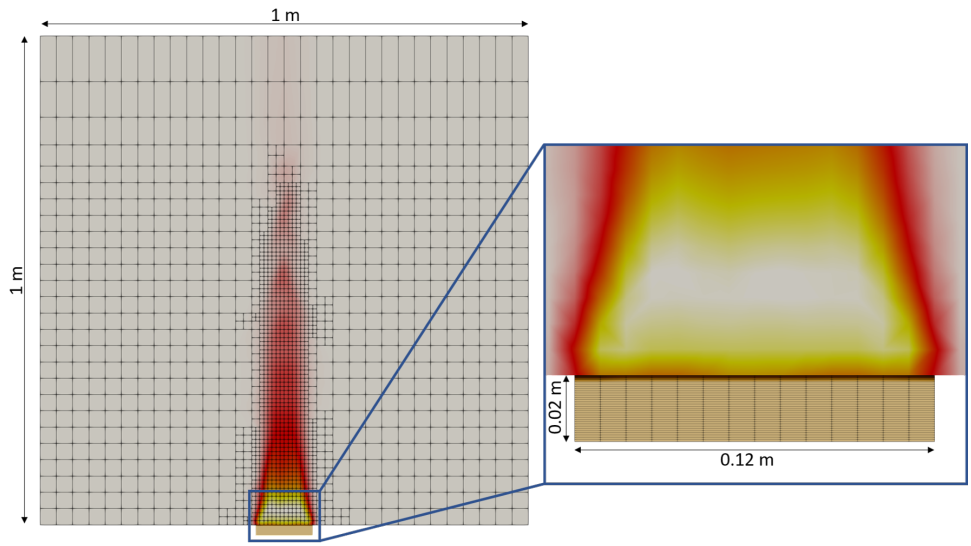

Figure 23: Gas- and solid-phase meshes, showing the temperature field from low (red, 750 K) to high (white, 1650 K) and the char in the solid (inset) from low (tan, 0) to high (brown, 0.03). Ambient temperature of 300 K is removed to show details of the plume.

In the gas domain, we use first-order Euler temporal integration and second-order spatial discretization. Total variation diminishing variants of the central differencing scheme are used for scalar divergence terms, stabilized central differencing is used for velocity divergence, and enthalpy gradients are limited to bound temperature. The solid region is numerically configured following cases from FM Global's fireFoam, resulting in first order in time and second order in space accuracy. Maximum advective Courant and solid diffusion numbers of 0.6 and 1, respectively, are used to set a global time step. A set number of 4 outer and 2 inner iterations are used.

6.2.2 Results

While calibrating the simulation parameters, we found that the physical properties of our samples had a large influence on the gas-phase results, as did the initial conditions. To that end, we took great care when carrying out experiments to completely dry the wood samples, accurately calculate the starting mass, and characterize the heat flux to the wood surface. Additionally, both AMR and statically refined simulations were performed to verify the AMR approach, and minimal differences were observed in the quantitative results. Consequently, only AMR results are shown.

Because data collected from the frequency combs are line-of-sight averaged, simulated values for gas-phase temperature and species must be similarly processed. Values are linearly interpolated onto horizontal profiles across the center of the block at 4 mm and 4±2 mm above the surface due to uncertainty in laser location attributable to swelling of the wood surface and beam steering (due to changes in the index of refraction) during the experiment.

The simulation utilizes CH_4 as the only gas produced in the process of mapping the gas in the solid to gaseous fuel in the gas-region and uses infinitely fast chemistry to simulate mixing-limited combustion.

6.2.2a Pyrolysis results

We observe good agreement between experimental and computational results for the solid surface temperature, as shown in Figure 24(a) for the simulated data. The surface temperature in the

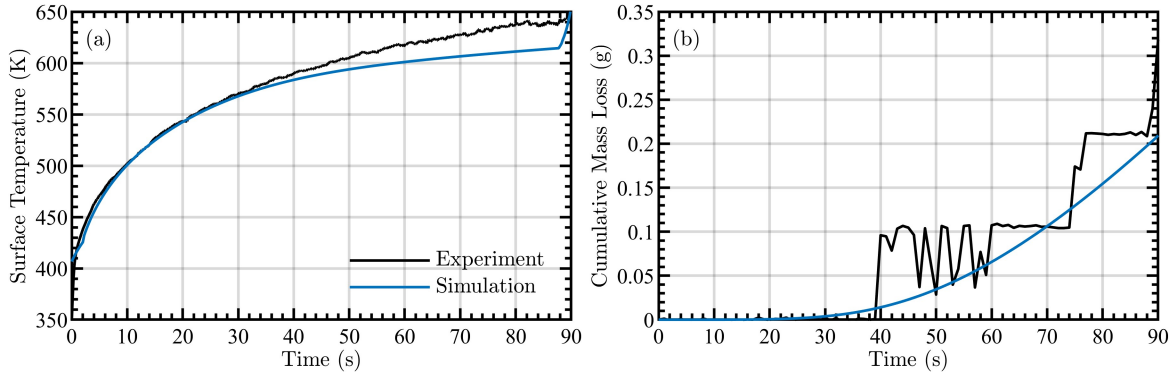

Figure 24: Surface temperature (a) and cumulative mass loss (b) during pyrolysis compared to experimental measurements nominally taken at 4 mm. The simulation contains only CH_4 and utilizes infinitely fast chemistry for combustion.

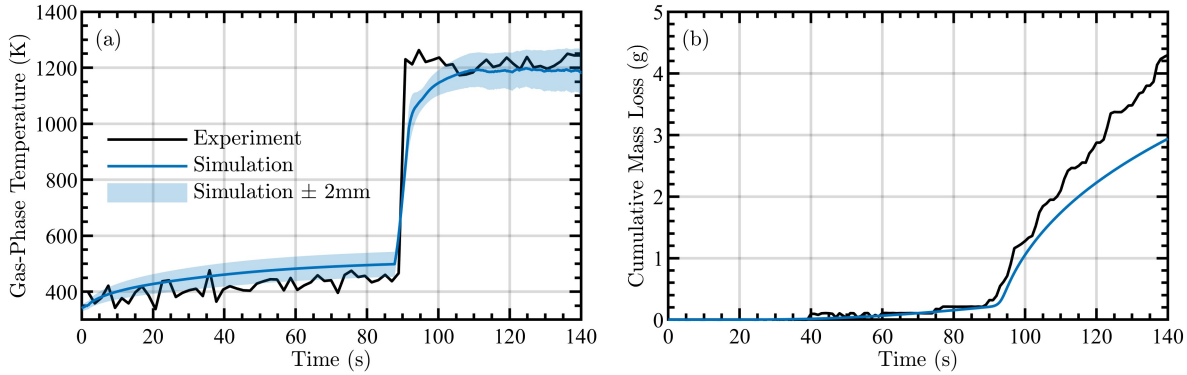

Figure 25: Gas-phase temperature (a) and cumulative mass loss (b) during pyrolysis and combustion compared to experimental measurements nominally taken at 4 mm. Clouds surrounding data provide measurements at ±2 mm from nominal measurement height. The simulation contains only CH_4 and utilizes infinitely fast chemistry for combustion.

simulation consistently heats up more slowly than the measurements at the end of the pyrolysis phase. Because the experimental surface temperatures were determined from the infrared camera using a constant surface emissivity, deviation between the simulation and experimental results occurs once charring begins (and the surface emissivity changes).

The simulated time-series of cumulative mass loss is similarly close to the measured values, as shown in Figure 24(b). Although the cumulative mass loss experimental data are binned in 11×10^{-2} g increments, the computational results match the overall trend. Specifically captured is the initial pyrolysis period where the wood heats without significant off-gassing, resulting in little to no mass loss.

The simulated time-series of gas-phase temperature, shown in Fig. 25(a), again captures the general trend of the experimental data. While sampling at the nominal height over-predicts the gas-phase temperature, it is expected that the wood sample surface would swell and deform as pyrolysis occurs.

6.2.2b Post-ignition results

At 89.5 s, combustion via infinitely fast chemistry is allowed to occur, matching the time when the experiment was ignited via a spark. Figure 25(a) shows that the simulation produces good agreement of gas-phase temperature after ignition. Figure 25(b) indicates that the cumulative mass loss is accurate for a short period before deviating slightly. Even in the absence of finite-rate

chemistry, it is possible to obtain good agreement with the gas-phase temperature and cumulative mass loss with the time-resolved experiments. Incorporating detailed pyrolysis chemistry is the focus of current work, described below, which is anticipated to improve the water mole-fraction comparison significantly.

6.2.2c Finite rate results

We have extended these simulations by simulating the ignition of pyrolysis products in the gaseous domain with finite-rate chemistry. Reduced chemical models based on previous work by the present authors (Glusman, *et al.* 2019) were used to identify reduced gas-phase combustion mechanisms for efficient simulations incorporating finite-rate chemistry. To utilize more complex chemistry, custom boundary conditions were developed to map pyrolysate in the solid phase to numerous reacting species in the gas phase.

With data obtained using mid-infrared frequency combs, additional species concentrations have been measured in a similar experimental setup, giving additional opportunities to showcase the predictive capabilities of this method (Makowiecki, *et al.* 2020). Moreover, coupling these computationally efficient simulations with parameter estimation methods such as approximate Bayesian computation (Christopher, *et al.* 2018), would allow the automated prediction of simulation parameters (i.e., heat of reaction and Arrhenius reaction coefficients) as well as initial conditions (i.e., temperature and water mole fraction).

Recent work has been focused on incorporating finite-rate chemistry to match experiments in which, *in situ* measurements of mass loss, surface temperature, gas-phase temperature and gaseous specie mole fractions are taken. Specifically, the Jones-Lindstedt reduced chemical model (Jones and Lindstedt 1988) and the previously described skeletal model are incorporated. These simulations will also incorporate AMR to decrease computational cost.

Additionally, to facilitate more complex, finite-rate chemistry models within a highly resolved simulation, integration of a load-balanced chemistry solver known as DLBFoam (Tekgul*, et al*. 2021) has the potential to allow an exponential speed-up over standard chemistry solvers. This work will combine cutting-edge numerical techniques in a singular framework to model the pyrolysis, ignition and combustion of a biomass specie validated by unique *in situ* measurements.

7. Results: Measurements of Biomass Combustion Using FCLD

In this project, dual comb spectroscopy (DCS), a type of FCLD, was selected over other diagnostic techniques for its rapid detection, coherent nature, and broad bandwidth. The coherent nature of DCS allows the beam to cover large distances, while the heterodyne detection removes the influence of thermal radiation from flames and hot surfaces. Traditional tunable diode laser-based spectroscopic techniques are limited by a narrow frequency range, which requires multiple lasers at carefully selected wavelengths to measure multiple species and temperature. The broad bandwidth of DCS can provide for the simultaneous measurement of several molecular species absorbing within its detection bandwidth because each gas exhibits a unique absorption fingerprint. The broad bandwidth detection of DCS also increases the dynamic temperature range which can be quantified as it can target absorption features with different temperature sensitives. Compared with other broad-bandwidth spectroscopic techniques, the DCS technique enables measurement in transient conditions. For the same resolution, DCS can scan 1000 times faster than FTIR systems.

7.1 Near Infrared DCS of Solid Fuel Pyrolysis and Combustion (Makowiecki et al., 2020)

We have implemented a unique suite of non-intrusive, quantitative diagnostics that simultaneously measure mass loss, surface temperature, in situ gas temperature and water vapor concentration, including the first implementation of dual FCLD for the study of solid fuels. As a demonstration, we examine the effect of fuel moisture content on the burning of Douglas fir wood samples that are ignited under constant radiative heat flux from a cone calorimeter to provide benchmark data for multi-scale models. A mass loss cone calorimeter from Fire Testing Technology Ltd., like the devices in Harada (2001) and Spearpoint and Quintiere (2001), uniformly heats the samples and measures mass loss. The heat flux distribution across the plane of the sample surface was characterized with a water-cooled heat flux meter provided by GBH International. By translating the heat flux meter across the plane corresponding to the sample surface, the heat flux is found to be uniform to within 16% of the maximum (which occurs at the center) along the 12-cm sample length. The mass loss calorimeter contains a load cell, shown in Figure 26. The load cell post extends through a clearance hole in the purge system box, where it is attached to the sample platform. The load cell was calibrated with a 250 g calibration mass before testing. Dessicated air flows into the purge system box which consists of an outer metal box of [12.5 x 6 x 2.75] in with a smaller box set of [5 x 4.5 x 2.5] in set into the center of the larger box, where the sample was placed on the load cell pedestal. The area between the boxes was covered with a fine wire mesh top through which the dried air permeated at approximately 0.03 m/s to purge the area around the sample. The box was filled with small beads to act as a manifold/diffuser to break up and distribute the entering flow. The slow flow can then be considered uniform and laminar with a calculated Reynolds number of 0.29 based on mesh dimensions, flow rates, and surface area. The dry air removes the background laser absorption signal associated with water vapor in the ambient air without perturbing the flow over the sample, as evidenced by a lack of measurable water vapor absorption in the spectrum above dry samples prior to heating.

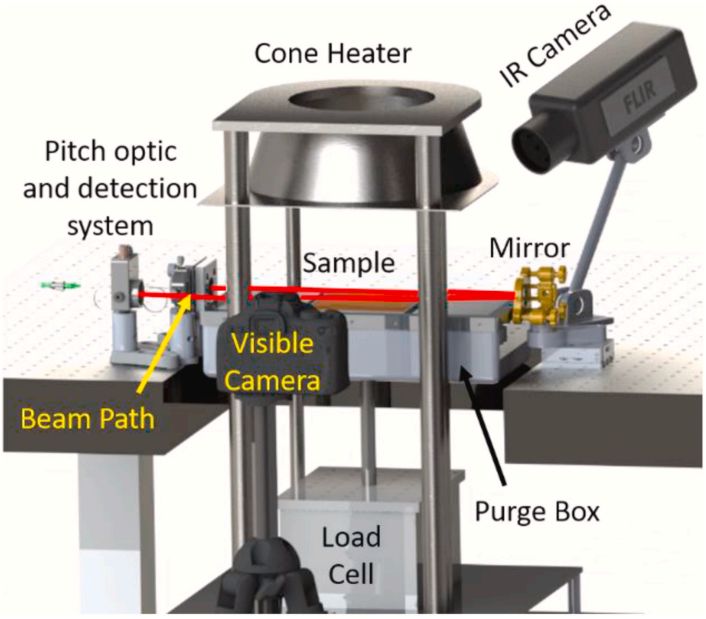

Figure 26: Experimental setup showing the configuration of the IR camera (surface temperature), laser beam path (gas-phase temperature and water vapor con- centration), load cell (mass loss), and visual camera (optical images). Not shown is the heat flux gauge. The cone heater uniformly irradiates the sample, while the purge box surrounding the sample holder provides a uniform flow of dry air to purge portions of the laser beam path that are not over the sample.

A spark igniter extends past the edge of the purge box and hovers approximately 10 mm above the center of the sample. A large voltage difference applied to the igniter produces a continuous ~5 Hz spark above the sample without locally heating the sample surface. To determine ignition time, ignition type, and flame dynamics, a Canon Rebel T6i DSLR camera records the sample

throughout the test at 30 frames per second. A FLIR A655SC infrared camera is used to monitor the surface temperature of the samples throughout each trial.

7.1.1 Dual frequency comb absorption measurements

Gas-phase temperature and water vapor mole fraction are measured using dual comb spectroscopy (Coddington et al. 2016). We have recently applied the dual comb spectrometer (DCS) for *in situ* species and temperature measurements in several turbulent environments, including stationary gas turbine exhaust systems (Schroeder et al., 2017), the open atmosphere (Coburn et al., 2018), a rapid compression machine (Draper et al., 2019) and industrial burner flames (Hayden et al., 2019). A similar technique, Fourier transform infrared spectroscopy (FTIR), has previously been used to measure emissions from biomass burning in laboratory scale fires (Yokelson et al., 1996, 1999), though well outside the flaming regions. To the author's knowledge, the current work is the first demonstration of non-intrusive temperature and water concentration measurements recorded within a biomass flame.

In the dual-comb technique, broadband light from two optical frequency comb lasers is passed above the sample (at a height of 3 mm and beam diameter of 2.5 mm in these experiments) and interfered on a fast photodetector. The light is absorbed at specific wavelengths that correspond to transitions of water vapor molecules between discrete rotational-vibrational energy states that are allowed by quantum mechanics. The absorption is quantified by heterodyne spectroscopy, where the measured signal is captured in a 'beat' rf signal created by interfering two optical frequency combs. This technique down converts the optical signals to rf frequencies that can be measured by the detector. The magnitude of the absorption, and the unique temperature dependence of the absorption for each transition can be modeled using transition-specific parameters from databases such as HITRAN and/or experimental validations. Water vapor mole fraction and gas temperature are extracted by performing non-linear least squares fit to minimize the residual between the measurement and the modeled absorption by varying the water mole fraction and temperature of the modeled absorption.

The systematic uncertainty introduced by the DCS instrument itself has been shown to be lower than 1% (Waxman et al., 2017). The dominant uncertainty associated with the measurement comes from the uncertainty of the absorption model used in the fit (Schroeder et al., 2017a) and non-uniform temperature gradients in the experiment. In this case, the absorption model is generated using experimentally validated line strengths, which describe the magnitude of an absorption feature, from Schroeder et al., (2018). The experimental line strengths are augmented by air-broadening and pressure shift parameters from the HITRAN2012 database (Rothman et al., 2013). Broadening parameters describe how the width of the absorption feature will change based on the concentration of gases present in the system and the pressure shift parameter describes how the center wavelength of a feature will vary with pressure.

Non-uniform temperatures were minimized by using dried air to purge all sections of the beam path laying outside the perimeter of the wood sample. The measurement is fundamentally absorption weighted, meaning areas with increased water concentrations, like flames, are weighted more heavily when fitting for temperature, this minimizes the contribution from background absorption during temperature fits, particularly during flaming combustion. We estimate the total systematic uncertainty due to model and instrument uncertainty to be less than 3% for the gas-phase temperature and water vapor mole fraction measurements. Due to the nature of diffusion flames, and in some cases the presence of multiple separate flaming regions, the temperature and water vapor distribution of the gases within biomass flames are non-uniform. Since absorption

measurements are inherently pathlength averaged the technique cannot capture a localized high temperature or concentration, but instead report an absorbance-weighted gas temperature and a pathlength-averaged mole fraction.

The dual frequency comb spectrometer used in this investigation spans approximately 1200–1800 nm with 200 MHz (0.0013 nm) measurement point spacing. A portion of the water vapor absorption bands near 1422 nm were used for this study. Spectra are recorded at 3.7 kHz and averaged to 2 s before each fit to improve the signal-to-noise ratio (SNR). A fit of each 2-s spectrum leads to time-resolved traces for water vapor concentration and gas-phase temperature. It is important to note that our measurements of flame temperature represent a laser-beam-path average temperature recorded approximately 3 mm above the surface of the wood sample. The peak gas temperatures reported in the following sections signify the highest path- average temperature recorded at a location 3 mm above the surface of the wood sample for each trial.

7.1.2 Sample preparation

Samples of Douglas fir are cut into approximately 120 x 40 x 20 mm pieces and lightly sanded with 220 grain sandpaper to ensure uniform finishes on each sample. All samples are placed in an 85°C oven for several days until the mass of the samples no longer decreases with time. At the end of the bake-out period, the mass of each sample is recorded as the dry mass. Two separate batches of samples were burned 3 weeks apart. Batch 1 consisted of 14 samples divided into three moisture content ‘groups. Batch 2 consisted of 28 samples divided into 5 moisture content ‘groups. All samples for a given moisture content group are soaked in distilled water for a set amount of time, then placed in airtight containers for approximately two weeks to allow the moisture to distribute evenly through the samples. During this time, the dry samples are stored in airtight containers with desiccant packets to prevent moisture re-absorption. All samples are weighed within 3 min of the experiment to determine the mass increase due to moisture absorption. Moisture content values are reported as the per- centage increase in mass from the dry mass.

After each sample is weighed, it is placed on the load cell with the grain orientated perpendicularly to the heat source, with the shutter system of the mass loss calorimeter (MLC) closed to prevent pre-heating of the sample. All diagnostics are started, and the MLC shutter is opened, exposing the sample to a heat flux of 21.9±1.7 kW/m^2. Within 10 s of opening the shutter the igniter pilot is switched on, creating a repetitive spark above the sample. After sustained flaming is achieved, the igniter is removed. The shutter of the mass loss calorimeter remains open during flaming combustion to allow smoke to be exhausted from the environment.

7.1.3 Experimental results

The results of simultaneous gas-phase temperature, surface temperature, water vapor mole fraction, mass loss, and mass flux measurements before and after sample ignition are shown in Figure 27 for representative samples with varying moisture content. The source of the water pro-duction pre-ignition is driven by two processes, evaporation, and pyrolysis. While it is difficult to decouple the production source of the water vapor, it can be assumed that the proportion of water vapor produced from evaporation is increased as initial fuel moisture content is increased. For each experiment with low moisture content, the mass flux, gas temperatures, and water vapor mole fractions are relatively constant before ignition of the sample. This indicates a consistent rate of production of water vapor from pyrolysis and evaporation is occurring prior to ignition. Only the highest moisture content case (Figure 27c) shows a different trend, where an elevated water vapor mole fraction is observed initially due to the presence of a water film on the surface of these

samples, which were kept in the water bath until just prior to the experiment to achieve maximum moisture content. Comparing across fuel moisture contents, the pre-ignition mole fraction of water and pre- ignition mass flux are lowest for dry samples (MC group A) and elevated for higher moisture content samples (MC groups B through F), as expected. It should be noted that all the samples were thermally thick, and even the driest sample contained enough moisture to sustain evaporation until the point of ignition. These trends in moisture evolution may not apply to thermally thin samples.

Sample ignition is marked by a steep increase in gas temperature that corresponds to the presence of large flames which cover the surface of the sample as the accumulated pyrolysis gases initially burn. Water vapor mole fraction, mass flux, and surface temperature also increase rapidly after ignition. The surface temperature of the sample remains elevated at a constant temperature following ignition, while the gas temperature only remains constant after ignition in the case of the driest sample (MC group A), where the gas temperature reaches and remains above 1200 K. For samples with moisture content above 20% (MC groups E and F), the gas temperature reaches a peak value above 1000 K just after ignition and then decreases, with the decrease more pronounced and rapid with increasing moisture content.

There is strong correlation between the water vapor mole fraction and mass flux time histories, as shown in the upper panels of each subplot in Figure 27. Both water vapor mole fraction and mass flux peak after ignition and then decrease simultaneously, in agreement with the water vapor trends shown in Refs. [20]. The peak mole fraction of water vapor after ignition is a relatively consistent 0.20–0.25 for all cases and decreases post ignition. For the highest moisture content samples (MC group F), the water vapor concentration decreases rapidly as the cooler flames provide a reduced heat flux to the burning sample, while for the dry samples (MC group A), the water vapor concentration decreases somewhat before maintaining a higher steady-state concentration compared with the samples of higher moisture content. This is consistent with the flame temperature and visual flame

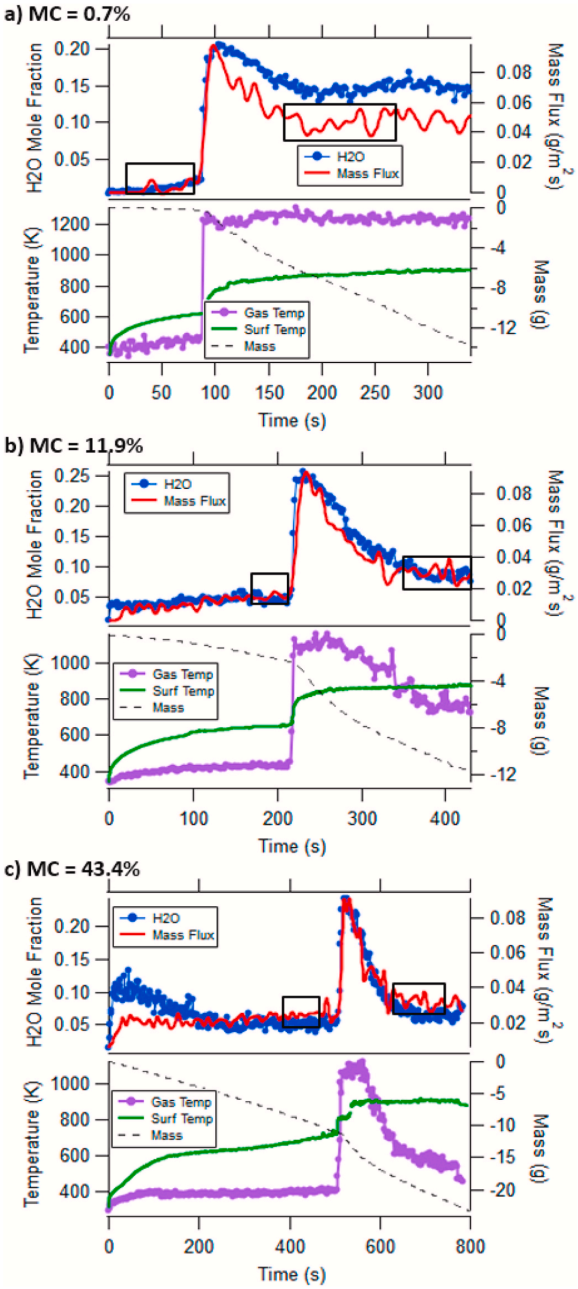

Figure 27: Representative plots of surface temperature, mass loss, mass flux, gaseous temperature and water mole fraction for three samples with varying moisture content: (a) 0.7% (b) 11.9% (c) 43.4%.

data, which show the flame weakening and developing more quickly into a patchwork of flame and surface smoldering for higher moisture content samples. The weaker combustion is accompanied by lower rates of mass loss. The lower rate of fuel consumption would be expected to produce less water vapor. To expand the application of these measurements, it would be useful to convert the measured mole fractions to species-specific mass fluxes from the surface. This would require an estimate of velocity and mixing at the surface of the wood sample, which could be accomplished through comparison to computational models or experimental measurements.

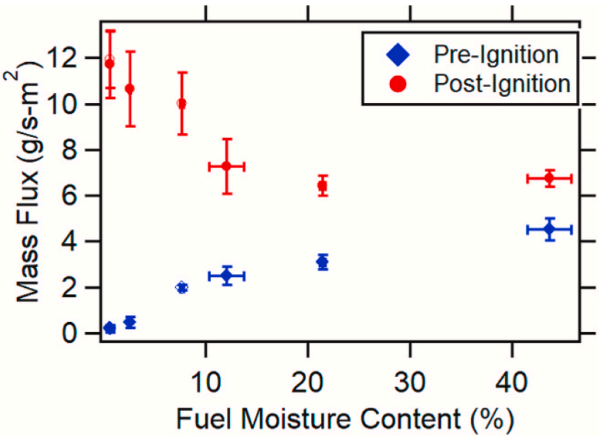

Figure 28: Mass flux before and after ignition as a function of sample moisture content. Mass fluxes represent the average of the time-resolved data encompassed by boxes in Figure 27.

The time-to-ignition increases as the moisture content of the sample increases, consistent with previous studies (McAllister, 2013; Atreya and Abu-zaid, 1991; Harada, 2001). This trend was consistent for each igniter configuration, but we do not quantify the ignition timing results because the ignition time depended on the igniter voltage source (and two different sources were used for the two batches of samples).

Figure 27 also provides insights into the combustion efficiencies for different samples. Between the time of ignition and the end of the experiments, each of the solid fuel samples lost roughly 10 g of mass. The time taken for this loss to occur increased with fuel moisture content, from roughly 200 s in the case of the 0.7% MC sample to roughly 300 s in the case of the 43.4% MC sample. This corresponds to a decrease in the combustion efficiency as the fuel moisture content increases. For each of the samples, the mass loss prior to combustion increased with MC, consistent with the expectation that there was increased evaporation for the samples with higher MC. However, the continued effect on the mass loss post-ignition indicates that evaporation was not complete prior to combustion.

Figure 28 shows the effect of moisture content on the measured mass flux pre- and post-ignition. The mass fluxes shown are determined from an average of the measured mass flux data prior to ignition and after ignition. An average was used due to the sensitivity of taking the derivative of discrete data with noise. Despite the different igniter configurations, there is good agreement between the two trials. As the moisture content of the fuel increases, the pre-ignition mass flux increases. Given the correlation between water vapor mole fraction and mass flux discussed above, this result is consistent with a higher rate of water vapor leaving the sample. Above a fuel moisture content of approximately 12%, the pre-ignition mass flux no longer increases proportionally to the fuel moisture content. This observation agrees well with Moghtaderi et al., who observed a similar trend during the combustion of Radiata pine, where the mass flux prior to ignition was relatively constant for samples at moisture contents greater than 10% (Moghtaderi et al., 1997). Future detailed modeling will aid in the interpretation, but this could suggest that the rate of moisture leaving the sample becomes diffusion limited.

Conversely, the post-ignition mass flux decreases with increasing fuel moisture content, indicating that wet fuel is consumed at a slower rate than dry fuel. While one would expect this

result, it is interesting that this trend plateaus for high fuel moisture content, so as the moisture content increases above 10–15%, there is no further reduction in post- ignition mass flux.

The peak flame temperature decreases with increasing fuel moisture content as shown in Figure 29. The peak temperature decreases from nearly 1300 K for dry fuel to ~1000 K for fuel with moisture content of 40%. For fuel moisture content below 20%, the decrease in temperature is proportional to moisture content with a slope that is found to be within 20% of another past study on pine (Anderson, 2020). As moisture content increases above 20%, the decrease in peak temperature is less significant. The higher pre-ignition water vapor concentration for fuels with more moisture content will serve to dilute the wood pyrolysis products and absorb energy during ignition and combustion. These results exhibit a similar temperature versus fuel moisture content trend reported for a Chemkin simulation of pyrolysis gases in an idealized opposing jet burner in Ferguson et al., (2013).

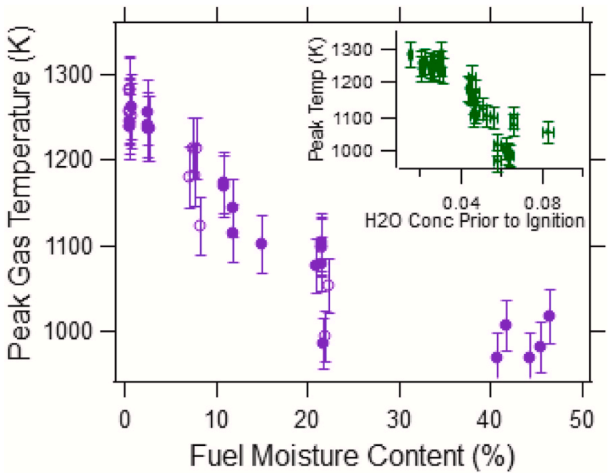

Figure 29: The effect of fuel moisture content on the peak gas temperature measured 3 mm above the sample surface. The inset shows the peak gas temperature data plotted as a function of the measured water vapor concentration in the gases above the sample just prior to ignition.

Ultimately, as moisture content in the sample rises, pre-ignition mass fluxes increase due to increased evaporation from the wet sample. The mass flux and water vapor concentration above the sample surface are observed to be highly correlated, which is expected prior to ignition if water evaporation dominates the mass flux. After ignition, this correlation is less easily interpreted since water vapor could appear both from evaporation and as a product of combustion. Additionally, post- ignition mass fluxes are smaller for samples with high water content, because the wet samples burn more slowly. However, both the increase in pre-ignition mass flux and the decrease in post-ignition mass flux appear to asymptote (toward similar values) as moisture content in- creases. These trends could be related to diffusion limits of water vapor through the wood and/or the energy balance of the sample.

Upon initial ignition, peak gas temperatures above 1000 K are observed for all samples, regardless of moisture content, at a height of 3 mm above the sample. Lower moisture content fuels exhibit the highest gas temperatures, more than 1200 K, and sustain these high temperatures after ignition. For moist samples, we observe a decrease in the peak gas temperature after ignition. This temperature decrease occurs more rapidly and is more pronounced for wetter samples, and correlates well with diminished mass flux and visual flame intensity.

7.2 Mid Infrared DCS of Solid Fuel Pyrolysis (Makowiecki et al., 2021)

Frequency comb spectroscopy in combustion environments was first implemented in the near-infrared (Lu et al., 2019; Alrahman et al., 2014; Schroeder et al., 2017; Draper et al., 2019; Hayden et al., 2019), where components to build the laser systems are robust and cost effective due to their development for the telecom industry. While near-IR systems enable sensitive detection over long pathlengths or at relatively high concentrations, many combustion-relevant molecules absorb weakly in the near-IR, limiting the practicality of the near-IR sources for detection in combustion

systems. In recent years, researchers have pushed to develop comb sources extending into the mid-IR to enable measurements of the fundamental vibrational transitions for many carbon-based species, where absorption can be 1000 times stronger than in the near-IR.

There are multiple approaches to generate mid- IR comb sources (Coddington et al., 2016), generally falling into two categories: nonlinear down-conversion of mode-locked combs (Schliesser et al., 2012) and direct, solid-state generation such as in quantum cascade lasers (QCL) (Faist et al., 2016) or inter-band cascade lasers (ICL) (Sterczewski et al., 2019). These semiconductor lasers emit light in the mid-IR or longwave-IR with a tooth spacing ranging from 5 to 50 GHz, and a bandwidth limited by the device dispersion to less than 100 cm^{-1} (Faist et al., 2016) (up to a few hundred comb teeth). The large comb mode spacing, and high power-per-mode make QCL-based DCS ideal as a diagnostic in high pressure and rapidly varying systems, as recently shown in Pinkowski et al. (2020). However, the coarse resolution can be insufficient to measure small, narrowly absorbing molecules without multiple inter- leaving measurements, and the smaller bandwidth can also limit the number of detectable species (Faist et al., 2016).

In contrast, mid-IR combs generated from a mode-locked near-IR comb via nonlinear processes such as difference-frequency generation (DFG) (Baumann et al., 2011; Ycas et al., 2018; Timmers et al., 2018; Nader et al., 2019; Herman et al., 2019) or optical parametric oscillators (OPO) (Adler et al., 2010; Kara et al., 2017; Sadiek et al., 2018; Muraviev et al., 2018; Abbas et al., 2019) can exhibit simultaneous bandwidth as high as 3700 cm^{-1} (Nader et al., 2019) with typical comb tooth spacing of 100-200 MHz (typically hundreds of thousands of comb teeth), but comparatively low power-per-mode. The source combs can be phase locked to each other allowing for better mutual coherence and long averaging times, which helps achieve high SNR.

Here we demonstrate for the first time, broad- band mid-infrared dual-comb spectroscopy utilizing mode-locked lasers for combustion analysis. We use a NIST high-power, fiber-based mid-IR comb (Ycas et al., 2018; Herman et al., 2019; Ycas et al., 2019) with 200 MHz comb tooth spacing covering a total optical bandwidth of 1500 cm^{-1} with two settings of the difference frequency generation process within the spectrometer. The broad band- width coupled with the fine resolution allows for instrument-lineshape-free measurements of both narrow and broadly absorbing species. By fully re- solving the spectrum, we can separate the over- lapping molecular signatures of both the narrow and broadly absorbing molecules and fit with absorbance models to extract quantitative concentration time histories and gas temperatures.

Biomass pyrolysis and combustion was selected as the ideal demonstration of the benefits of the mid-IR DCS system because it is an extremely complex process involving a variety of species. Understanding the evolution of species and temperature during biomass pyrolysis and combustion is vital to understanding the chemistry and ultimately predicting wildfire spread dynamics and emissions rates. This effort builds on previous work using Fourier transform infrared spectrometers (FTIRs) to quantify emissions from biomass burning in both laboratory (Yokelson et al., 1996, 1997; Bassilakis et al., 2001) and field-based studies (Yokelson et al., 1999; Scharko et al., 2019). By performing these measurements with a mid-IR DCS system in place of an FTIR, we can extract time-resolved measurements in the turbulent, high-temperature zone directly above the sample.

Here, we select the CO and CO_2 fundamental bands at 2000–2300 cm^{-1} to quantify emissions from smoldering combustion, and the C–H stretch region from 2500 to 3500 cm^{-1} to target emissions of pyrolysis species. In total, the DCS covers absorption from 11 target species: CH_4, H_2O, two isotopologues of CO_2, two isotopologues of CO, ethane, formaldehyde, methanol, acetic acid, and formic acid. The spectra from these species are highly overlapping and contain both broad and narrow features. Nevertheless, we show here that through 20-s coherent averaging, the

mid-IR DCS generates the high-SNR, ultrahigh-resolution, and broadband spectra needed to separate out these overlapping and congested molecular signatures. We can then fit with absorbance models to extract quantitative concentration time histories for each of the eleven species in addition to gas temperature.

7.2.2 Experimental system

The mid-IR dual frequency comb system is based on fiber optic, mode-locked lasers. The mid- IR light is generated through DFG of two near- IR fiber comb oscillators in a periodically poled lithium niobate (PPLN) crystal (Ycas et al., 2018). Each comb has a tooth spacing of 200 MHz (0.0067 cm^{-1}). The center wavelength of the output spectrum is tuned by changing poling periods of the PPLN crystal. Further details of the DCS system are explained in (Ycas et al., 2018, 2019). Spectra are collected at a rate of 104 Hz, phase corrected and averaged to 20-s time steps. While strongly absorbing species such as CO_2, CO, and H_2O could be measured with less than 20-s averaging, we chose this length of coherent averaging because it provides the SNR required for weakly absorbing species while still fully resolving the transient behavior of the wood pyrolysis process.

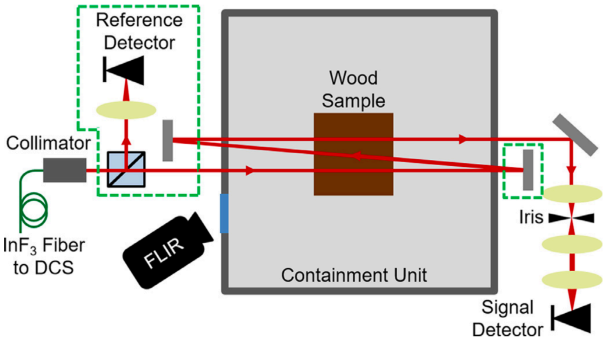

Figure 30: Top-down view of experimental setup. Components in green dashed boxes are only present for tests in the C–H stretch region.

The experimental setup is shown in Figure 30. Due to building constraints, it was not possible to locate the combustion system in the same room as the laser system. Therefore, the mid-IR comb light is coupled into a 20-m single mode InF_3 fiber for delivery to the experiment. The light is collimated with an off-axis parabolic mirror and passes over the radiatively heated sample. It is spatially filtered to reject radiation from the heater and focused onto a photodetector.

For the 4–5μm wavelength region, the CO and CO_2 absorption is sufficiently strong to enable detection with a single-pass configuration. For the second wavelength region from 3 to 4 μm, the absorption is weaker and a triple- pass configuration increases the interaction length and the corresponding absorption signal. As such, components in the green dashed boxes in Figure 30 are only present for tests in the C–H stretch region.

Because CO and CO_2 are narrow absorbers, the broadband intensity variations of the mid-IR combs can easily be separated from the molecule signatures in post-processing. However, the molecular signatures of the large, broadly absorbing molecules in the C–H stretch region are difficult to separate from the comb source intensity variations, so a second reference measurement is added to monitor the comb spectra in this region.

Biomass samples are 10 × 10 × 2.5 cm cuts of oak that have been dried in a convection oven at 75 °C for 25 days. Sample mass is monitored regularly and considered dry when the mass no longer decreases. The surface of each sample is lightly sanded with 110-grit sandpaper to ensure uniformity. During the experiment, the samples are radiatively heated at 22.4 kW/m^2 in a mass-loss calorimeter from GBH International (Makowiecki et al., 2020). The calorimeter consists of a cone-shaped resistive heater above a sample-holding pedestal. Initially, the radiation from the heater is blocked by a shutter, which is opened to begin testing. The mass-loss calorimeter is placed inside an aluminum containment chamber with a 15-cm duct and in-line fan to remove smoke from

the chamber. An infrared camera (FLIR A655SC) monitors the surface temperature of the wood samples.

To quantify species concentrations and gas temperature, we fit the measured transmission spectra with absorption models derived from the Pacific Northwest National Laboratory (PNNL), HITRAN and other experiments (Sharpe et al., 2002; Gordon et al., 2017; Johnson et al., 2010), using the m-FID technique described in Cole et al. (2019). Prior to each measurement, we record a 5-min transmission spectrum with the heater on, the shutter open, and the sample removed. This background trans- mission spectrum is then used to normalize the subsequent measured spectra. This normalization serves two purposes; first it removes background absorption from the open portions of the beam due to CO_2 and H_2O in the room air. Second, the normalization removes most of the intensity variation of the mid-IR comb sources across the spectrum. The spectral fitting for each region is described in more detail in Makowiecki et al. (2021).

7.2.3 Results and discussion

Figure 31 shows representative data for a 20-s period during the pyrolysis experiment. We fit each 20-s average spectrum throughout the 30-min experiment to yield time- resolved concentrations and gas temperature. The retrieved concentrations and gas temperature are plotted as a function of time in Figure 32. The traces follow distinct trends, governed by the progression of biomass thermal decomposition. The pyrolysis species, such as methanol, acetic acid, and formic acid, are a product of degradation of the wood at lower temperature and thus are emitted quickly after the shutter is opened. Emissions of these products continue throughout the test as deeper layers of the wood are heated and begin to pyrolyze.

At approximately 500-s, we see the onset of smoldering combustion as there is an increase in the emissions of the aliphatic compounds that are associated with smoldering combustion: CH_4 and C_2H_6 in addition to CO and CO_2. Interestingly, we also see significant emission of both CO and CO_2, but not CH_4 and C_2H_6, prior to the onset of smoldering combustion, which suggests that either the unstable species from the pyrolysis are decomposing to form CO and CO_2 or these species are directly produced from the pyrolysis. It is noteworthy that the isotopologue ratios of CO follow the natural abundance, while there is a splitting in the isotopologue ratio for CO_2during smoldering combustion. Isotopologues of C^{12} and C^{13} can indicate carbon fractionation pathways, seasonal trends, and CO_2 sources for the tree (Gessler et al., 2014). However, meaningful interpretation of the isotopic ratios requires extreme precision and accuracy to resolve minute differences between isotopologue concentrations. As such, we avoid drawing conclusions based on these early measurements, and future investigations into isotopic ratios using mid- IR DCS will require enhanced short-term SNR as well as improved spectral databases of these isotopologues, particularly for high temperatures.

Direct comparison to previous studies is not possible due to different fuel types and the fact that previous studies extractively sampled the gases or optically interrogated in the exhaust flume with much lower time resolution. However, relative concentrations reported here compare well with previous studies on biomass combustion. Yokelson et al. (1996) report emissions of CO, CO_2, CH_4, C_2H_6 and NH_3 from smoldering combustion in laboratory scale fires consistent with the findings here except NH_3, which was below the detectable limit in this study. In the same study, they report methanol, formaldehyde, acetic acid, and formic acid as detectable in pyrolysis products.

The difference between the gas and surface temperature is also consistent with expectations. The radiative heater primarily heats the wood surface, which then heats the gases above through

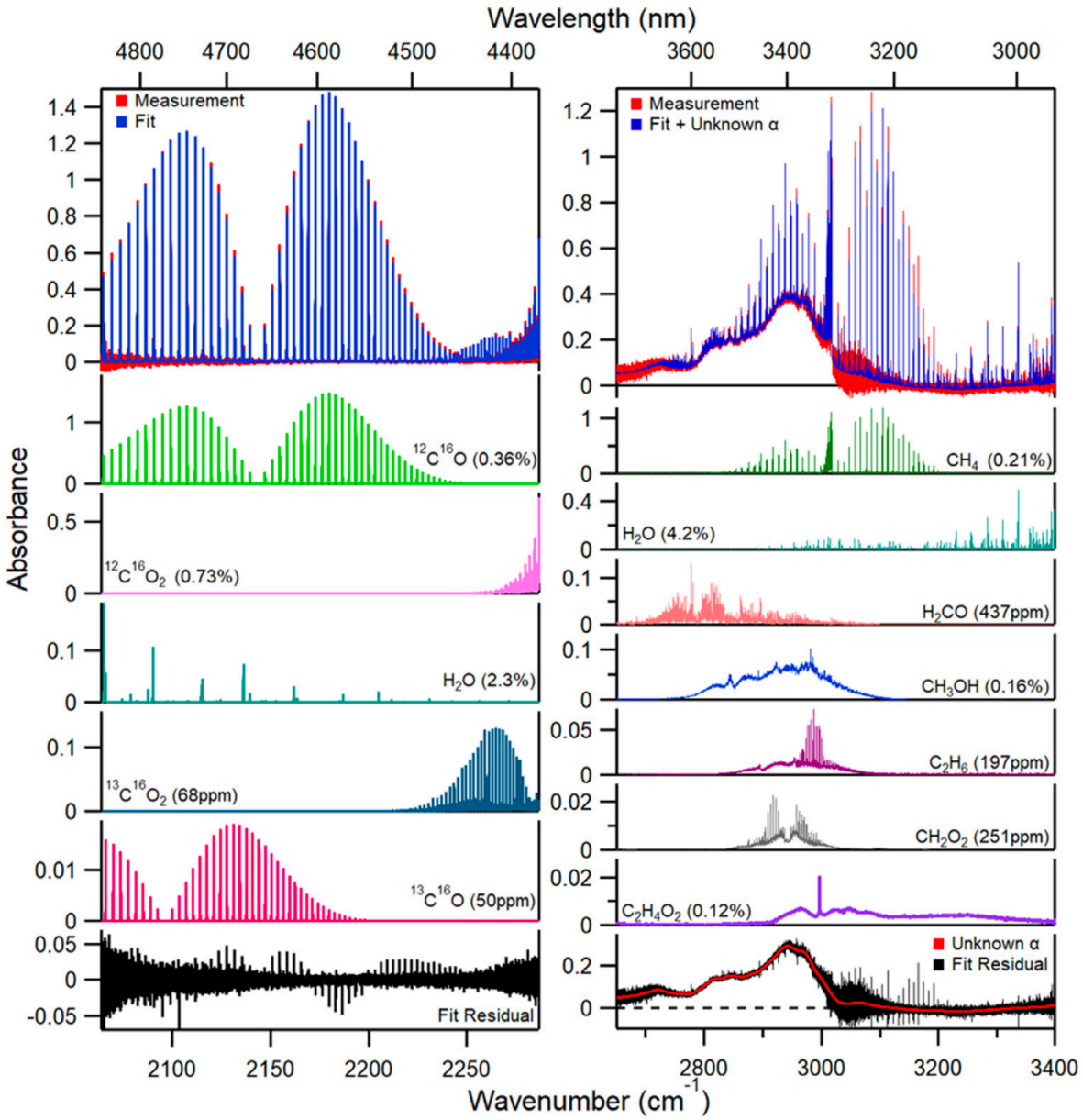

Figure 31: Recorded absorbance spectra and model fits to obtain species concentrations and temperature. The left panels show the measurement and fit in the 4-5 μm spectral region targeting CO and CO_2 transitions. The right panels show the measurement in the C–H stretch region. The top panels show measured DCS data (red) and the spectral fits (blue). The second row shows the fit residuals. The absorbance model of each constituent in the fit is shown separately below. For the C–H stretch region (right panels), the blue curve in the top panel is the addition of the spectral fit together with the residual absorbance from the m-FID approach.

convection. The poor thermal conductivity of air creates a strong thermal gradient above the sample, with the sample temperature being consistently higher than the gas temperature.

7.3 WindCline Measurements

In predicting wildland fire spread the impacts of weather and topography are of particular importance. For example, in mountainous landscapes we often see unexpected and rapid fire spread due to buoyancy effects on flame dynamics. Recent work has determined the flame

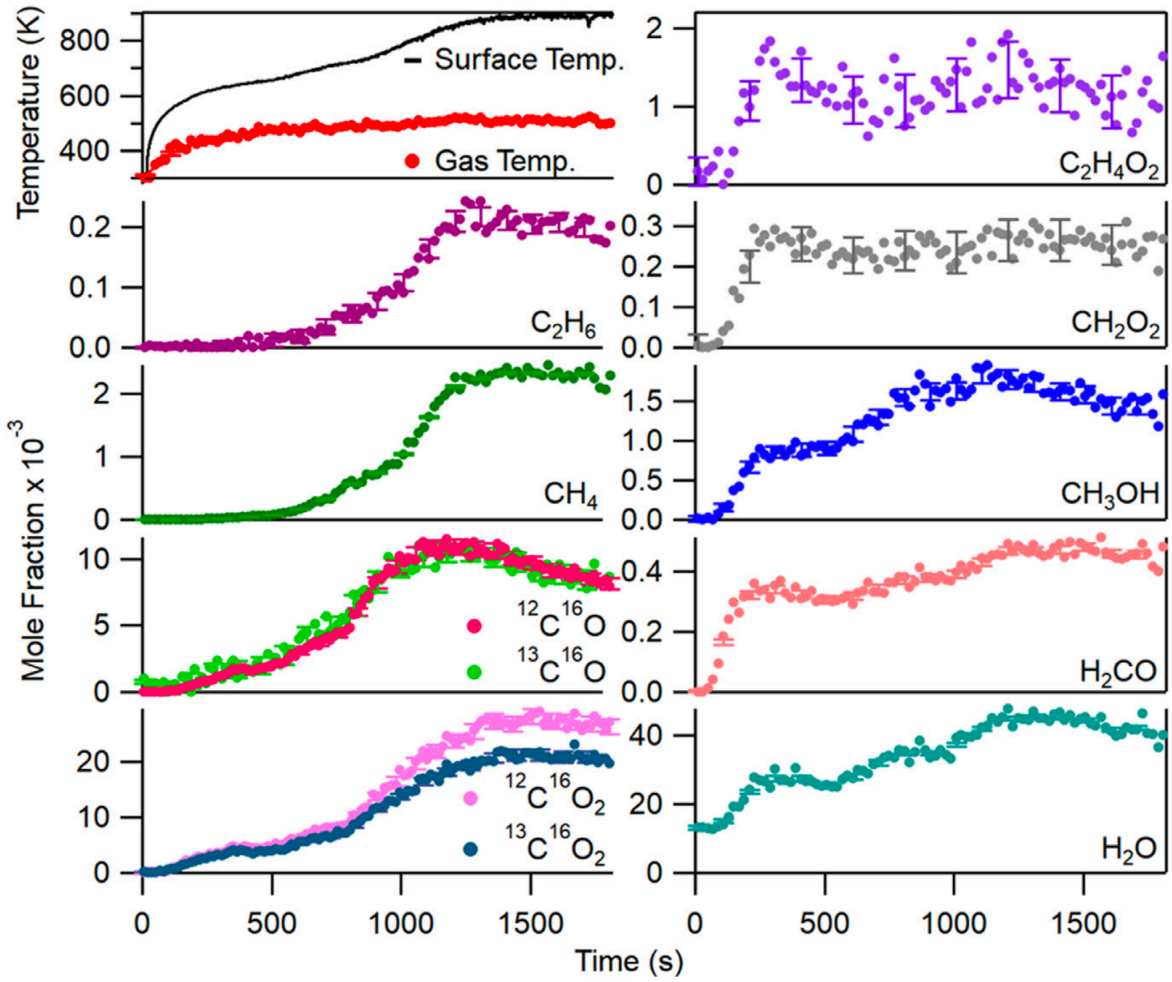

Figure 32: 20-s time-resolved species concentrations and gas temperature derived from the DCS measurements. Species concentrations are normalized by the natural abundance used in the HITRAN database. The species are grouped by the process which governs their production (and hence trend), with species predominantly produced from smoldering combustion on the left and species produced from pyrolysis on the right. Uncertainty bars are calculated from uncertainty in pressure measurement, statistical fit uncertainty, and saturation threshold (varied from 0.15 to 0.25).

structure and dynamics witnessed in both field and laboratory studies must be considered to accurately predict flame front propagation.

While several studies have been performed on tilting platforms in open rooms, the open room concept prevents isolation of boundary conditions, and airflow throughout the area can impact flow conditions, making boundary conditions difficult to quantify. Placing tilting platforms within wind tunnels can mitigate room airflow effects but will create non-uniform flow within the measurement volume. The platform acts as a constriction in the flow, creating a back pressure in the tunnel. As the flow is constricted into a smaller area by the tilting platform, it will accelerate, leading to non-uniform velocities across the platform surface, further complicating boundary conditions and making experimental results challenging to replicate computationally.

To mitigate these effects and overcome these challenges, we have designed and built a wind tunnel facility called the WindCline where the wind tunnel structure is mounted on a tilting

platform. The tilting platform allows for the investigation of incline effects on flame structure, without compromising flow quality.

7.3.1 Description of facility

The wind tunnel is a blow-down type wind tunnel where ambient air is pulled in through a blower and is pushed through the tunnel; Figure 33 shows a schematic of the tunnel. This design prevents hot exhaust gases from soiling or overheating the fan. After the blower, the air is expanded in a wide-angle diffuser, before entering the settling chamber. The settling chamber consists of 4-inch-thick, ¼ cell extruded aluminum honeycomb to straighten the incoming flow. After the honeycomb, there are two stainless steel M60 screens mounted 2 inches apart. The screens provide backpressure to the flow and break down turbulent structures which are larger than the mesh size of the screens. After leaving the settling chamber, the flow cross section is contracted down to the cross section of the test section. The test section cross section dimensions are 35cm x 35cm and the test section extends 100cm. The test section is built on an extruded aluminum frame to allow for reconfiguration if needed. The side panels are made from boroscillicate glass to allow for optical access and imaging and maintaining structural integrity at elevated temperatures. The baseplate of the tunnel is a stainless-steel sheet coated with a flame proof enamel which is used to control the emissivity of the surface for thermal imaging.

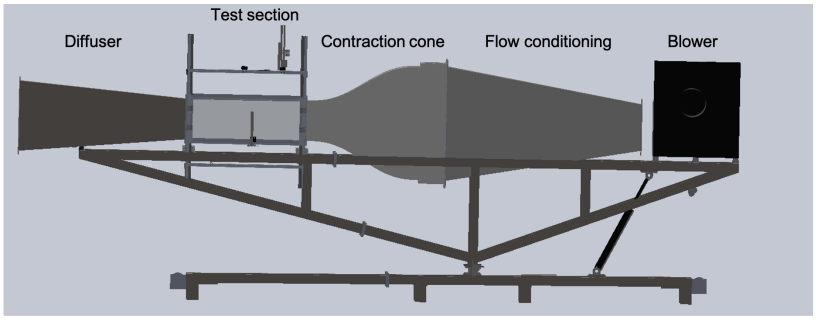

Figure 33: Schematic of the WindCline tilting blow-down wind tunnel.

Notably, the wind tunnel frame was designed around a central axis, about which the tunnel can rotate, like a seesaw. Angle adjustments are performed with a hydraulic piston cylinder assembly. The range of available testing angles is based on the extension length of the hydraulic cylinder. A digital protractor mounted on the baseplate of the test section is used to quantify tilt angle to within 0.05°. In the current configuration, the wind tunnel can operate from -13° (downwards tilt) to +16° (upwards tilt); Figure 34 shows the WindCline in tilt-up and tilt-down configurations.

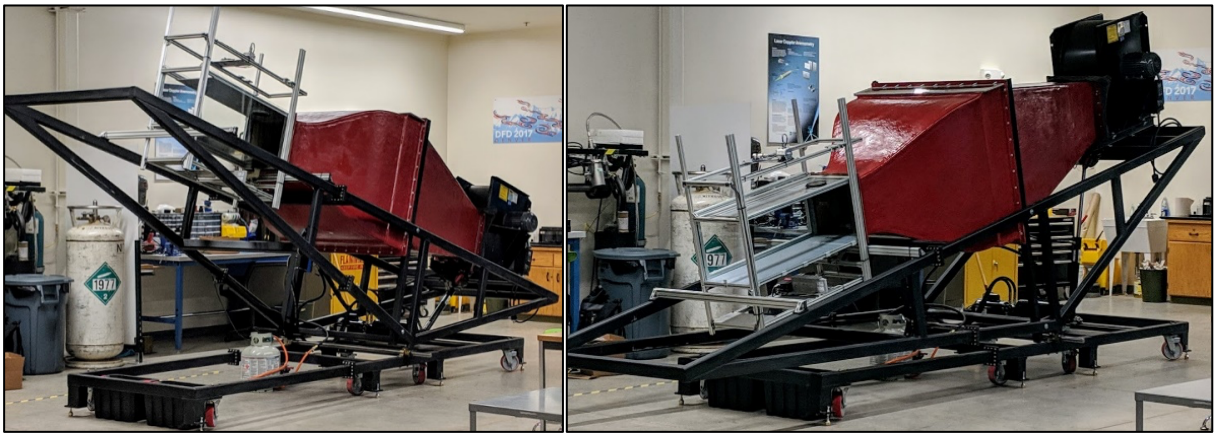

Figure 34: Images of the WindCline in both tilt-up (left) and tilt-down (right) configurations.

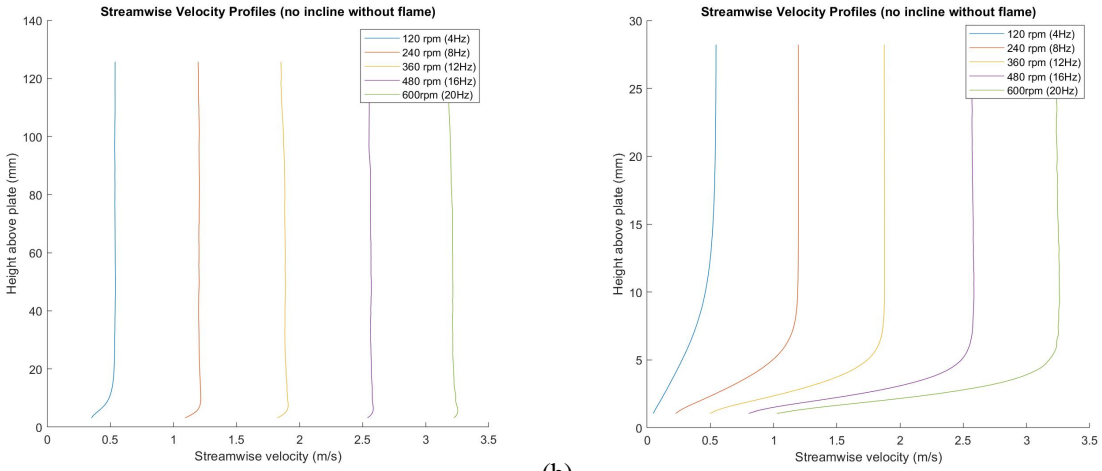

(a) (b)

Figure 35: Streamwise velocity profiles measured using PIV at the beginning of the WindCline test section for different blower speeds. Panel (a) shows a wide field of view and panel (b) shows the boundary layer structure.

7.3.2 Characterization of facility

The WindCline can support flame structure and spread experiments at a wide range of velocities encountered in nature, while also allowing slope experiments. Most importantly, the WindCline has carefully controlled initial and boundary conditions, which is critical for benchmark validation data for simulations. research. To provide high-fidelity inputs to the simulations, particle image velocimetry (PIV) has been used to characterize the inflow velocity profile at the beginning of the WindCline test section, immediately after the contraction cone. These results are shown for a range of blower speeds in Figure 35. Two sets of PIV measurements were performed with different fields of view. In Figure 35(a), a wide field of view was used to measure flow uniformity near the test section centerline; these results show nearly uniform flow at heights great than roughly 10 mm above the test section floor. The narrower field of view in Figure 35(b) reveals the boundary layer structure, which is particularly important in crossflow and flame spread experiments where the primary region of interest is along the bottom wall. The profiles shown in Figure 35 were directly used for the inflow boundary condition in the simulations described in Section 5.3.3.

Initial experiments in the WindCline involved the use of a slot burner at the beginning of the test section, and hot wire anemometry was used to characterize the uniformity of the flow through the burner, as well as the flow velocity. Once more, these results are being used directly in the simulations. In particular, the burner velocity was observed to fluctuate by roughly ±5% and this unsteadiness is being modeled in the simulations.

7.3.3 Results

Two sets of experiments have been performed in the WindCline. In the first experiments, a diffusion flame in cross-flow was created by flowing methane through the burner at the bottom of the test section and igniting immediately above the burner. Flame structure was examined for different wind tunnel speeds, burner flow rates, and wind tunnel inclines; Table 1 provides a summary of the conditions examined. In the second experiment, the metal bottom plate of the test section was replaced with a planed sheet of Douglas fir to measure charring, pyrolysis, and both flame and smoldering combustion in a solid fuel sample.

Case Parameters				Flame Properties		
U magnitude (m/s)	SLPM	Case Number	Incline Angle (deg)	Angle Method #1	Angle Method #2	Centroid Fit
1.2	3	10	-10	7.91	7.85	7
1.2	3	11	0	3.25	4.35	3.81
1.2	3	12	10	3.27	3.9	3.77
1.2	6	4	-10	10.03	8.69	9.43
1.2	6	5	0	9.1	6.65	7.41
1.2	6	6	10	3.87	4.97	5.04
1.2	9	13	-10	9.34	10.93	11.54
1.2	9	14	0	7.89	7.69	8.6
1.2	9	15	10	9.18	8.46	8.43
0.5	6	1	-10	11.02	8.87	11.04
0.5	6	2	0	11.21	9.61	10.78
0.5	6	3	10	10.37	10.04	11.54
1.9	6	7	-10	6.06	4.8	5.49
1.9	6	8	0			
1.9	6	9	10	4.13	3.92	4.07

Table 1: Conditions examined in the WindCline gas phase experiments, showing the tunnel velocity, burner flow rate in SLPM and incline angle. Flame angles measured using different approaches are shown in the last three columns.

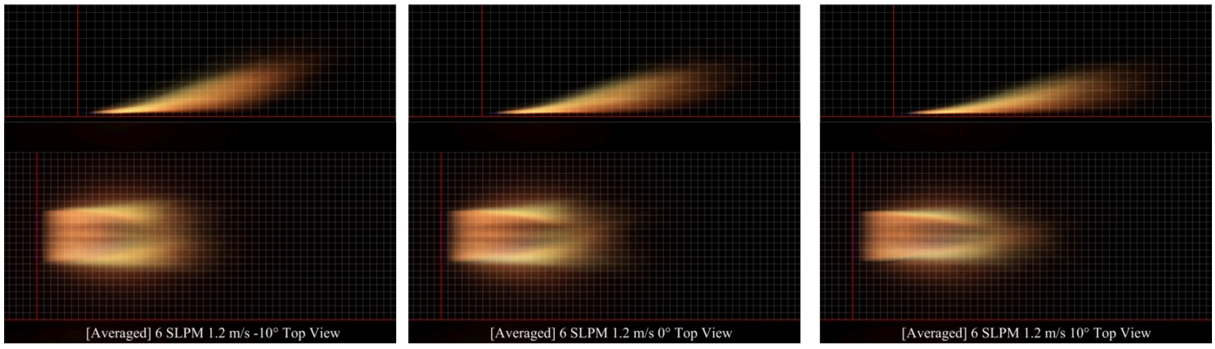

Figure 36: Optical images of the time averaged flame in the WindCline for three different tilt angles: -10°, 0°, and 10° (left to right). Top panels show the side view and bottom panels show the top-down view. The wind tunnel inflow and burner flow rates were 1.2 m/s and 6 SLPM, respectively.

7.3.3a Gas phase experiments

The primary initial focus of these first experiments was on capturing flame structure using optical imaging, resulting in results similar to those shown in Figure 36. In these tests, we observed changing flame angle and flame length with increasing incline. From tilt-down to tilt-up configurations, in particular, we notice longer flames and greater lifting of the flame above the test section floor.

Most notably in these first experiments, near-IR DCS similar to that described in Section 6.1 was used to measure in situ temperature profiles at several downstream locations for one of the test cases. These results are shown in Figure 37, and we observe a lifting of the location of peak temperature with downstream distance. In the future, these measurements will be repeated for additional test cases outlined in Table 1.

The data shown in Figure 37 were used for the simulation validation shown in Figure 14. The bottom temperature boundary condition in the simulations was set isothermally at 500 K based on the measurements near a height of 0 mm shown in Figure 37. In general, the simulation and

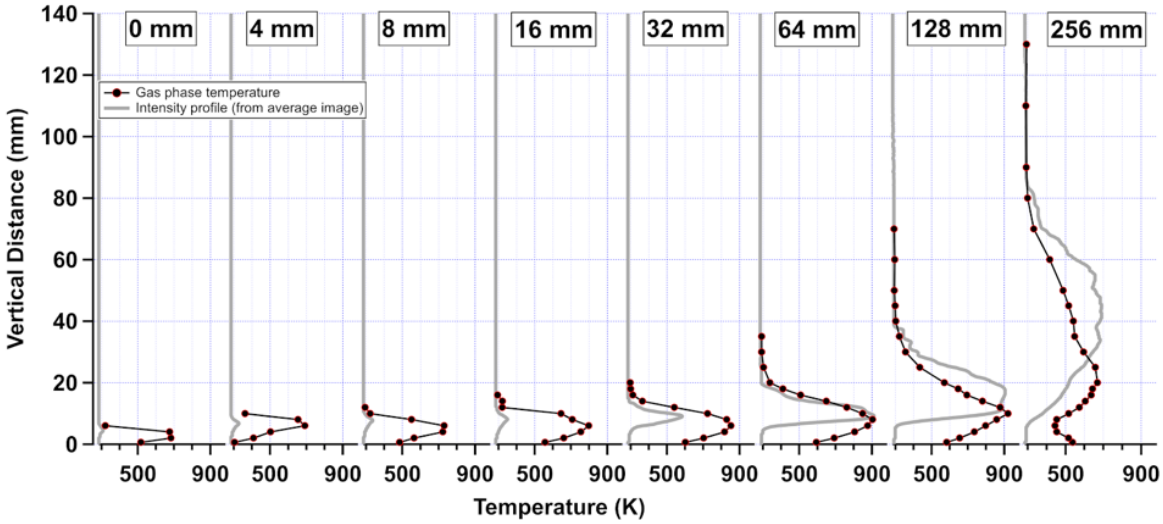

Figure 37: Gas phase temperature profiles measured using near-IR FCLD in the WindCline for a slope of 0° and inflow and burner flow rates of 1.2 m/s and 6 SLPM, respectively.

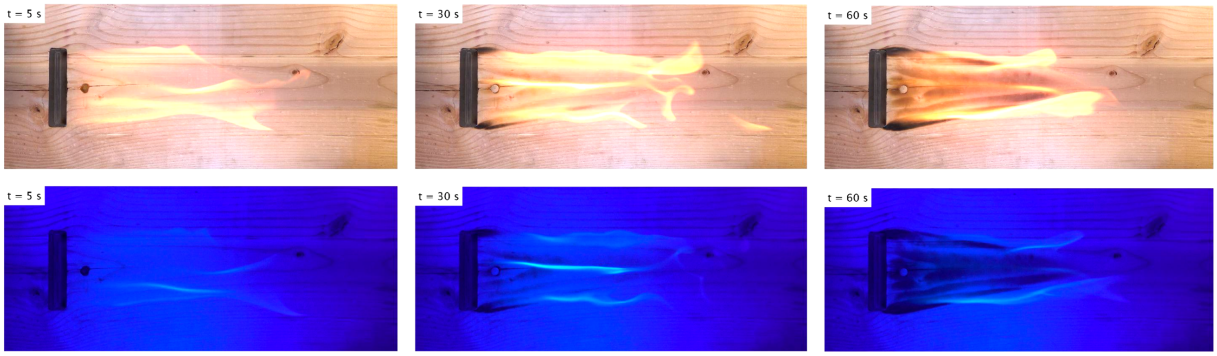

Figure 38: Optical images (top row) and blue light filtered images (bottom row) of the instantaneous flame structure and charring pattern in the WindCline for 0° tilt angle. The wind tunnel inflow and burner flow rates were 1.2 m/s and 6 SLPM, respectively.

experimental results are in good agreement, which is due, in part, to the careful construction and characterization of the WindCline facility.

7.3.3b Solid phase experiments

Initial experiments have been performed with combustion of a solid Douglas fir wood sample in the WindCline test section. The same conditions were used for these tests, and both standard and blue light filtered cameras were used to track the progress of the charring. Figure 38 shows three snapshots from the experiments, where the evolution of the charring can be observed, providing a target for the numerical simulations, which also predict charring. Moreover, experimental measurements of CO, CO_2, and PM2.5 were taken at the exit of the test section. These results, shown in Figure 39, reveal a noticeable transition from flaming to smoldering combustion, where the production of CO and PM2.5 both increase dramatically after the burner is extinguished. These types of measurements over a broader range of conditions are an important direction for future research.

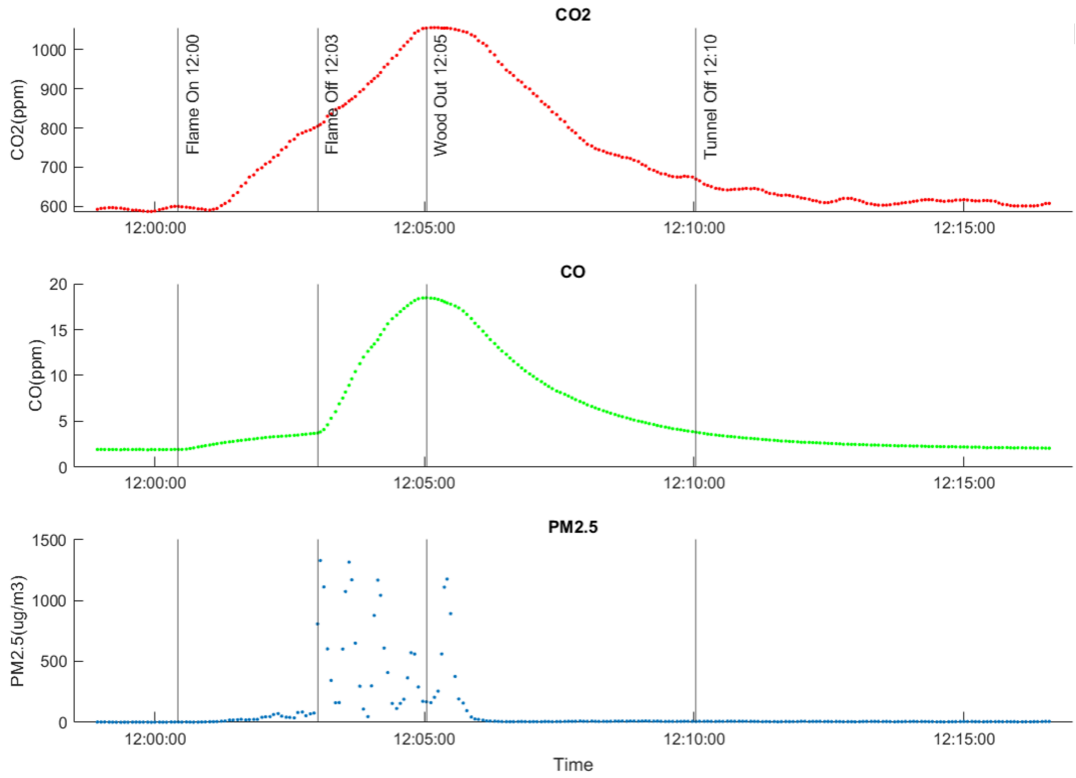

Figure 39: Time series of CO_2, CO and PM2.5 at the exit of the WindCline during the solid phase flame spread experiment shown in Figure 38.

8. Results: Numerical Simulations of Landscape Scale Fires

Large-scale combustion phenomena, such as wildland fires and those impacting the wildland-urban interface (WUI), span large spatial and temporal timescales, ranging temporally from sub-second chemical reactions to much longer time spans characteristic of fire spread and suppression and physically from meter-scale fuel geometry to kilometer-scale topography. Methods to address the temporal scale disparities characteristic of such fires (e.g., assuming infinitely fast chemistry) are often used, but relevant length scales are often dictated by the problem itself (e.g., important geometric and topographical features). In this work we present a new OpenFOAM solver intended to address such spatial scale disparity, targeting important capability outlined in Hanson et al. (2000), specifically the ability to simultaneously resolve important topographical and flame-scale features and employ "grid nesting" to facilitate efficient resolution of such features. We employ adaptive mesh refinement (AMR) to accomplish both tasks, used to add (or remove) resolution at run-time to track features of interest (e.g., a propagating flame) while maintaining low resolution – and low computational cost – in uninteresting regions of the domain.

8.1 AMR Based Computational Solver for Landscape-Scale Simulations

As described previously, we extended the *fireFoam* solver to use AMR for efficient simulation of diffusion flames and small-scale fire spread, resulting in the *diffusionFireFoam* (Lapointe et al., 2020) and *fireDyMFoam* (Lapointe et al., 2020a, 2021) solvers, respectively, and the computational efficiency of dynamic simulations (i.e., using AMR) was demonstrated. The AMR was limited, though, to the gaseous domain to work with native pyrolysis and thin-film functionality. This approach was sufficient because the gas-phase solution comprises the bulk of

the computational expense when solid- or liquid-regions are small (or not present). As a solid region grows, though, this assumption is no longer valid. To address this, we have extended *fireFoam* to incorporate multi-region AMR and three-dimensional (3D) solid-phase pyrolysis modeling functionality. The resulting solver (and associated libraries) is publicly available via GitHub for use by the broader OpenFOAM community.

8.1.1 Solver description

The new solver, *multiRegionFireDymFoam*, is based on the *fireFoam* solver (Wang et al., 2011) and is designed for large-scale fire spread and incorporates one "master" gaseous region and an arbitrary number of solid regions, each with their own computational mesh and thermophysical properties. Each region may use – at user-discretion – AMR; regions are coupled using coupled patches with mapped arbitrary mesh interface (AMI) interpolation, so mesh resolution need not match on at region interfaces.

8.1.1a Governing equations

In the gas phase, 3D Favre-filtered compressible Navier-Stokes equations are solved as described previously. In the solid phase, conservation equations for mass, energy, and species are solved (based on the native OpenFOAM pyrolysis model), in addition to a conservation equation for the diffusion of gas within the solid (Bellais, 2007).

The solver is again used for LES using a one equation eddy viscosity model (Yoshizawa, 1986). Combustion is also assumed to be infinitely fast via the eddy dissipation method (Chen et al., 2014). Radiation modeling is accomplished using a finite-volume implementation of the discrete ordinate method (i.e., fvDOM) with a prescribed radiative fraction. Region coupling is accomplished via mapped boundary conditions for velocity (to map the flux of fuel in the gaseous region to the flux of pyrolyzate in a solid region), temperature (to map temperature in the gaseous region to temperature in the solid) and species (to map pyrolyzate in a solid region to a known fuel in the gaseous region).

Although *fireFoam* also includes thin-film and Lagrangian particle functionality, their use for fire suppression simulations will be the subject of future work; related source terms are not included in the previous equations for brevity.

8.1.1b Solution procedure

Solution of the equations outlined previously is done sequentially, similarly to the procedure used in *fireDyMFoam*. A mesh update is first performed for each region, if required. Then, solid regions are solved, following a procedure like the *reactingOneDim* pyrolysis model. Gas-phase conservation is next solved using the PIMPLE algorithm where we use MULES to bound species and energy transport, following a similar implementation in (UniCFD Lab, 2021, https: //github.com/unicfdlab/hybridCentralSolvers) and *interMixingFoam*.

8.1.2 Solver demonstration

We now demonstrate the new multi-region functionality for a simple fire spread case representative of the WUI, involving flame propagation in the vicinity of a building-like, flammable structure. In the following sections we briefly outline a pre-processing procedure specific to the multi-region AMR before showing some simulation results to highlight fluid- and solid-region time-varying meshes.

8.1.2a Case Setup

The meshing procedure makes use of one "master" case directory, where the primary gaseous region is first created (using *blockMesh* to create the base mesh and *snappyHexMesh* to resolve important geometric features, such as buildings or a heat source). Meshes for solid regions are then created using *extrudeToRegionMesh* and *splitMeshRegions* utilities. A meshing procedure for a single building simulation is therefore summarized as:

1. The "master" gaseous region is first created using *blockMesh*, before using *snappyHexMesh* to resolve the mesh where needed (e.g., in the vicinity of an obstacle or heat source),
2. The "primary" solid region, used to model a large, terrain-like fuel bed, is created using *blockMesh* and *snappyHexMesh* for an independent case, then merged with the "master" case with the *mergeMesh* utility. In contrast to creation with *extrudeToRegionMesh*, this process allows for meshes that aren't necessarily identical at their interface, as well as refinement of key features in the solid,
3. The building-like solid region(s) are created first by removing unnecessary portions of the "master" mesh via *subSetMesh*, followed by using the *extrudeToRegionMesh* utility,
4. Finally, boundaries of the gaseous and solid regions are edited to enable region coupling using AMI interpolation to accommodate the use of AMR.

For this demonstration we model fire spread over a flat, grass-like fuel bed with one building in its center. The primary, gaseous domain uses four levels of AMR for an effective resolution of 1 m. In the solids, two levels of AMR are used to achieve meter-scale resolution in the interface-tangent directions and millimeter-scale in the interface-normal direction. The meshes thus match in resolution at gas-solid region interfaces when at their highest respective levels of refinement. The thermophysical properties of the fuel bed are set similarly to those in Mell et al. (2007) and those for the building are based on solid-phase values used in fireFoam tutorials.

The computational domain is shown in Figure 40(a), where the location of the fire line heat-source and building with respect to the fuel bed (shown in green) are indicated in red and white, respectively, and the gaseous region is outlined in black. Solid region properties are based on those in the *oppositeBurningPanels* tutorial and adjusted in the fuel bed to be more conducive to fire spread, which is driven from left to right by a fixed inflow profile as indicated. This configuration is quite similar (just scaled in size) to recent work using fireFoam to investigate fire spread in the WUI (Ghaderi et al., 2021).

Numerically, first-order temporal and nominally second-order spatial schemes are employed, with central differencing for vector and total variation diminishing (TVD) central differencing for scalar divergence terms and unbounded second order schemes for diffusive terms. Solid regions are similarly first-order in in time and second order in space.

8.1.2b Case results

The simulation is first spun-up without combustion before running for 30 seconds – long enough to demonstrate mesh changes in all regions and ignition of the building. Refinement in each region is based on un-scaled temperature values for simplicity, with a lower bound of 400 K (the upper bound is set to an arbitrarily high value). As mentioned previously, four levels of refinement are used in the gas phase and two are used in each solid. Meshes in the gaseous and solid regions are shown in Figure 40(b) for 30 s, where cell addition in all regions is observed by the final time.

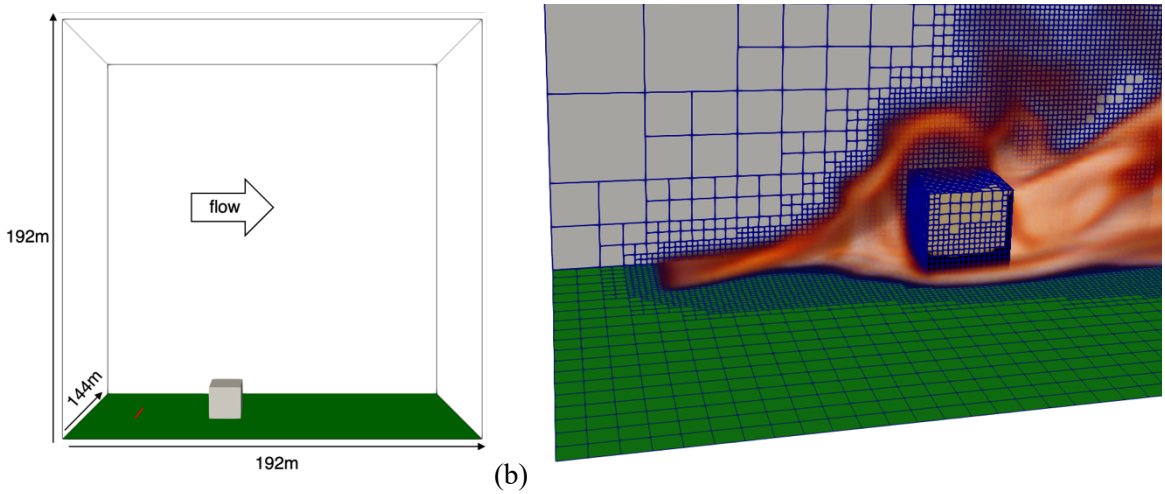

Figure 40: Visualization of simulation at 1 and 30 s highlighting mesh changes in gaseous and solid regions. The fuel bed and building obstacle are colored by char mass fraction from green (low) to black (high) and brown (low) to black (high), respectively. In the gaseous domain a volume render of high temperature is included to visualize fire propagation. Mesh outlines are provided in each region to illustrate where cells have been added.

8.2 AMR Based Landscape-Scale Simulations

Previously, an efficient solver for fire spread and suppression was developed, utilizing AMR in the gas-phase (where computations are most expensive) to identify regions of interest as the simulation is running and increase the physical resolution in those regions. This is particularly efficient when such regions are not known *a priori*, as in the case of fire spread. Additionally, the solver employed quasi-3D solid modeling. A series of independent, one-dimensional computational meshes were used (that together comprised a full 3D volume.

This solver has since been extended to incorporate AMR in the solid phases to further decrease computational cost. Previously, the solid regions needed to be pre-refined to high resolution to enable use of AMR; this constraint has been relaxed. Additionally, solid modeling has been generalized to enable fully 3D modeling. Arbitrary mesh interface (AMI) coupling is employed to couple gaseous and solid regions.

This solver has been demonstrated for two large-scale, wind-driven fire spread cases, both incorporating gas- and solid-phase AMR to decrease computational cost. The first case is representative of the wildland urban interface (WUI) where a propagating fire interacts (and eventually burns) a building-like structure and AMR is used to achieve meter-scale resolution from a nominal resolution of 16-m. A visual rendering of the case setup is shown in Figure 40(a), where the initial fire-line in relation to the structure are visible, in addition to their placement on a large fuel bed within a 100 meter-scale domain. In Figure 40(b) successful spread is shown for a simulation time of 30 seconds. Mesh changes in the gas- and solid-regions are also visualized to show where cells were added by the AMR.

Next, the solver is used to model a slightly more complex problem, where a propagating flame interacts with an array of tree-like obstacles. Here we further leverage the utility of AMR to obtain ~0.25-m. resolution from an initial resolution of 16m. Simulation layout highlighting the fireline location with respect to the group of trees is shown in Figure 41(a); spread is again successfully captured and visualized in Figure 41(b) – having shown that AMR was successful previously, the focus here is on the flame itself.

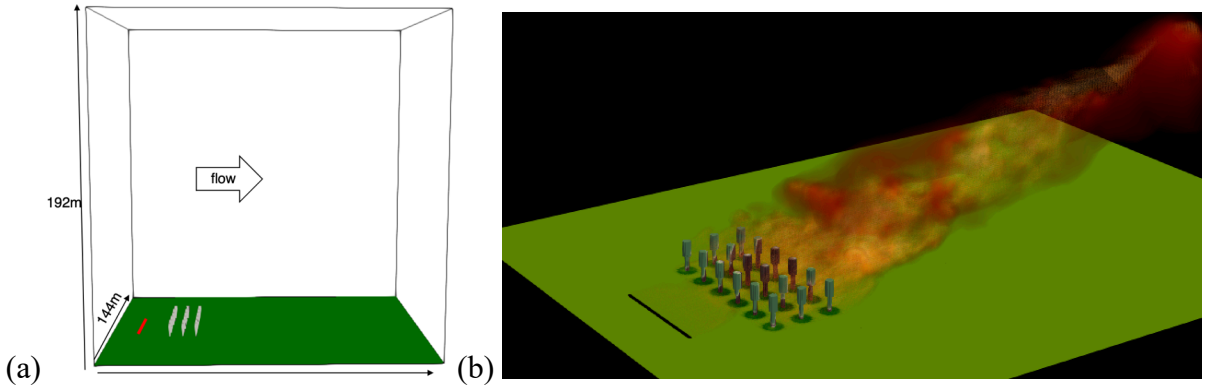

Figure 41: (a) Visual representation of the computational domain for the tree fire spread case, showing the initial fire line (red) and tree grouping (grey) with respect to the fuel bed (green) and gaseous domain; (b) Visualization of resulting fire spread, where fire is represented by a volume render of temperature from low (black) to hot (orange).

9. Conclusions and Implications for Future Research/Implementation

Many important and valuable research findings have resulted from this project, and all are described in detail in the peer-reviewed publications produced during this project. Briefly, the most significant conclusions and research highlights from this project were the following:

1. We have developed the first AMR-based simulation capability for modeling and predictions of fire spread in both built and natural environments. This capability, called fireDyMFoam, is an extension of the OpenFOAM solver fireFoam and provides increased spatial resolution in user-defined regions of interest, resulting in a substantial computational cost reduction. The solver has been verified and validated across a range of cases, and most notably includes the capability to simultaneously use AMR in gas and solid phase regions for complex geometries, enabling future AMR-based simulations of real-world wildland fire scenarios. All solvers developed in this project, including fireDyMFoam, are publicly available at https://github.com/clapointe2011/public.
2. Three new skeletal chemical kinetic models (provided in Appendix B of this report) have been developed and validated for the combustion of gas-phase products resulting from the pyrolysis of Douglas Fir. The smallest 54 species, 204 reaction model had a maximum error of roughly 83% in ignition delay, with an average maximum error of 24%. These errors are reasonable given the complexity and uncertainty involved in modeling solid biomass combustion, although the larger skeletal model, with smaller error, is preferable if sufficient computational resources are available to allow its integration within high-fidelity simulations of wildland fire. These models are now being implemented and tested using fireDyMFoam, with validation data from near-IR FCLD.
3. We developed a new diagnostic suite for small-scale biomass pyrolysis and combustion experiments that combined traditional approaches and modern laser-based sensing to provide the controlled boundary conditions and multi-parameter measurements that are necessary for developing and validating high-resolution chemical kinetic and computational fluid dynamic models. We demonstrated the first uses of both near-IR and mid-IR dual-comb spectroscopy in experiments of biomass evaporation, pyrolysis, ignition, and combustion. The mid-IR experiments were, in fact, the first demonstration of this technology in any combustion

environment. These experiments provided simultaneous high frequency time series of temperature and chemical species concentrations, which were used to validate the chemical kinetic models and simulations. With respect to physical insights obtained, the effects of moisture content on combustion properties were examined using the near-IR experiments, and the production of isotopologues was examined using the mid-IR experiments.

4. We created a novel tilting wind tunnel called the WindCline for experiments of both gas and solid fuel combustion at different wind and topographical conditions. Conditions in the tunnel were carefully controlled and characterized to enable apples-to-apples validation of the simulations. Near-IR FCLD was used to measure temperature profiles in the tunnel for methane diffusion flames in crossflow, and experiments of solid fuel pyrolysis and combustion were performed. Simultaneous simulations of the WindCline cases were also performed, revealing good agreement with the simulation data. Experiments and simulations of additional configurations were also performed to create relationships between flame structure and dynamics, and ambient and topographical conditions.

In the future, we will continue integrating more physics in the simulations and providing tools for simulations of increasingly complex geometries. This will allow efficient simulations of pressing problems including wildland fire spread and suppression. Fire spread case will benefit substantially from the use of AMR, since regions requiring static mesh refinement can be difficult or impossible to predict *a priori* in real-world fire spread problems, resulting in static meshes that are considerably larger than AMR grids. However, ensuring that heat transfer, convection, complex terrain, complex chemistry, and multi-phase flow, among other physical effects, are adequately captured by the AMR requires continued research.

Ongoing work on chemical model reduction is focused on the use of additional performance measures in different flows, such as diffusion flames, as targets for MARS. A multi-dimensional finite volume model in OpenFOAM is currently under development to allow full coupling of pyrolysis and gas chemistry, thus permitting more direct comparisons with experimental data. An additional study will also be performed to quantify the maximum reduction allowable before the induced errors affect major simulation outcomes, as well as to expand to more general biomass flora.

Finally, the near- and mid-IR FCLD must now be used to examine an increasingly broad range of conditions, particularly for new solid fuel types and geometries. This is the focus of a new SERDP project involving many of the same project participants, and new experimental diagnostics will be included to obtain even more complete knowledge of the flow field and chemical composition within the WindCline. Ultimately, these experimental and simulation tools must all be scaled up and applied in the field. This is also an important objective of future research.

10. References

1. M.A. Abbas, Q. Pan, J. Mandon, S.M. Cristescu, F.J.M. Harren, A. Khodabakhsh, Appl. Phys. (2019).
2. Adams, Brian M., et al. "DAKOTA, a multilevel parallel object-oriented framework for design optimization, parameter estimation, uncertainty quantification, and sensitivity analysis: version 5.0 user's manual." *Sandia National Laboratories, Tech. Rep. SAND2010-2183* (2009).
3. Adler, P. Masłowski, A. Foltynowicz, K.C. Cossel, T.C. Briles, I. Hartl, et al., Opt. Express 18 (2010) 21861–21872.
4. Almgren, A. S., et al. (1998) A conservative adaptive projection method for the variable density incompressible Navier–Stokes equations. J. Comput. Phys. 142 (1), 1–46.
5. Abd Alrahman, A. Khodabakhsh, F.M. Schmidt, Z. Qu, A. Foltynowicz, Opt. Express 22 (2014) 13889–13895.
6. H.E. Anderson, Heat transfer and fire spread, res pap INT-RP-69 ogden Utah US dep, Agric. For. Serv. Intermt. For. Range Exp. Stn. 20 (1969) 69. https://www.fs. usda.gov/treesearch/pubs/40489. accessed March 2, 2020.
7. Appelö, D., & Colonius, T. (2009). A high-order super-grid-scale absorbing layer and its application to linear hyperbolic systems. *Journal of Computational Physics*, *228*(11), 4200-4217.
8. Aspden, A.J., et al (2011).: Turbulence-flame interactions in lean premixed hydrogen: transition to the distributed burning regime. J. Fluid Mech. **680**, 287–320
9. Aspden, A.J., et al.: Lewis number effects in distributed flames. Proc. Combust. Inst. **35**, 1321–1329 (2015)
10. Aspden, A.J., et al: Turbulence-chemistry interaction in lean premixed hydrogen combustion. Proc. Combust. Inst. **35**(2), 1321–1329 (2015)
11. Aspden, A.J., et al.: Three-dimensional direct numerical simulation of turbulent lean premixed methane combustion with detailed kinetics. Combust. Flame **166**, 266–283 (2016)
12. Aspden, A.J. et al.: Turbulence-flame interactions in lean premixed dodecane flames. Proc. Combust. Inst. **36**(2), 2005–2016 (2017)
13. Aspden, A.J.: A numerical study of diffusive effects in turbulent lean premixed hydrogen flames. Proc. Combust. Inst. **36**(2), 1997–2004 (2017)
14. A. Atreya, M. Abu-zaid, Effect of environmental variables on piloted ignition, Fire Saf. Sci. 3 (1991) 177–186, https://doi.org/10.3801/iafss.fss.3-177.
15. Baker, T. J. (1997). Mesh adaptation strategies for problems in fluid dynamics. *Finite Elements in Analysis and Design*, *25*(3-4), 243-273.
16. Barbero, et al. (2015). Climate change presents increased potential for very large fires in the contiguous united states. *Int. J. Wildl. Fire* 24, 892–899. doi: 10.1071/WF15083
17. R. Bassilakis, R.M. Carangelo, M.A. Wójtowicz, Fuel 80 (2001) 1765–1786.
18. Bastiaans, R.J.M., et al (2000): Direct and large-eddy simulation of the transition of two- and three-dimensional plane plumes in a confined enclosure. Int. J. Heat Mass Transf. **43**(13), 2375–2393
19. Baumann, F.R. Giorgetta, W.C. Swann, A.M. Zolot, I. Coddington, N.R. Newbury, Phys. Rev. A 84 (2011) 062513.
20. Bell, J. B., et al. (2005). Numerical simulation of a laboratory-scale turbulent V-flame. Proc. Natl Acad. Sci. USA 102 (29), 10006–10011.

21. M. Bellais, “Modelling of the pyrolysis of large wood particles,” Ph.D. dissertation, KTH, 2007. [Online]. Available: https://www.diva-portal.org/smash/record.jsf?pid=diva2%3A12258&dswid=1079
22. Bharadwaj, K. K. & Das, D. (2017) Global instability analysis and experiments on buoyant plumes. J. Fluid Mech. 832, 97–145.
23. Bharadwaj, K. K. & Das, D. (2019) Puffing in planar buoyant plumes: BiGlobal instability analysis and experiments. J. Fluid Mech. 863, 817–849.
24. Blanquart, G., Pitsch, H. (2008): Large-Eddy Simulation of a Turbulent Buoyant Helium Plume, pp. 245–252. Center for Turbulence Research Annual Research Briefs, Stanford University and NASA-Ames Research Center, Stanford
25. Brown, P.N., et al (1989) .: VODE: a variable coefficient ODE solver. SIAM J. Sci. Stat. Comput. **10**, 1038–1051
26. Burton, G.C (2008).: Large-Eddy Simulation of a Turbulent Helium–Air Plume Using the nLES Method, pp. 261–271. Center for Turbulence Research Annual Research Briefs, Stanford University and NASA-Ames Research Center, Stanford
27. Cetegen, B. M. & Kasper, K. D. 1996 Experiments on the oscillatory behavior of buoyant plumes of helium and helium–air mixtures. Phys. Fluids 8 (11), 2974–2984
28. Cetegen, B. M., Dong, Y. & Soteriou, M. C. (1998) Experiments on stability and oscillatory behavior of planar buoyant plumes. Phys. Fluids 10 (7), 1658–1665.
29. Chaos, et al. Evaluation of optimization schemes and determination of solid fuel properties for cfd fire models using bench-scale pyrolysis tests. Proceedings of the Combustion Institute, 33(2):2599–2606, 2011a.
30. Chaos, et al. Experiments and modeling of single-and triple-wall corrugated cardboard: Effective material properties and fire behavior. Fire and Materials, pages 625–636, 2011b.
31. Christopher, et al, Parameter estimation for complex thermal-fluid flows using approxi-mate Bayesian computation, Physical Review Fluids 3 (2018) 10460
32. Colella, P. (1990). Multidimensional upwind methods for hyperbolic conservation laws. Journal of Computational Physics, 87, 171–200.
33. Chung, W., Devaud, C.B (2008).: Buoyancy-corrected k-epsilon models and large Eddy simulation applied to a large axisymmetric helium plume. Int. J. Numer. Meth. Fluids **58**, 57–89
34. Chen, et al. (2014a). Extension of the eddy dissipation concept and smoke point soot model to the LES frame for fire simulations. Fire Saf. J., 64:12–26.
35. Chen, et al. (2014b). Large eddy simulation of a medium-scale methanol pool fire using the extended eddy dissipation concept. Int. J. Heat Mass Transf., 70 pp. 389-408
36. S. Coburn, C.B. Alden, R. Wright, K. Cossel, E. Baumann, G.-W. Truong, F. Giorgetta, C. Sweeney, N.R. Newbury, K. Prasad, I. Coddington, G.B. Rieker, Regional trace-gas source attribution using a field-deployed dual frequency comb spectrometer, Optica 5 (2018) 320–327, https://doi.org/10.1364/ OPTICA.5.000320.
37. Coddington, et al. Dual-comb spectroscopy, Optica 3 (2016)414–426
38. Coen, J. L., M. Cameron, J. Michalakes, E. G. Patton, P. J. Riggan, and K. M. Yedinak. "WRF-Fire: Coupled Weather–Wildland Fire Modeling with the Weather Research and Forecasting Model." *Journal of Applied Meteorology and Climatology* 52 (2013): 16-38.
39. R.K. Cole, A.S. Makowiecki, N. Hoghooghi, G.B. Rieker, Opt. Express 27 (2019) 37920–37939.

40. Day, M. S. & Bell, J. B. (2000) Numerical simulation of laminar reacting flows with complex chemistry. Combust. Theor. Model. 4 (4), 535–556
41. Deardorff, James W. "Stratocumulus-capped mixed layers derived from a three-dimensional model." Boundary-Layer Meteorology 18.4 (1980): 495-527.
42. DesJardin, P.E., et al (2004).: Large eddy simulation and experimental measurements of the near-field of a large turbulent helium plume. Phys. Fluids **16**(6), 1866–1883
43. Diddams, S. A. (2010). The evolving optical frequency comb. *JOSA B*, *27*(11), B51-B62.
44. Doom, J., et al. (2007). A numerical method for DNS/LES of turbulent reacting flows. *Journal of Computational Physics*, *226*(1), 1136-1151.
45. A.D. Draper, R.K. Cole, A.S. Makowiecki, J. Mohr, A. Zdanowicz, A. Marchese, N. Hoghooghi, G.B. Rieker, Broadband dual-frequency comb spectroscopy in a rapid compression machine, Optic Express 27 (2019) 10814–10825, https://doi. org/10.1364/OE.27.010814.
46. Ern, A., Giovangigli, V (2004) .: EGlib: A general-purpose fortran library for multicomponent transport property evaluation. Manual of EGlib version 3
47. Evans, R. J., and T. A. Milne. "Molecular Characterization of the Pyrolysis of Biomass. 1. Fundamentals." *Energy and Fuels* 1 (1987): 123.
48. J. Faist, G. Villares, G. Scalari, M. Rösch, C. Bonzon, A. Hugi, et al., Nanophotonics 5 (2016) 272–291.
49. Faravelli, T., et al. (2010). Detailed kinetic modeling of the thermal degradation of lignins. *Biomass Bioenergy* 34, 290–301. doi: 10.1016/j.biombioe.2009.10.018
50. S.C. Ferguson, A. Dahale, B. Shotorban, S. Mahalingam, D.R. Weise, The role of moisture on combustion of pyrolysis gases in wildland fires, Combust. Sci. Technol. 185 (2013) 435–453, https://doi.org/10.1080/00102202.2012.726666.
51. FM Global (2017). Firefoam development repository. Github.
52. Fukumoto, et al. Large eddy simulation of upward flame spread on PMMA walls with a fully coupled fluid-solid approach. Combustion and Flame, 190:365–387, 2018
53. Gardiner, T. A., & Stone, J. M. (2008). An unsplit Godunov method for ideal MHD via constrained transport in three dimensions. *Journal of Computational Physics*, *227*(8), 4123-4141.
54. A. Gessler, J.P. Ferrio, R. Hommel, K. Treydte, R.A. Werner, R.K. Monson, Tree Physiol. 34 (2014) 796–818.
55. M. Ghaderi, M. Ghodrat, and J. Sharples, "Les simulation of wind-driven wildfire interaction with idealized structures in the wildland-urban interface," Atmosphere, vol. 12, no. 1, p. 21, 2021.
56. Glusman, J. F., et al. (2019). Reduced Gas-Phase Kinetic Models for Burning of Douglas Fir. *Frontiers in Mechanical Engineering*, *5*, 40.
57. I.E. Gordon, L.S. Rothman, C. Hill, et al., J. Quant. Spectrosc. Radiat. Transf. 203 (2017) 3–69.
58. Gulla, B. (2014). Model citizens: open-source fire research.
59. Hall, L. (2006). Many Good Years with Jila. In *Proceedings Of The John Hall Symposium: In Honor of John Hall on the Occasion of His 70th Birthday* (pp. 83-84).
60. Hanson, et al. The potential and promise of physics-based wildfire simulation, Environmental Science & Policy 3 (2000) 161–172
61. Hamins, A., Yang, J. C. & Kashiwagi, T. 1992 An experimental investigation of the pulsation frequency of flames. Symp. (Intl) Combust. 24 (1), 1695–1702.

62. T. Harada, Time to ignition, heat release rate and fire endurance time of wood in cone calorimeter test, Fire Mater. 25 (2001) 161–167, https://doi.org/10.1002/ fam.766.
63. T.R.S. Hayden, N. Malarich, D. Petrykowski, S.P. Nigam, J.D. Christopher, C. Lapointe, N.T. Wimer, P.E. Hamlington, G.B. Rieker, OH radical measurements in combustion environments using wavelength modulation spectroscopy and dual- frequency comb spectroscopy near 1491 nm, Appl. Phys. B 125 (2019) 226, https://doi.org/10.1007/s00340-019-7341-6.
64. D.I. Herman, E.M. Waxman, G. Ycas, F.R. Giorgetta, N.R. Newbury, I.R. Coddington, J. Mol. Spectrosc. 356 (2019) 39–45.
65. Hiremath, V. et al. (2013). Large-scale parallel simulations of turbulent combustion using combined dimension reduction and tabulation of chemistry. *Proc. Combust. Inst.* 34, 205–215. doi: 10.1016/j.proci.2012.06.004
66. hyStrath repository 2021. Github.
67. Jarvis, M. W., et al. "Elucidation of Biomass Pyrolysis Products Using a Laminar Entrained Flow Reactor and Char Particle Imaging." *Energy and Fuels* 25 (2011): 324-336.
68. Jasak, H and A.D. Gosman. Automatic resolution control for the finite-volume method, Part 1: a-posteriori error estimates. Numer. Heat Transf., Part B: Fundamentals, 38 (3) (2000), pp. 237-256
69. Jasak, H and A.D. Gosman. Automatic resolution control for the finite-volume method, Part 2: adaptive mesh refinement and coarsening. Numer. Heat Transf., Part B: Fundamentals, 38 (3) (2000), pp. 257-271
70. Jasak, H. and A.D. Gosman. Automatic resolution control for the finite-volume method, Part 3: turbulent flow applications. Numer. Heat Transf., Part B: Fundamentals, 38 (3) (2000), pp. 273-290
71. Jatale, A., et al. (2015).: Application of a verification, validation and uncertainty quantification framework to a turbulent Buoyant helium plume. Flow Turbul. Combust. **95**(1), 143–168
72. T.J. Johnson, L.T.M. Profeta, R.L. Sams, D.W.T. Griffith, R.L. Yokelson, Vib. Spectrosc. 53 (2010) 97–102, doi:10.1016/j.vibspec.2010.02.010.
73. Jones, W. P., and R. P. Lindstedt. "Global reaction schemes for hydrocarbon combustion." *Combustion and flame* 73.3 (1988): 233-249.
74. O. Kara, L. Maidment, T. Gardiner, P.G. Schunemann, D.T. Reid, Opt. Express. 25 (2017) 32713–32721.
75. Kazakov, A., and Frenklach, M. (1995). *Reduced Reaction Sets Based on GRI-Mech 1.2*.
76. Kadem, *et al.* 2011
77. Lapointe, C., et al. (2020). Efficient simulation of turbulent diffusion flames in OpenFOAM using adaptive mesh refinement. *Fire Safety Journal*, *111*, 102934.
78. Lapointe, C. B. (2020). *Efficient Simulation of Complex Fire Phenomena in OpenFOAM Using Adaptive Mesh Refinement* (Doctoral dissertation, University of Colorado at Boulder).
79. C. Lapointe, N. Wimer, J. Glusman, P. Sardana, A. Makowiecki, J. Daily, G. Rieker, and P. Hamlington, "Efficient simulations of propagating flames using adaptive mesh refinement," arXiv preprint arXiv:2102.09349, 2021. [Online]. Available: https://arxiv.org/abs/2102.09349
80. Lee. Numerical analysis on the rapid fire suppression using a water mist nozzle in a fire compartment with a door opening. Nuclear Engineering and Technology, 51(2):410–423, 2019.

81. Linn, Rodman Ray. *A transport model for prediction of wildfire behavior*. No. LA-13334-T. Los Alamos National Lab., NM (United States), 1997.
82. Linn, Rodman, et al. (2002). Studying wildfire behavior using FIRETEC. *International journal of wildland fire* 11.4: 233-246.
83. Linn, R. R., J. L. Winterkamp, D. R. Weise, and C. Edminster. "A numerical study of slope and fuel structure effects on coupled wildlfire behavior." *International Journal of Wildland Fire* 19 (2010): 179-201.
84. C. Lu, F.S. Vieira, F.M. Schmidt, A. Foltynowicz, Opt. Express 27 (2019) 29521–29533.
85. Makowiecki, A. S., et al. (2020). Dual frequency comb spectroscopy of solid fuel pyrolysis and combustion: Quantifying the influence of moisture content in Douglas fir. *Fire Safety Journal* 116: 103185.
86. Makowiecki, A. S., et al. (2021). Mid-infrared dual frequency comb spectroscopy for combustion analysis from 2.8 to 5 μm. *Proceedings of the Combustion Institute*, *38*(1), 1627-1635.
87. Maragkos, G et al. (2012).: Application of FDS and FireFOAM in large eddy simulations of a turbulent buoyant helium plume. Combust. Sci. Technol. **184**(7–8), 1108–1120
88. Maragkos, G., et al. (2013).: Large Eddy simulations of the flow in the near-field region of a turbulent buoyant helium plume. Flow Turbul. Combust. **90**(3), 511–543
89. Maragkos, G. and B. Merci. Large eddy simulations of CH4 fire plumes. Flow, Turbul. Combust., 99 (1) (2017), pp. 239-278
90. S. McAllister, Critical mass flux for flaming ignition of wet wood, Fire Saf. J. 61 (2013) 200–206, https://doi.org/10.1016/j.firesaf.2013.09.002.
91. McGrattan, K., et al. (2013). Fire dynamics simulator user's guide. *NIST special publication*, *1019*(6).
92. Mell, W. E., R. J. McDermott and G. P. Forney (2010). Wildland fire behavior modeling: perspectives, new approaches and applications. Proceedings of 3rd Fire Behavior and Fuels Conference,, Spokane, Washington, USA.
93. Mell, William, et al. (2007). A physics-based approach to modelling grassland fires. International Journal of Wildland Fire 16.1: 1-22.
94. Meredith, et al. A numerical model for simulation of thin-film water transport over solid fuel surfaces. Fire Safety Science, 10:415–428, 2011a
95. Meredith, et al. A numerical model for partially-wetted flow of thin liquid films. Computational Methods in Multiphase Flow VI, 70:239, 2011b.
96. Meredith, et al. A comprehensive model for simulating the interaction of water with solid surfaces in fire suppression environments. Proceedings of the Combustion Institute,34(2):2719–2726, 2013.
97. B. Moghtaderi, V. Novozhilov, D.F. Fletcher, J.H. Kent, A new correlation for bench-scale piloted ignition data of wood, Fire Saf. J. 29 (1997) 41–59, https://doi. org/10.1016/S0379-7112(97)00004-0.
98. Morvan, D. "Physical Phenomena and Length Scales Governing the Behaviour of Wildfires: A Case for Physical Modelling." *Fire Technology* 47 (2011): 437-460.
99. A.V. Muraviev, V.O. Smolski, Z.E. Loparo, K.L. Vodopyanov, Nat. Photon. 12 (2018) 209.
100. N. Nader, A. Kowligy, J. Chiles, E.J. Stanton, H. Timmers, A.J. Lind, et al., Optica 6 (2019) 1269.
101. Newbury, N. R. (2011). Searching for applications with a fine-tooth comb. *Nature photonics*, *5*(4), 186-188.

102. Niemeyer et al. Skeletal mechanism generation for surrogate fuels using directed relation graph with error propagation and sensitivity analysis. Combustion and Dlame, 157 (9) (2010), pp. 1760-1770
103. Niemeyer, K. E., and Sung, C.-J. (2011). On the importance of graph search algorithms for drgep-based mechanism reduction methods. *Combust. Flame* 158, 1439–1443. doi: 10.1016/j.combustflame.2010.12.010
104. Niemeyer, K. E., and Sung, C.-J. (2014). Mechanism reduction for multicomponent surrogates: a case study using toluene reference fuels. *Combust. Flame* 161, 2752–2764. doi: 10.1016/j.combustflame.2014.05.001
105. Niemeyer, K. E., and Sung, C.-J. (2015). Reduced chemistry for a gasoline surrogate valid at engine-relevant conditions. *Energy Fuels* 29, 1172–1185. doi: 10.1021/ef5022126
106. NIST : Proceedings of the first workshop organized by the IAFSS working group on measurement and computation of fire phenomena (MaCFP). Fire Saf. J. **101**, 1–17
107. Nonaka, A., et al. (2012) A deferred correction coupling strategy for low Mach number flow with complex chemistry. Combust. Theor. Model. 16 (6), 1053–1088.
108. Nonaka, A., et al. (2018).: A conservative, thermodynamically consistent numerical approach for low Mach number combustion. Part I: Single-level integration. Combust. Theor. Model. **22**(1), 156–184
109. O'Hern, T.J., et al.: Experimental study of a turbulent Buoyant helium plume. J. Fluid Mech. **544**, 143–171 (2005)
110. OpenFOAM. The OpenFOAM Foundation. https://openfoam.org/ (2018)
111. Pantano, C., et al. (2003). Mixing of a conserved scalar in a turbulent reacting shear layer. *Journal of Fluid Mechanics*, *481*, 291-328.
112. Pazner, W.E., et al. (2016).: A high-order spectral deferred correction strategy for low Mach number flow with complex chemistry. Combust. Theor. Model. **20**(3), 521–547
113. Pham, M.V., et al (2007).: Direct and large-Eddy simulations of a pure thermal plume. Phys. Fluids **19**(12), 125103
114. N.H. Pinkowski, Y. Ding, C.L. Strand, R.K. Hanson, R. Horvath, M. Geiser, Meas. Sci. Tech. 31 (2020) 055501.
115. Poinsot, T. J. A., & Lele, S. K. (1992). Boundary conditions for direct simulations of compressible viscous flows. *Journal of computational physics*, *101*(1), 104-129.
116. Poludnenko, A. Y., & Oran, E. S. (2010). The interaction of high-speed turbulence with flames: Global properties and internal flame structure. *Combustion and Flame*, *157*(5), 995-1011.
117. Poludnenko, A. Y., & Oran, E. S. (2011). The interaction of high-speed turbulence with flames: Turbulent flame speed. *Combustion and flame*, *158*(2), 301-326.
118. Pope, S.B. Computationally efficient implementation of combustion chemistry using in situ adaptive tabulation. Combust. Theor. Model., 1 (1) (1997), pp. 41-63
119. Ranzi, E., et al. (2008). Chemical kinetics of biomass pyrolysis. *Energy Fuels* 22, 4292–4300. doi: 10.1021/ef800551t
120. Ranzi, E., et al. (2001). Lumping procedures in detailed kinetic modeling of gasification, pyrolysis, partial oxidation and combustion of hydrocarbon mixtures. *Prog. Energy Combust. Sci.* 27, 99–139. doi: 10.1016/S0360-1285(00)00013-7
121. Rieker, G. B., et. al. (2014). Frequency-comb-based remote sensing of greenhouse gases over kilometer air paths. *Optica*, *1*(5), 290-298.
122. Reaction Design (2011). CHEMKIN 10112 Reaction Design, San Diego

123. Ren, et al. Large-scale fire suppression modeling of corrugated cardboard boxes on wood pallets in rack-storage configurations. Fire Safety Journal, 91:695–704, 2017
124. Ren, et al. Large eddy simulation of turbulent vertical wall fires supplied with gaseous fuel through porous burners.Combustion and Flame, 169:194–208, 2016.
125. Rettenmaier, et al. Load balanced 2d and 3d adaptive mesh refinement in openfoam. SoftwareX, 10:100317,2019
126. Rothermal, R. C. "A mathematical model for predicting fire spread in wildland fuels. USDA Forest Service, Intermount." For. Range Exp. Stn., Ogden, UT, Res. Pap. INT-115 (1972).
127. L.S. Rothman, I.E. Gordon, Y. Babikov, A. Barbe, D. Chris Benner, P.F. Bernath, M. Birk, L. Bizzocchi, V. Boudon, L.R. Brown, A. Campargue, K. Chance, E. A. Cohen, L.H. Coudert, V.M. Devi, B.J. Drouin, A. Fayt, J.-M. Flaud, R. R. Gamache, J.J. Harrison, J.-M. Hartmann, C. Hill, J.T. Hodges, D. Jacquemart, A. Jolly, J. Lamouroux, R.J. Le Roy, G. Li, D.A. Long, O.M. Lyulin, C.J. Mackie, S. T. Massie, S. Mikhailenko, H.S.P. Müller, O.V. Naumenko, A.V. Nikitin, J. Orphal, V. Perevalov, A. Perrin, E.R. Polovtseva, C. Richard, M.A.H. Smith, E. Starikova, K. Sung, S. Tashkun, J. Tennyson, G.C. Toon, VlG. Tyuterev, G. Wagner, The HITRAN2012 molecular spectroscopic database, J. Quant. Spectrosc. Radiat. Transf. 130 (2013) 4–50, https://doi.org/10.1016/j.jqsrt.2013.07.002.
128. Sadiek, T. Mikkonen, M. Vainio, J. Toivonen, Foltynowicz, Phys. Chem. Chem. Phys. 20 (2018) 27849–27855.
129. Saltzman, J. (1994): An unsplit 3D upwind method for hyperbolic conservation laws. J. Comput. Phys. **115**, 153–168 (1994)
130. N.K. Scharko, A.M. Oeck, R.G. Tonkyn, et al., Atmos. Meas. Tech. 12 (2019) 763–776.
131. A. Schliesser, N. Picqué, T.W. Hänsch, Nat. Photon. 6 (2012) 440–449.
132. Schwetz, K., and Lipp, A. (1985). Ullmann's encyclopedia of industrial chemistry. *VCH: Deerfield Beach* 28:315.
133. Schroeder, et al., Dual frequency comb laser absorption spectroscopy in a 16 MW gas turbine exhaust, Proceedings of the Combustion Institute 36 (2017) 4565–4573
134. P.J. Schroeder, D.J. Pfotenhauer, J. Yang, F.R. Giorgetta, W.C. Swann, I. Coddington, N.R. Newbury, G.B. Rieker, High temperature comparison of the HITRAN2012 and HITEMP2010 water vapor absorption databases to frequency comb measurements, J. Quant. Spectrosc. Radiat. Transf. 203 (2017) 194–205, https://doi.org/10.1016/j.jqsrt.2017.04.023.
135. P.J. Schroeder, M.J. Cich, J. Yang, F.R. Giorgetta, W.C. Swann, I. Coddington, N. R. Newbury, B.J. Drouin, G.B. Rieker, Speed-dependent Voigt lineshape parameter database from dual frequency comb measurements up to 1305 K. Part I: pure H2O absorption, 6801–7188 cm-1 1, J. Quant. Spectrosc. Radiat. Transf. 210 (2018) 240–250, https://doi.org/10.1016/j.jqsrt.2018.02.025.
136. S.W. Sharpe, R.L. Sams, T.J. Johnson, in: Proceed- ings of the Applied Imagery Pattern Recognition Workshop, 2002, pp. 45–48.
137. Singer, and Pope. Exploiting ISAT to solve the reaction-diffusion equation. Combust. Theor. Model., 8 (2) (2004), pp. 361-383.
138. Singer et al. Operator-splitting with ISAT to model reacting flow with detailed chemistry. Combust. Theor. Model., 10 (2) (2006), pp. 199-217
139. Smagorinsky, J. General circulation experiments with the primitive equations Mon. Weath. Rev., 91 (3) (1963), pp. 99-164

140. Smith, G. P., et al. *GRI-Mech Home Page.* 2015. http://www.me.berkeley.edu/gri_mech/ (accessed March 7, 2015).
141. M.J. Spearpoint, J.G. Quintiere, Predicting the piloted ignition of wood in the cone calorimeter using an integral model — effect of species, grain orientation and heat flux, Fire Saf. J. 36 (2001) 391–415, https://doi.org/10.1016/S0379-7112(00) 00055-2.
142. L.A. Sterczewski, J. Westberg, M. Bagheri, C. Frez, I. Vurgaftman, C.L. Canedy, et al., Opt. Lett. 44 (2019) 2113–2116.
143. Stone, J. M., et al. (2008). Athena: a new code for astrophysical MHD. *The Astrophysical Journal Supplement Series*, *178*(1), 137.
144. Sullivan, A. L. "Wildland surface fire spread modelling, 1990–2007. 1: Physical and quasi-physical models." *International Journal of Wildland Fire* 18 (2009): 349-368.
145. Tekgül, Bulut, et al. "DLBFoam: An open-source dynamic load balancing model for fast reacting flow simulations in OpenFOAM." *arXiv preprint arXiv:2011.07978* (2020).
146. R. Timmers, A. Kowligy, A. Lind, F.C. Cruz, N. Nader, M. Silfies, et al., Optica 5 (2018) 727–732.
147. Vinayak. Mathematical Modeling & Simulation of Pyrolysis & Flame Spread in OpenFOAM. Master's thesis, 2017
148. Vilfayeau, et al. Numerical simulation of under-ventilated liquid-fueled compartment fires with flame extinction and thermally-driven fuel evaporation. Proceedings of the Combustion Institute, 35(3):2563–2571, 201
149. Wang, Y. et al. Large eddy simulation of fire plumes. Proc. Combust. Inst., 33 (2) (2011), pp. 2473-2480
150. Wang et al. Optimization of water mist droplet size by using cfd modeling for fire suppressions. Journal of Loss Prevention in the Process Industries, 44:626–632, 2016
151. E.M. Waxman, K.C. Cossel, G.W. Truong, F.R. Giorgetta, W.C. Swann, S. Coburn, R. J. Wright, G.B. Rieker, I.R. Coddington, N.R. Newbury, Comparison of open-path dual frequency comb spectroscopy for high-precision atmospheric gas measurements, Atmospheric Meas. Tech. (2017), https://doi.org/10.5194/amt-10- 3295-2017.
152. Weller, H.G. et al. A tensorial approach to computational continuum mechanics using object-oriented techniques. Comput. Phys., 12 (6) (1998), pp. 620-631
153. Westbrook, C. K., & Dryer, F. L. (1984). Chemical kinetic modeling of hydrocarbon combustion. *Progress in energy and combustion science*, *10*(1), 1-57.
154. Westerling, A. L., H. G. Hidalgo, D. R. Cayan, and T. W. Swetnam. "Warming and Earlier Spring Increase Western U.S. Forest Wildfire Activity." *Science* 313 (2006): 940-943.
155. Wimer, N., et al (2017). Direct Numerical Simulation of Wildland Fires at Small Scales. In *APS Division of Fluid Dynamics Meeting Abstracts* (pp. D35-006).
156. Wimer, N. T., et al (2020). Scaling of the puffing Strouhal number for buoyant jets and plumes. *Journal of Fluid Mechanics*, *895*.
157. Wimer, N. T., et al. (2021). Numerical simulations of buoyancy-driven flows using adaptive mesh refinement: structure and dynamics of a large-scale helium plume. *Theoretical and Computational Fluid Dynamics*, *35*(1), 61-91.
158. Worthy, J., Rubini, P (2005).: A study of LES stress and flux models applied to a buoyant jet. Numer. Heat Transf. B Fundam. **48**(3), 235–256
159. G. Ycas, F.R. Giorgetta, E. Baumann, I. Coddington, D. Herman, S.A. Diddams, et al., Nat. Photon. 12 (2018) 202.
160. G. Ycas, F.R. Giorgetta, K.C. Cossel, et al., Optica 6 (2019) 165–168.

161. R.J. Yokelson, D.W.T. Griffith, D.E. Ward, Open-path Fourier transform infrared studies of large-scale laboratory biomass fires, J. Geophys. Res. Atmospheres. 101 (1996) 21067–21080, https://doi.org/10.1029/96JD01800.
162. R.J. Yokelson, R. Susott, D.E. Ward, J. Reardon, D.W.T. Griffith, J. Geophys. Res. Atmos. 102 (1997) 18865–18877.
163. R.J. Yokelson, J.G. Goode, D.E. Ward, R.A. Susott, R.E. Babbitt, D.D. Wade, I. Bertschi, D.W.T. Griffith, W.M. Hao, Emissions of formaldehyde, acetic acid, methanol, and other trace gases from biomass fires in North Carolina measured by airborne Fourier transform infrared spectroscopy, J. Geophys. Res. Atmospheres 104 (1999) 30109–30125, https://doi.org/10.1029/1999JD900817.
164. A. Yoshizawa, "Statistical theory for compressible turbulent shear flows, with the application to subgrid modeling," The Physics of Fluids, vol. 29, no. 7, pp. 2152–2164, 1986.
165. Younsi, R., et al. (2010). A high-temperature thermal treatment of wood using a multiscale computational model: Application to wood poles. *Bioresource technology*, *101*(12), 4630-4638.
166. Zhang, W., et al (2019).: AMReX: a framework for block-structured adaptive mesh refinement. J. Open Source Softw. **4**(37), 1370
167. Zhou, X., & Mahalingam, S. (2001). Evaluation of reduced mechanism for modeling combustion of pyrolysis gas in wildland fire. *Combustion Science and Technology*, *171*(1), 39-70.
168. Zhou, X., et al (2001a).: Large-eddy simulation of a turbulent forced plume. Eur. J. Mech. B/Fluids **20**(2), 233–254
169. Zhou, X., et al (2001b) .: Study of density effects in turbulent buoyant jets using Large-Eddy simulation. Theor. Comput. Fluid Dyn. **15**(2), 95–120
170. Zhou, X., Pakdee, W., & Mahalingam, S. (2004). Assessment of a flame surface density-based subgrid turbulent combustion model for nonpremixed flames of wood pyrolysis gas. *Physics of Fluids*, *16*(10), 3795-3807.
171. Zhou, X., Mahalingam, S., & Weise, D. (2005). Modeling of marginal burning state of fire spread in live chaparral shrub fuel bed. Combustion and Flame, 143(3), 183-198.
172. Zhou, X., Mahalingam, S., & Weise, D. (2007). Experimental study and large eddy simulation of effect of terrain slope on marginal burning in shrub fuel beds. Proceedings of the Combustion Institute, 31(2), 2547-2555.

11. Appendices

11.1 Appendix A: Supporting Data

Text based files for the chemical kinetic models can be found here:
https://www.frontiersin.org/articles/10.3389/fmech.2019.00040/full#supplementary-material

All simulation codes developed during this project can be found here:
https://github.com/clapointe2011/public

11.2 Appendix B: List of Scientific/Technical Publications

Peer-Reviewed Journal Publications:

1. A. S. Makowiecki, D. I. Herman, N. Hoghooghi, E. F. Strong, R. K. Cole, G. G. Ycas, F. R. Giorgetta, C. B. Lapointe, J. F. Glusman, J. W. Daily, P. E. Hamlington, N. R. Newbury, I. R. Coddington, and G. B. Rieker. Mid-Infrared Dual Frequency Comb Spectroscopy for Combustion Analysis from 2.8 to 5 Microns. Proceedings of the Combustion Institute, https://doi.org/10.1016/j.proci.2020.06.195, 2021.
2. N. T. Wimer, M. S. Day, C. Lapointe, M. A. Meehan, A. S. Makowiecki, J. F. Glusman, J. W. Daily, G. B. Rieker, and P. E. Hamlington. Numerical simulations of buoyancy-driven flows using adaptive mesh refinement: structure and dynamics of a large-scale helium plume. Theoretical and Computational Fluid Dynamics, 35:61–91, 2021.
3. C. Lapointe, N. T. Wimer, J. F. Glusman, A. S. Makowiecki, J. W. Daily, G. B. Rieker, and P. E. Hamlington. Efficient simulation of turbulent diffusion flames in openfoam using adaptive mesh refinement. Fire Safety Journal, 111:102934, 2020.
4. A. S. Makowiecki, J. E. Steinbrenner, N. T. Wimer, J. F. Glusman, C. B. Lapointe, J. W. Daily, P. E. Hamlington, and G. B. Rieker. Dual Frequency Comb Spectroscopy of Solid Fuel Pyrolysis and Combustion: Quantifying the Influence of Moisture Content in Douglas Fir. Fire Safety Journal, 116:103185, 2020.
5. N. T. Wimer, C. Lapointe, J. D. Christopher, S. P. Nigam, T. R. S. Hayden, A. Upadhye, M. A. Strobel, G. B. Rieker, and P. E. Hamlington. Scaling of the puffing strouhal number for buoyant jets and plumes. Journal of Fluid Mechanics, 895:A26, 2020.
6. R. Cole, A. Makowiecki, N. Hoghooghi, and G. Rieker. Pressure Scaling of Measured Absorption Cross- Sections by Modifying the Molecular Free Induction Decay Signal. Journal of Quantitative Spectroscopy and Radiative Transfer, 254:107189, 2020.
7. R. Cole, A. Makowiecki, N. Hoghooghi, and G. Rieker. Baseline-free Quantitative Absorption Spectroscopy Based on Cepstral Analysis. Optics Express 27:37920-37939, 2019.
8. J. F. Glusman, K. E. Niemeyer, A. S. Makowiecki, N. T. Wimer, C. Lapointe, G. B. Rieker, P. E. Hamlington, and J. W. Daily. Reduced Gas-Phase Kinetic Models for Burning of Douglas Fir. Frontiers in Mechanical Engineering, 5:40, 2019.
9. S. A. Mason, P. E. Hamlington, B. D. Hamlington, W. M. Jolly, and C. M. Hoffman. Effects of Climate Oscillations on Burning Index Variability in the United States. Geophysical Research Letters, 44:7002–7010, 2017.

Conference Proceedings:

10. J. F. Glusman, C. B. Lapointe, A. S. Makowiecki, S. Simons-Wellin, G. B. Rieker, J. W. Daily, and P. E. Hamlington. Computationally efficient simulations of Douglas fir pyrolysis and combustion. Proceedings of the 12th U.S. National Meeting on Combustion, 2021.
11. C. B. Lapointe, S. Simons-Wellin, and P. E. Hamlington. Optimization for complex fire phenomena using adaptive mesh refinement. Proceedings of the 12th U.S. National Meeting on Combustion, 2021.
12. C. Lapointe, N. T. Wimer, J. F. Glusman, A. S. Makowiecki, J. W. Daily, G. B. Rieker, and P. E. Hamlington. Progress towards high fidelity simulations of large-scale fires. Proceedings of the 11th U.S. National Meeting on Combustion, 2019.
13. A. S. Makowiecki, N. T. Wimer, J. F. Glusman, J. W. Daily, P. E. Hamlington, and G. B. Rieker. Comparison of flame temperatures to mass flux rates for wildland fire fuels. Proceedings of the 11th U.S. National Meeting on Combustion, 2019.
14. J. F. Glusman, A. S. Makowiecki, N. T. Wimer, K. E. Niemeyer, G. B. Rieker, P. E. Hamlington, and J. W. Daily. A Chemical Kinetic Model Reduction and Pyrolysis Model for Wildland Fire Direct Numerical Simulation. Proceedings of the 2018 Western States Section of the Combustion Institute Spring Technical Meeting, Paper ID: 38CK-0010, 2018.
15. N. T. Wimer, C. Lapointe, T. R. S. Hayden, J. D. Christopher, A. Y. Poludnenko, G. B. Rieker, and P. E. Hamlington. Near- and Far-Field Properties of High-Temperature Turbulent Buoyant Jets. AIAA Paper, AIAA-2017-4423, 2017.
16. N. T. Wimer, A. S. Makowiecki, A. Y. Poludnenko, C. M. Hoffman, J. W. Daily, G. B. Rieker, and P. E. Hamlington. Direct Numerical Simulation of Wildland Fires at Small Scales. Proceedings of the 2017 Western States Section of the Combustion Institute Fall Technical Meeting, Paper ID: 29FI-0079, 2017.

Conference Presentations (abstract only):

17. C. Lapointe, N. T. Wimer, M. S. Day, A. S. Makowiecki, J. F. Glusman, J. W. Daily, G. B. Rieker, and P. E. Hamlington (2019) The Study of Fire at Small Scales Using Adaptive Mesh Refinement. 17th International Conference on Numerical Combustion, SIAM, 6-8 May 2019, Aachen, Germany.
18. N. T. Wimer, M. S. Day, A. S. Makowiecki, J. F. Glusman, J. W. Daily, G. B. Rieker, and P. E. Hamlington (2019) Low Mach Number AMR Combustion Simulations with PeleLM. SIAM Conference on Computational Science and Engineering, 25 February–1 March 2019, Spokane, WA.
19. C. Lapointe, N. T. Wimer, and P. E. Hamlington (2018) Progress Towards Efficient Simulation of Large- Scale Fires. 71st Annual meeting, Division of Fluid Dynamics, American Physical Society, Atlanta, GA, 18-20 November 2018.
20. N.T. Wimer, M. Day, A.S. Makowiecki, J.F. Glusman, J.W. Daily, G.B. Rieker, and P.E. Hamlington (2018) Progress Towards Direct Numerical Simulations of Plumes and Pool Fires. 71st Annual meeting, Division of Fluid Dynamics, American Physical Society, Atlanta, GA, 18-20 November 2018.
21. C. A. Z. Towery, A. Y. Poludnenko, and P. E. Hamlington (2018) Direct Numerical Simulations of High Intensity Turbulent Combustion and Fire. World Congress of Computational Mechanics, July 23-27, 2018, New York, NY.

22. P. E. Hamlington, C. Lapointe, N. T. Wimer, and M. Day (2018) Progress Towards Direct Numerical Simula- tion of Fire Using Adaptive Mesh Refinement. 10th FM Global Open Source CFD Fire Modeling Workshop, May 30-31, 2018, Norwood, MA.
23. N. T. Wimer, A. S. Mackowiecki, J. F. Glusman, A. Y. Poludnenko, C. Hoffman, J. W. Daily, G. B. Rieker, and P. E. Hamlington (2018) Direct Numerical Simulation of a Turbulent Helium Plume and Methane Pool Fire. The Fire Continuum Conference, 21-24 May 2018, Missoula, MT.
24. N. T. Wimer, A. S. Mackowiecki, A. Y. Poludnenko, C. Hoffman, J. W. Daily, G. B. Rieker, and P. E. Hamlington (2017) Examination of Wildland Fire Spread at Small Scales Using Direct Numerical Simulations and High-Speed Laser Diagnostics. American Geophysical Union Fall Meeting, 11-15 December 2017, New Orleans, LA.
25. A. Mackowiecki, N. Wimer, J. Daily, P. Hamlington, G. Rieker, C. Hoffman, and A. Poludnenko (2017) Examination of wildland fire spread at small scales using frequency comb laser diagnostics and direct numerical simulations. 7th International Fire Ecology & Management Congress, 28 November - 2 December, 2017, Orlando, FL.
26. N. Wimer, A. Mackowiecki, C. Hoffman, A. Poludnenko, J. Daily, G. Rieker, and P. Hamlington (2017) Direct Numerical Simulation of Wildland Fires at Small Scales. 70th Annual meeting, Division of Fluid Dynamics, American Physical Society, Denver, CO, 19-21 November 2017.

Conference Posters:

27. J. F. Glusman, A. Makowiecki, N. T. Wimer, C. Lapointe, A. Y. Poludnenko, C. M. Hoffman, J. W. Daily, G. B. Rieker, and P. E. Hamlington (2018) Examination of Wildfire Spread at Small Scales Using Direct Numeri- cal Simulations and Frequency Comb Laser Diagnostics. Strategic Environmental Research and Development Program (SERDP) and Environmental Security Technology Certification Program (ESTCP) Symposium, 27 November 2018, Washington, D.C.
28. A. Makowiecki, J. Steinbrenner, J. Glusman, N. Wimer, J. Daily, P. Hamlington, and G. Rieker (2018) Dual Frequency Comb Spectroscopy for the Investigation of Ignition Behaviour of Wildland Fire Fuels. Field Laser Applications in Industry and Research (FLAIR), Assisi, Italy, September 2018.
29. N. T. Wimer, C. Lapointe, M. Day, A. Y. Poludnenko, J. F. Glusman, A. S. Makowiecki, J. W. Daily, G. B. Rieker, and P. E. Hamlington (2018) Progress Towards Direct Numerical Simulations of Fire Using Adaptive Mesh Refinement. 37th International Symposium on Combustion, 29 July - 3 August 2018, Dublin, Ireland.
30. A. S. Makowiecki, J. E. Steinbrenner, J. F. Glusman, N. T. Wimer, J. W. Daily, P. E. Hamlington, and G. B. Rieker (2018) Diagnostics Suite for Benchmark Data of Wildland Fire Fuels for Application to Physics-Based Models. 37th International Symposium on Combustion, 29 July - 3 August 2018, Dublin, Ireland.
31. J. F. Glusman, A. S. Makowiecki, N. T. Wimer, K. E. Niemeyer, G. B. Rieker, P. E. Hamlington, and J. W. Daily (2018) Experimental Comparison of Small-Scale Biomass Pyrolysis and Reduced Chemical Kinetic Models for Direct Numerical Simulations of Wildland Fires. 37th International Symposium on Combustion, 29 July - 3 August 2018, Dublin, Ireland.
32. N. T. Wimer, A. Makowiecki, J. F. Glusman, A. Y. Poludnenko, C. M. Hoffman, J. W. Daily, G. B. Rieker, and P. E. Hamlington (2017) Examination of Wildfire Spread at Small Scales

Using Direct Numerical Sim- ulations and Frequency Comb Laser Diagnostics. Strategic Environmental Research and Development Pro- gram (SERDP) and Environmental Security Technology Certification Program (ESTCP) Symposium, 28-30 November 2017, Washington, D.C.

33. A. S. Makowiecki, N. Hoghooghi, N. T. Wimer, J. W. Daily, P. E. Hamlington, and G. B. Rieker (2017) Cavity Enhanced Dual Frequency Comb Spectroscopy for Characterization of Biomass Pyrolysis. Gordon Research Conference: Laser Diagnostics in Combustion, 6-11 August 2017, West Dover, VT.
34. N. T. Wimer, A. Makowiecki, A. Y. Poludnenko, C. M. Hoffman, J. W. Daily, G. B. Rieker, and P. E. Hamlington (2017) Examination of Wildland Fire Spread at Small Scales Using Direct Numerical Simulations and Frequency Comb Laser Diagnostics. 12th International Symposium on Fire Safety Science, 12-16 June 2017, Lund, Sweden.
35. S. A. Mason, P. E. Hamlington, B. D. Hamlington, W. M. Jolly, and C. M. Hoffman (2016) Effects of Climate Oscillations on Burning Index Variability in the Continental United States. American Geophysical Union Fall Meeting, 12-16 December 2016, San Francisco, CA.

Invited Seminars:

36. P. E. Hamlington (2020) Adaptive Mesh Simulations of Fine-Scale Combustion for Physics-Based Models of Wildland Fire. Environmental Engineering Program, University of Colorado, Boulder, November 6, 2020.
37. P. E. Hamlington (2019) Progress Towards Direct Numerical Simulations of Fire Using Adaptive Mesh Re- finement. Department of Mechanical and Aerospace Engineering Seminar, University of Colorado, Colorado Springs, September 19, 2019.
38. P. E. Hamlington (2018) Progress Towards Direct Numerical Simulations of Fire Using Adaptive Mesh Re- finement. Mechanical and Aerospace Engineering Seminar, Arizona State University, Tempe, AZ, Nov. 9, 2018.
39. P. E. Hamlington (2018) Progress and Challenges in High-Fidelity Numerical Simulations of Combustion and Fire. Oregon State University, Corvallis, OR, October 26, 2018.
40. P. E. Hamlington (2018) High-Fidelity Numerical Simulations of Combustion and Fire: A Hot Topic in a Warming World. Department of Mechanical Engineering, University of Colorado, Boulder, CO, October 19, 2018.
41. P. E. Hamlington (2018) A Bridge Between Communities: The Study of Wildland Fires Using Techniques from Combustion. Colorado State University, Ft. Collins, CO, October 18, 2018.
42. P. E. Hamlington (2018) Direct Numerical Simulations of Combustion and Fire. University of Wyoming, Laramie, WY, October 4, 2018.
43. P. E. Hamlington (2018) From Turbines to Trees: Direct Numerical Simulations of Combustion and Fire. National Renewable Energy Laboratory, Golden, CO, July 9, 2018.